

**MASSACHUSETTS INSTITUTE OF TECHNOLOGY
LINCOLN LABORATORY**

SOLID STATE RESEARCH

QUARTERLY TECHNICAL REPORT

1 FEBRUARY — 30 APRIL 1988

ISSUED 18 NOVEMBER 1988

Approved for public release; distribution unlimited.

AD-A204 718

The work reported in this document was performed at Lincoln Laboratory, a center for research operated by Massachusetts Institute of Technology, with the support of the Department of the Air Force under Contract F19628-85-C-0002.

This report may be reproduced to satisfy needs of U.S. Government agencies.

The views and conclusions contained in this document are those of the contractor and should not be interpreted as necessarily representing the official policies, either expressed or implied, of the United States Government.

The ESD Public Affairs Office has reviewed this report, and it is releasable to the National Technical Information Service, where it will be available to the general public, including foreign nationals.

This technical report has been reviewed and is approved for publication.

FOR THE COMMANDER

Hugh L. Southall

Hugh L. Southall, Lt. Col., USAF
Chief, ESD Lincoln Laboratory Project Office

Non-Lincoln Recipients

PLEASE DO NOT RETURN

Permission is given to destroy this document
when it is no longer needed.

**MASSACHUSETTS INSTITUTE OF TECHNOLOGY
LINCOLN LABORATORY**

SOLID STATE RESEARCH

QUARTERLY TECHNICAL REPORT

1 FEBRUARY — 30 APRIL 1988

ISSUED 18 NOVEMBER 1988

Approved for public release; distribution unlimited.

LEXINGTON

MASSACHUSETTS

Printed by
United States Air Force
Hanscom AFB, MA 01731

ABSTRACT

This report covers in detail the research work of the Solid State Division at Lincoln Laboratory for the period 1 February through 30 April 1988. The topics covered are Solid State Device Research, Quantum Electronics, Materials Research, Microelectronics, and Analog Device Technology. Funding is provided primarily by the Air Force, with additional support provided by the Army, DARPA, Navy, SDIO, NASA, and DOE.



Accession For	
NTIS GRA&I	<input checked="" type="checkbox"/>
DTIC TAB	<input type="checkbox"/>
Unannounced	<input type="checkbox"/>
Justification	
By _____	
Distribution/	
Availability Codes	
Dist	Avail and/or Special
A-1	

TABLE OF CONTENTS

Abstract	iii
List of Illustrations	vii
List of Tables	xi
Introduction	xiii
Reports on Solid State Research	xvii
Organization	xxv
1. SOLID STATE DEVICE RESEARCH	1
1.1 p ⁺ -AlInAs/InP Depletion-Mode JFET	1
1.2 Reduction of Intermodulation Distortion in Interferometric Optical Modulators	2
1.3 InGaAsP/InP Buried-Heterostructure Lasers With Concurrently Fabricated Stripes and Mirrors	6
1.4 Y-Junction-Coupled InGaAsP/InP Buried-Heterostructure Laser Arrays	9
1.5 Hydride Adsorption on Impregnated Carbon	11
2. QUANTUM ELECTRONICS	17
2.1 Modeling of Q-Switched, Four-Level Lasers With Nonzero Lower-Level Lifetime	17
2.2 Intracavity Frequency Modulation of Nd:YAG Laser Radiation	19
2.3 Measurement of Doubling Efficiency Using 150- μ s Macropulses From a Nd:YAG Laser	25
2.4 Amplified Spontaneous Emission in a Ti:Al ₂ O ₃ Amplifier	28
2.5 Wavelength-Independent Faraday Isolator	32
3. MATERIALS RESEARCH	37
3.1 Infrared Absorption of Ir and IrSi Thin Films on Si	37
3.2 100-MHz Modulation of GaAs/AlGaAs LED Monolithically Integrated With Si Driver Circuit	42

4. MICROELECTRONICS. <i>anal</i>	47
4.1 Discrete Fourier Transform CCD	47
4.2 Back-Illuminated Thinned CCD Imagers	51
4.3 Back Stabilization Coatings for Thinned CCD Imagers	54
5. ANALOG DEVICE TECHNOLOGY. <i>Keywords: → to form in 57</i>	57
5.1 Process Integration of Superconducting Thin Films and Dielectric Thick Films	57
5.2 High- T_c Superconducting Resonators	60

LIST OF ILLUSTRATIONS

Figure No.		Page
1-1	Schematic Diagram of a p^+ -AlInAs/InP JFET Showing the Si^+ -Implanted n-InP and the MBE-Grown AlInAs Crystalline and Polycrystalline Regions	1
1-2	Typical I-V Characteristics of a $4 \times 200\text{-}\mu\text{m}$ p^+ -AlInAs/InP JFET (With Buffer Layer). The Zero-Gate-Bias Curve Is Second From the Top.	2
1-3	Analog Optical Communication Link Consisting of Constant-Power Optical Source, Polarizer, Interferometric Modulator, and Detector	3
1-4	Plot of Detector Electrical Output Power Level, $20 \log (P_{kl} ^{TE} + P_{kl} ^{TM}) / P_{in}$, for the Fundamental, $P_{1,0}$, and Third-Order IM Product, $P_{1,2}$, as a Function of Modulator Electrical Drive Power, $20 \log (2V_m / V_{\pi}^{TE})$. Dashed Lines Indicate Single-Polarization Operation. Solid Lines Indicated Optimized Dual-Polarization Operation with $\gamma = 3$.	5
1-5	SEM Perspective View of IBAE-Defined Cylindrical-Mirror Laser After Etching and Mass Transport. The Supporting Mesa Regions on Either Side of the Laser Mesa Are Also Shown.	7
1-6	Far-Field Patterns of IBAE-Defined Etched-Mirror Lasers	8
1-7	Y-Junction-Coupled Laser Array: (a) Schematic Illustration, and (b) Top View of a Portion of an IBAE-Defined Mesa	10
1-8	Far-Field Pattern in the Junction Plane of a Y-Junction-Coupled Laser Array. The Laser Was Excited at 1.5 Times the Threshold Current.	11
1-9	Volume of Hydride Adsorbed During Six Adsorption/Oxidation Runs. (The Fifth Run of the Phosphine Adsorption Test Was Inadvertently Run at a Different Concentration and the Volume Was Not Accurately Determined. For Purposes of Determining the Total Capacity, the Volume Adsorbed Was Assumed to Be the Same as During the Fourth and Sixth Runs.)	13
2-1	Energy Level Diagram of the $1.064\text{-}\mu\text{m}$ Nd:YAG Transition	18
2-2	Extraction Efficiency as a Function of the Ratio r of the Initial Population Inversion Density to the Threshold Inversion Density and the Ratio τ of the Lower-Laser-Level Lifetime to the Cavity Lifetime	19

Figure No.		Page
2-3	Calculated Frequency-Modulation Spectra for Various Depths of Modulation Γ : (a) Single Carrier Frequency ω_0 ; $\omega = \omega_0 + n\omega_m$ and (b) Two Carrier Frequencies ω_0 and ω_0' Corresponding to Adjacent Cavity Modes; $\omega_n = \omega_0 + n\omega_m$ and $\omega_k' = \omega_0' + k\omega_m$. The Two Carrier Frequencies Are Assumed to Be Incoherent Relative to One Another. For the Purpose of This Figure, the Sideband Intensities of Nearly the Same Frequency From Different Carrier Frequencies Are Added Incoherently.	21
2-4	Measured Frequency-Modulation Spectra of a 1.32- μm Nd:YAG Laser for Various Depths of Modulation Γ . The Laser Had a Cavity Mode Spacing of 150.000 MHz and Was Modulated at 149.800 MHz. (a) Spectral Profiles of the Frequency-Modulated Laser When Operating With a Single Carrier Frequency. The Laser Free-Running Spectral Profile Is Shown in the Uppermost Plot. (b) Spectral Profiles of the Frequency-Modulated Laser When Operating With Two Carrier Frequencies Corresponding to Adjacent Cavity Modes	22
2-5	Measured Depth of Frequency Modulation Γ as a Function of the Relative Sinusoidal Drive Voltage Applied to the Intracavity LiNbO ₃ Crystal	23
2-6	Measured Depth of Frequency Modulation Γ as a Function of the Inverse of the Difference Between the Cavity Mode Spacing ($\nu_c + \omega_c/2\pi$) and the Modulation Frequency ($\nu_m = \omega_m/2\pi$)	24
2-7	Spectral Profiles of Frequency-Modulated 1.06- and 1.32- μm Nd:YAG Lasers and Their Sum Radiation at 0.589 μm . The Modulation Depth of the Sum Radiation Could Be Varied From Zero to Twice That of the Nd:YAG Laser by Adjusting the Phase Difference $\Delta\phi$ Between the Two Laser Modulations. The Single-Frequency Result at $\Delta\phi = 180^\circ$ Confirms that Each Nd:YAG Laser Was Operating With a Single Carrier Frequency	25
2-8	Oscilloscope Trace of Laser Input to Frequency-Doubling Crystals	26
2-9	Spatial Properties of (a) Nd:YAG Laser System Output at 1.064 μm and (b) the Second Harmonic Generated in a LiIO ₃ Crystal at 0.532 μm . The Light Areas in the Centers Are Generally the Regions of Most Intense Radiation, but Some of the Hot Spots Within Those Regions Appear as Dark Islands. The Lighter Regions on the Perimeter Represent Areas of Lower Intensity Than in the Intervening Dark Region.	27

Figure No.		Page
2-10	The Decay (Solid Line) of the Amplified Signal at 791 nm in a Ti:Al ₂ O ₃ Crystal From Reference 10. The Model (Dots) Gives an Excellent Fit to the Decay With a Solid Angle Parameter of 0.04. The Experimentally Measured Initial Value of γ is 5.27.	29
2-11	Log-Log Plot of Solid Angle Parameters Obtained From Model Versus Amplifier Gain. An Intensity-Independent Solid Angle Is Expected at Low Intensities. At High Intensities Such That the Pump Saturates the Inversion, the Solid Angle Is Expected to Decrease as γ^2 , Shown as a Line With Slope -2 on This Log-Log Plot.	30
2-12	Decay of the Amplified signal at 633 nm in a Ti:Al ₂ O ₃ Crystal From Reference 10. The Model Gives an Excellent Fit to the Decay With No Adjustable Parameters. Also Shown Is the Shape of the Decay Curve if Amplified Spontaneous Emission Is Not Included.	31
2-13	Backward Transmission Through Faraday Isolator. The Compensated Faraday Isolator Has a Backward Transmission (Solid Line) Nearly Independent of Wavelength. The Slight Wavelength Dependence Is Caused by a Mismatch Between the Optically Active Rotator and the Faraday Rotator of $\sim 1^\circ$ at 780 nm. Such a Mismatch Gives Rise to an Expected Backward Transmission (Dashed Line). The Backward Transmission of a Conventional Isolator Is Shown by the Dotted Line.	33
2-14	Forward Transmission Through Faraday Isolator. The Observed Transmission (Solid Line) Is Smaller Than Expected (Dashed Line). The Discrepancy May Be Caused by Imperfect Coatings. The Expected Transmission in a Conventional Isolator Is Shown by the Dotted Line.	34
3-1	Configuration for Measurement of Reflection R and Transmission T of Film/Substrate Sample	38
3-2	Absorption Versus Thickness for PtSi Films on Si Substrates	38
3-3	Absorption Versus Thickness for (a) Ir and (b) IrSi Films on Si Substrates	40
3-4	Elemental Depth Profiles Obtained by Auger Analysis for (a) Ir, (b) IrSi, (c) Pt, and (d) PtSi Films on Si Substrates	41
3-5	Circuit Diagram of Monolithically Integrated LED/Driver Circuit	42

Figure No.		Page
3-6	Photomicrograph of LED/Driver Circuit	43
3-7	Dc Light Output of LED as a Function of Driver Input Voltage	45
3-8	Waveforms of Driver Input Voltage (5 V/div) and LED Light Output (5 mV/div) for Modulation at 100 MHz	45
4-1	CCD Discrete Fourier Transform Device Concept	47
4-2	CCD Fixed-Weight Multiplier With Normal or Inverting Potential Equilibration Input Structure	48
4-3	Conventional and New Split-Gate CCD Input Structures	49
4-4	Photomicrograph of Discrete Fourier Transform CCD	50
4-5	Cross-Sectional View of Thinned CCD Structure	51
4-6	Whole 3-in Wafer Containing Various Types of Imaging Chips After Mounting, Thinning, and Etching Process	53
4-7	SEM Photograph of Wire Bonds to Thinned Imaging Chip	53
4-8	Resolution Chart Imaged Onto Thinned CCD at Low Light Levels: (a) 127 e/pixel, (b) 25 e/pixel	54
5-1	Basic Structure for the Stripline Using an Integrated Superconductive-Thin-Film/Dielectric-Thick-Film Approach	57
5-2	Exploded View of the L-C Resonator Test Structure	59
5-3	Stripline Resonator Structure: (a) Cross Section; (b) Top View of Center Conductor	62
5-4	Calculated Single-Sideband Phase Noise	64
5-5	Measured Residual Noise for All-Nb Superconducting Resonator at 1.15 GHz	65

LIST OF TABLES

Table No.		Page
1-1	Summary of Experimental and Theoretical Results	6
3-1	Complex Dielectric Constants at 4 μm	41
4-1	Multiplier Accuracy	50
4-2	Fabrication Process for Back-Illuminated Thinned Imagers	52
4-3	Fixed Charge in Deposited Oxides	55

INTRODUCTION

1. SOLID STATE DEVICE RESEARCH

Depletion-mode $p^+-AlInAs/InP$ junction FETs have been fabricated in semi-insulating InP using a selective molecular-beam-epitaxy technique. Current-voltage measurements on devices with a $4\text{-}\mu\text{m}$ gate length show a transconductance of 41 mS/mm at zero gate bias, and RF measurements indicate a maximum frequency of oscillation of 3.2 GHz .

A dual-polarization technique for reducing intermodulation distortion in integrated-optic interferometric modulators has been developed. For a given depth of optical modulation, the intermodulation distortion can be significantly reduced by adjusting the relative amounts of TE and TM optical power.

Concurrent fabrication of $InGaAsP/InP$ buried-heterostructure laser stripes and mirrors has been demonstrated by the use of dry etching and mass transport. In comparison to previous processes in which the laser stripes and mirrors are fabricated separately, this process offers the advantages of simplicity, built-in alignment, and improved control of device dimensions.

Coherent arrays of multiple-stripe $InGaAs/InP$ mass-transported buried-heterostructure lasers have been made by using Y-junction coupling. Sharply defined Y-junctions have been formed by ion-beam-assisted etching to facilitate low-loss coupling.

Adsorption on impregnated carbon has been studied as a method to safely and effectively control arsine and phosphine emissions from OMVPE systems. The capacities for these hydrides, with multiple adsorption/oxidation cycles, have been determined under typical laboratory-scale OMVPE operating conditions.

2. QUANTUM ELECTRONICS

A reduction in efficiency of Q-switched Nd^{3+} lasers due to a nonzero lower-state lifetime has been predicted by a rate-equation model. For the $1.064\text{-}\mu\text{m}$ Nd:YAG transition, the efficiency reduction is, at worst, 32 percent.

Intracavity frequency modulation of a Nd:YAG laser at very nearly the cavity mode spacing has produced output having either a single carrier frequency or two carrier frequencies corresponding to adjacent cavity modes. By using the same modulation drive frequency for two Nd:YAG lasers (1.32 and $1.06\text{ }\mu\text{m}$) and adjusting the relative phases of the drive voltages, the degree of modulation of sum-frequency radiation ($0.589\text{ }\mu\text{m}$) may be varied from zero to twice that of the Nd:YAG lasers.

A Nd:YAG laser system has been modified to produce $150\text{-}\mu\text{s}$ macropulses, and frequency-doubling experiments have been carried out with several doubling crystals using these macro-pulses at a 10-Hz PRF. In the best case, second harmonic generation efficiency was found to be limited to ~ 30 percent, with the limitation imposed by the fundamental laser beam configuration.

The time dependence of amplified spontaneous emission has been studied using a simple model. Experimental measurements of the gain in a $\text{Ti:Al}_2\text{O}_3$ amplifier affected by amplified spontaneous emission are in excellent agreement with the model.

A new configuration Faraday isolator for use with the $\text{Ti:Al}_2\text{O}_3$ laser has been constructed using a 45° birefringent rotator and a 45° Faraday rotator. Isolation >27 dB and transmission in the forward direction better than 55 percent have been achieved over a wavelength range from 700 to 900 nm.

3. MATERIALS RESEARCH

The infrared absorption of Ir and IrSi thin films on Si substrates has been determined by transmission and reflection measurements over the wavelength range from 2.5 to 25 μm . The existence at the Ir/Si or IrSi/Si interface of a thin boundary layer with lower absorption than Ir or IrSi is indicated by the thickness dependence of the absorption and has been confirmed by the detection of oxygen at the interface by Auger analysis.

A GaAs/AlGaAs light-emitting diode (LED) has been monolithically integrated with a Si driver circuit composed of 10 MOSFETs. By applying a stream of voltage pulses to the input of the driver circuit, the LED output has been modulated at rates exceeding 100 MHz.

4. MICROELECTRONICS

An analog CCD discrete Fourier transform device has been designed, utilizing a new split-gate input structure. The device performs a 16-point transform with <37 -dB harmonic distortion at 5-MHz data rate and shows greatly improved accuracy between measured and calculated vector output compared with the earlier-reported discrete cosine transform chip.

A process has been developed to uniformly thin and package large CCD imagers for use with back illumination in order to achieve greater green and blue sensitivity. The noise and charge transfer efficiency are not materially affected by the process, but the dark current is elevated to ten times that of an unthinned wafer.

Various low-temperature dielectric coatings have been investigated to find one which contains a net negative charge in order to accumulate and stabilize the exposed p-type surface of a back-illuminated CCD imager. It has been discovered that electron-beam-evaporated aluminum oxide contains negative charge density in excess of 10^{11} electrons per square centimeter, a value adequate to improve the response of the imager in the visible and UV, whereas sputtered or evaporated silicon dioxide or sputtered aluminum oxide has positive charge.

5. ANALOG DEVICE TECHNOLOGY

A 10-MHz resonator utilizing superconductive NbN thin-film electrodes and ceramic thick-film dielectrics has been built in order to demonstrate the feasibility of integrating the two technologies in analog signal processing devices. The NbN remained superconducting after the 800°C firing of the ceramic, and the conductor and dielectric losses were small enough to give a resonator Q of 80.

Calculations of the phase noise of 10-GHz oscillators stabilized with high-temperature superconducting stripline resonators have been made and indicate excellent performance. The residual noise of niobium-based resonators has been measured and exhibits the expected behavior for offset frequencies >10 Hz.

REPORTS ON SOLID STATE RESEARCH

1 February through 30 April 1988

PUBLISHED REPORTS

Journal Articles

JA No.

5936	Serrodyne Optical Frequency Translation with High Sideband Suppression	L.M. Johnson C.H. Cox, III	J. Lightwave Technol. LT-6, 109 (1988)
5962	Cross Power and Crosstalk in Waveguide Couplers	J.P. Donnelly H.A. Haus* L.A. Molter*	J. Lightwave Technol. LT-6, 257 (1988)
6008	Characterization of Mass-Transported p-Substrate GaInAsP/InP Buried-Heterostructure Lasers with Analytical Solutions for Electrical and Thermal Resistances	Z.L. Liao J.N. Walpole D.Z. Tsang V. Diadiuk	IEEE J. Quantum Electron. QE-24, 36 (1988)
6014	Superconducting Analog Track-and-Hold Circuit	D. Go* C.A. Hamilton* F.L. Lloyd* M.S. Dilorio R.S. Withers	IEEE Trans. Electron Devices ED-35, 498 (1988)
6030	New MBE Buffer Used To Eliminate Backgating in GaAs MESFET's	F.W. Smith A.R. Calawa C.L. Chen M.J. Manfra L.J. Mahoney	IEEE Electron Device Lett. EDL-9, 77 (1988)
6031	Avalanche-Induced Drain-Source Breakdown in Silicon-on-Insulator n-MOSFET's	K.K. Young J.A. Burns	IEEE Trans. Electron Devices ED-35, 426 (1988)
6032	Electron-Beam-Pumped Two-Dimensional Semiconductor Laser Array with Tilted Mirror Resonator	F. Tong R.M. Osgood* A. Sanchez V. Daneu	Appl. Phys. Lett. 52, 1303 (1988)

* Author not at Lincoln Laboratory.

JA No.

- | | | | |
|------|---|--|--|
| 6040 | Pump Power Minimization for High Gain CW Laser Amplifiers | A. Walther
A. Sanchez | Appl. Opt. 27, 828 (1988) |
| 6047 | Spatial Light Modulators Using Charge-Coupled-Device Addressing and Electroabsorption Effects in GaAs/AlGaAs Multiple Quantum Wells | K.B. Nichols
B.E. Burke
B.F. Aull
W.D. Goodhue
B.F. Gramstorff
C.D. Hoyt
A. Vera | Appl. Phys. Lett. 52, 1116 (1988) |
| 6060 | Pt-Ir Silicide Schottky-Barrier IR Detectors | B-Y. Tsaur
M.M. Weeks*
P.W. Pellegrini* | IEEE Electron Device Lett. EDL-9, 100 (1988) |
| 6064 | Low-Threshold GaAs/AlGaAs Lasers Grown on Si by Organometallic Vapor Phase Epitaxy | H.K. Choi
J.W. Lee*
J.P. Salerno*
M.K. Connors
B-Y. Tsaur
J.C.C. Fan* | Appl. Phys. Lett. 52, 1114 (1988) |

Meeting Speeches

MS No.

- | | | | |
|------|--|---|--|
| 7491 | Analog Superconductive Correlator for Wideband Signal Processing | J.B. Green
A.C. Anderson
R.S. Withers | <i>Extended Abstracts, 1987 International Superconductivity Conference, Tokyo, Japan, 28-29 August 1987, p. 49</i> |
| 7581 | Multiple-Quantum-Well CCD Spatial Light Modulators | B.F. Aull
B.E. Burke
K.B. Nichols
W.D. Goodhue | <i>Spatial Light Modulators and Applications II, Proc. SPIE 825, 2 (1988)</i> |
| 7582 | Phase Noise of Bulk-Acoustic-Wave Reflection-Grating Resonators | D.E. Oates
J.Y. Pan | <i>1987 Ultrasonics Symposium Proceedings (IEEE, New York, 1987), pp. 331-336</i> |
| 7587 | Laser Direct Write Compensation of Reflective Array Compressors | V.S. Dolat
J.H. Sedlacek
D.J. Ehrlich | <i>1987 Ultrasonics Symposium Proceedings (IEEE, New York, 1987), pp. 203-208</i> |
| 7623 | Optical Considerations for Excimer Projection Systems | M. Rothschild
D.J. Ehrlich | <i>Mat. Res. Soc. Symp. Proc., Vol. 101 (1988), p. 13</i> |

* Author not at Lincoln Laboratory.

UNPUBLISHED REPORTS

Journal Articles

JA No.

6056	MBE-Grown Spatial Light Modulators with Charge-Coupled-Device Addressing	W.D. Goodhue B.E. Burke B.F. Aull K.B. Nichols	Accepted by J. Vac. Sci. Technol. B
6061	Sensitivity of Quantitative Vibrational CARS Spectroscopy to Saturation and Stark Shifts	M. Pealat* M. Lefebvre* J.-P. Taran* P.L. Kelley	Accepted by Phys. Rev. A
6062	Residual Infrared Absorption in As-Grown and Annealed Crystals of Ti:Al ₂ O ₃	R.L. Aggarwal R.E. Fahey A. Sanchez M.M. Stuppi A.J. Strauss	Accepted by IEEE J. Quantum Electron.
6070	Single Frequency Ti:Al ₂ O ₃ Ring Laser	P.A. Schulz	Accepted by IEEE J. Quantum Electron.
6079	High-Performance InGaAsP/InP Buried-Heterostructure Lasers and Arrays Defined by Ion-Beam-Assisted Etching	D. Yap Z.L. Liao D.Z. Tsang J.N. Walpole	Accepted by Appl. Phys. Lett.
6082	Wideband Superconductive Chirp Filters	M.S. DiIorio R.S. Withers A.C. Anderson	Accepted by IEEE Trans. Microwave Theory Tech.
6086	Crystal Growth, Spectroscopy, and Laser Characteristics of Ti:Al ₂ O ₃	A. Sanchez	Accepted by IEEE J. Quantum Electron.
6089	Large-Numerical-Aperture InP Lenslets by Mass Transport	Z.L. Liao V. Diadiuk J.N. Walpole D.E. Mull	Accepted by Appl. Phys. Lett.

* Author not at Lincoln Laboratory.

UNPUBLISHED REPORTS

Meeting Speeches

MS No.

7095F	A Neural-Network Integrated Circuit with Synapses Based on CCD/MNOS Principles	J.P. Sage	1988 IEEE International Solid State Circuits Conference, San Francisco, California, 17-18 February 1988
7711	International Solid State Circuits Conference Panel on Issues in Fabrication of Neural Networks	J.P. Sage	
7268	Emerging Technology for In-Situ Processing	D.J. Ehrlich	1988 Spring Meeting of the Materials Research Society, Reno, Nevada, 5-8 April 1988
7859	Homoepitaxial Semiconducting Diamond	M.W. Geis D.L. Smythe J.J. Zayhowski M. Rothschild D.J. Ehrlich	
7553	Advanced Device Fabrication with Angled Chlorine Ion-Beam-Assisted Etching	W.D. Goodhue	
7553A	Advanced Device Fabrication with Angled Chlorine Ion-Beam-Assisted Etching	W.D. Goodhue	
7654	Device Applications of Diamond	M.W. Geis	Seminar, Bell Laboratory, Murray Hill, New Jersey, 8 March 1988
7656A	Two-Dimensional Surface Emitting Diode Laser Arrays	R.C. Williamson	Technical Seminars Series, University of Minnesota, Minneapolis/St. Paul, Minnesota, 4 February 1988
7707	Excimer Projection Lithography at 193-nm Wavelength	M. Rothschild D.J. Ehrlich	SPIE Symposium on Microlithography, Santa Clara, California, 28 February-4 March 1988

MS No.

7714A	Multiple-Quantum-Well Structures for Electrooptic Devices	B.F. Aull	Technical Seminars Series, Northeastern University, Boston, Massachusetts, 25 February 1988
7739	Optically Induced Birefringence in $\text{Ti:Al}_2\text{O}_3$	R.L. Aggarwal K.F. Wall R.E. Fahey A.J. Strauss	CLEO '88, Anaheim, California, 25-29 April 1988
7743	Symmetrically Detuned Optical Three-Guide Coupler Switches in GaAs	L.A. Molter* J.P. Donnelly H.A. Haus* L.M. Johnson	
7746	Modeling for the Design of High Gain Pulsed Multistage Laser Amplifiers	A. Walther R.S. Tapper A. Sanchez	
7773	Wideband Interdigitated-Electrode p-HgCdTe Photomixers at 25 μm	D.L. Spears	
7917	Time-Resolved Wavefront Measurement of a Pulsed Dye Laser Using Integrated Optics	B.G. Zollars R.H. Rediker T.A. Lind B.E. Burke	
7741	Integrated-Optical 2×2 Switch with Y-Branch Mode Splitters	L.M. Johnson H.V. Roussell	IGWO '88, Santa Fe, New Mexico, 28-30 March 1988
7744	Use of Integrated Guided-Wave Optics to Measure and/or Process Optical Wavefronts with High-Temporal Resolution	R.H. Rediker T.A. Lind B.E. Burke B.G. Zollars	
7747	Optical Two-Guide Coupler Switches in GaAs: Ideal and Nonideal Operation	L.A. Molter* H.A. Haus* L.M. Johnson J.P. Donnelly	
7748	InGaAsP/InP Buried-Heterostructure Lasers and Laser Arrays Fabricated by Ion-Beam-Assisted Etching	D.Yap J.N. Walpole Z.L. Liao	
7762	Monolithic Two-Dimensional GaInAsP/InP Laser and Lenslet Arrays	Z.L. Liao J.N. Walpole V. Diadiuk	

* Author not at Lincoln Laboratory.

MS No.

7756	Superconductive Signal Processing Devices	J.B. Green	} American Physical Society Meeting, New Orleans, Louisiana, 21-25 March 1988
7782	Effects of Annealing Environments on the Microstructure of $\text{La}_{1.85}\text{Sr}_{0.15}\text{CuO}_{4-y}$ Ceramics	G.L. Doll* J.S. Speck* M.S. Dresselhaus* A.J. Strauss	
7787	Microwave Circuit Applications of Superconductive Electronics	R.W. Ralston	
7770	Monolithic GaAs/Si Integration	G.W. Turner H.K. Choi J.P. Mattia C.L. Chen S.J. Eglash B-Y. Tsaur	1988 Spring Meeting of the Materials Research Society, Reno, Nevada, 5-8 April 1988
7787A	Microwave Circuit Applications of Superconductive Electronics	R.W. Ralston	IEEE Seminar on Superconductivity, RADC, Hanscom Air Force Base, Massachusetts, 26 April 1988
7814	Surface-Emitting Two-Dimensional Semiconductor Diode Laser Arrays	J.P. Donnelly	Technical Seminars Series, Swarthmore College, Swarthmore, Pennsylvania, 4 February 1988
7822	MBE-Grown Spatial Light Modulators with Charge-Coupled-Device Addressing	W.D. Goodhue	Seminar, Jet Propulsion Laboratory, Pasadena, California, 10 February 1988
7836	Integrated Optics	L.M. Johnson	} Optoelectronics Symposium, MIT, Cambridge, Massachusetts, 13 April 1988
7837	New Structures	R.C. Williamson	
7838	High-Speed Resonant-Tunneling Diodes	E.R. Brown T.C.L.G. Sollner W.D. Goodhue C.L. Chen	SPIE Symposium on Semiconductors, Newport Beach, California, 13-18 March 1988
7845	Angled Chlorine Ion-Beam-Assisted Etching, A Technique for Sculpturing in GaAs and AlGaAs	W.D. Goodhue S.W. Pang M.A. Hollis J.P. Donnelly	Metallurgical Society Conference on Electronic Materials, University of Colorado, Boulder, Colorado, 22-28 February 1988

* Author not at Lincoln Laboratory.

MS No.		
7850A, B	Ti:Al ₂ O ₃ Ring Laser Dynamics	P.A. Schulz
		Seminar, Spectra Technology, Stanford, California, 9 February 1988; Seminar, MIT, Cambridge, Massachusetts, 20 April 1988
7854,A	SOI via Zone-Melting Recrystallization	K.K. Young
		Seminar, University of California, Berkeley, California, 12 February 1988; IEEE Solid State Circuits Workshop on Emerging Technologies, San Francisco, California, 15 February 1988
7860	A New Buffer Layer Used to Eliminate Sidegating in GaAs MESFETs	F.W. Smith A.R. Calawa
		WOCSEMMAD 1988, Monterey, California, 22-24 February 1988
7864	Integrated Optic A/D Converters and Modulators	R.C. Williamson L.M. Johnson G.E. Betts
7865	Recent Advances in Mass-Transported GaInAsP/InP Buried-Heterostructure Lasers	D. Yap D.Z. Tsang Z.L. Liao J.N. Walpole
		DoD Fiber Optics Conference '88, McLean, Virginia, 22-25 March 1988
7894	Radiation-Hardened Silicon-on-Insulator Junction Field-Effect Transistors	B-Y. Tsaur
		Workshop on High-Temperature Electronics, Albuquerque, New Mexico, 12-14 April 1988
7941	IEEE Panel Discussion on Microwave Applications of High-Temperature Superconductors	R.S. Withers
		IEEE Microwave Theory and Techniques, Boston Chapter Meeting, Lincoln Laboratory, Lexington, Massachusetts, 19 April 1988

ORGANIZATION

SOLID STATE DIVISION

A.L. McWhorter, *Head*
I. Melngailis, *Associate Head*
E. Stern, *Associate Head*
J.F. Goodwin, *Assistant*

N.L. DeMeo, Jr., *Associate Staff*

QUANTUM ELECTRONICS

A. Mooradian, *Leader*
P.L. Kelley, *Associate Leader*
A. Sanchez-Rubio, *Assistant Leader*

Aggarwal, R.L.	McClung, S.K.
Barch, W.E.	Menyuk, N.
Belanger, L.J.	Mims, V.A.*
Brailove, A.A.	Schulz, P.A.
Daneu, V.	Sciacca, M.D.
DeFeo, W.E.	Seppala, J.P.
Fan, T.Y.	Sharfin, W.F.
Hancock, R.C.	Sullivan, D.J.
Hryniewicz, J.V.	Tapper, R.S.
Jeys, T.H.	Walker, W.A.
Lacovara, P.	Wall, K.F.
Le, H.Q.	Zayhowski, J.J.

ELECTRONIC MATERIALS

A.J. Strauss, *Leader*
B-Y. Tsaur, *Associate Leader*
H.J. Zeiger, *Senior Staff*

Anderson, C.H., Jr.	Kolesar, D.F.
Button, M.J.	Krohn, L., Jr.
Chen, C.K.	Mastromattei, E.L.
Choi, H.K.	Mattia, J.P.
Clark, H.R., Jr.	Nitishin, P.M.
Connors, M.K.	Pantano, J.V.
Delaney, E.J.	Tracy, D.M.
Eglash, S.J.	Turner, G.W.
Fahey, R.E.	Wang, C.A.
Finn, M.C.	Young, K.K.
Iseler, G.W.	

APPLIED PHYSICS

R.C. Williamson, *Leader*
D.L. Spears, *Assistant Leader*
R.H. Rediker, *Senior Staff*

Aull, B.F.	Johnson, L.M.	Pang, L.Y.†
Betts, G.E.	Ketteridge, P.A.	Rauschenbach, K.
Bossi, D.E.†	Kim, S-M.†	Reeder, R.E.
Corcoran, C.J.†	Liau, Z.L.	Roussell, H.V.
Cox, C.H., III	Lind, T.A.	Seielstad, D.A.
Diadiuk, V.	Missaggia, L.J.	Shiple, S.D.†
Donnelly, J.P.	Mull, D.E.	Tsang, D.Z.
Ferrante, G.A.	O'Donnell, F.J.	Walpole, J.N.
Groves, S.H.	Palmacci, S.T.	Woodhouse, J.D.
Harman, T.C.	Palmateer, S.C.	Yap, D.†
Hovey, D.L.		Yee, A.C.

* Staff Associate

† Research Assistant

ANALOG DEVICE TECHNOLOGY

R.W. Ralston, *Leader*

R.S. Withers, *Associate Leader*

Anderson, A.C.
Arsenault, D.R.
Bhushan, M.
Boisvert, R.R.
Brogan, W.T.
Denneno, A.P.
Dolat, V.S.
Fitch, G.L.

Frickey, J.M.
Green, J.B.
Holtham, J.H.
Lattes, A.L.
Lichtenwalner, D.J.*
Macedo, E.M., Jr.
Munroe, S.C.
Oates, D.E.

Pan, J.Y.*
Sage, J.P.
Seidel, M.N.*
Slattery, R.L.
Thompson, K.E.
Wong, S.C.*

MICROELECTRONICS

R.A. Murphy, *Leader*

E.D. Savoye, *Associate Leader*

D.J. Ehrlich, *Assistant Leader*

B.B. Kosicki, *Assistant Leader*

R.W. Chick, *Senior Staff*

Actis, R.
Astolfi, D.K.
Bales, J.W.*
Bennett, P.C.
Black, J.G.
Bozler, C.O.
Brown, E.R.
Burke, B.E.
Calawa, A.R.
Chen, C.L.
Chiang, A.M.
Clifton, B.J.
Daniels, P.J.
Doherty, C.L., Jr.
Doran, S.P.
Durant, G.L.
Efremow, N.N., Jr.
Felton, B.J.
Gajar, S.A.*
Geis, M.W.

Goodhue, W.D.
Gray, R.V.
Gregory, J.A.
Hollis, M.A.
Huang, J.C.M.
Johnson, B.W.
Johnson, K.F.
Kunz, R.R.
LaFranchise, J.R.
Lincoln, G.A., Jr.
Lyszcza, T.M.
Mahoney, L.J.
Maki, P.A.
Manfra, M.J.
Mathews, R.H.
McGonagle, W.H.
McIntosh, K.A.
Meingailis, J.†
Mountain, R.W.
Nichols, K.B.

Pang, S.W.
Parker, C.D.
Pichler, H.H.
Rabe, S.
Rathman, D.D.
Reich, R.K.
Reinold, J.H., Jr.
Rooks, M.J.
Rothschild, M.
Sedlacek, J.H.C.
Shaver, D.C.
Smith, F.W.*
Smythe, D.L., Jr.
Sollner, T.C.L.G.
Uttaro, R.S.
Vera, A.
Wilde, R.E.
Young, E.M.

* Research Assistant

† Part Time

1. SOLID STATE DEVICE RESEARCH

1.1 p^+ -AlInAs/InP DEPLETION-MODE JFET

We previously reported a selective molecular-beam-epitaxy (MBE) technique for fabricating enhancement-mode p^+ -AlInAs/InP field-effect transistors (FETs).¹ As shown in Figure 1-1, the basic device structure, for both enhancement- and depletion-mode FETs, consists of an ion-implanted n-type InP channel layer with a p^+ -gate layer formed by selective MBE growth of Be-doped AlInAs. Details of the fabrication procedures are described in Reference 1. In order to realize depletion mode (normally on) FETs, the n-type channel doping was increased from $2 \times 10^{16} \text{ cm}^{-3}$ to $8 \times 10^{16} \text{ cm}^{-3}$, and a 2000-Å undoped AlInAs buffer layer was incorporated as a Be diffusion barrier. Indiffusion of Be during MBE growth² was thought to contribute to the extremely low zero-gate-bias drain saturation current observed in devices fabricated without a buffer layer.¹

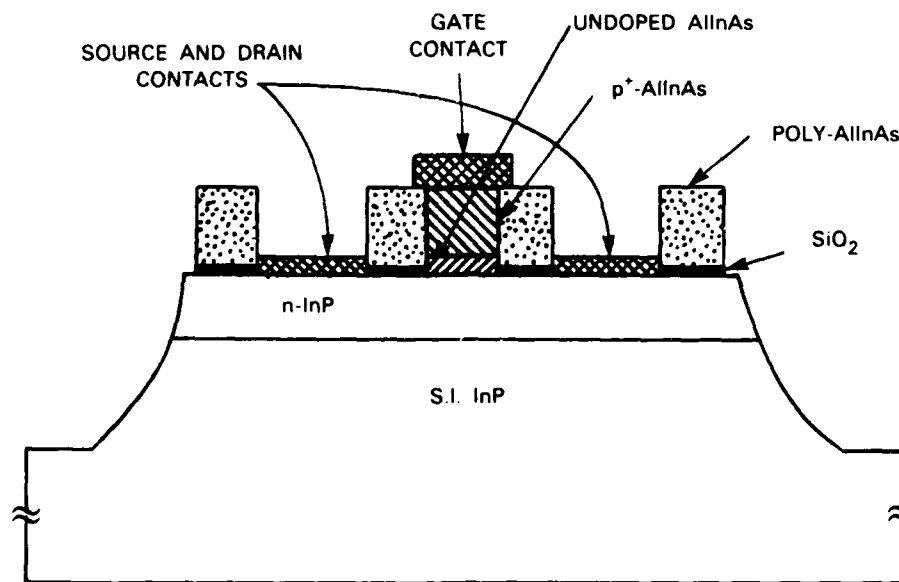


Figure 1-1. Schematic diagram of a p^+ -AlInAs/InP JFET showing the Si^+ -implanted n-InP and the MBE-grown AlInAs crystalline and polycrystalline regions.

For the present depletion-mode device, Figure 1-2 shows typical drain current-voltage (I-V) characteristics of a 4- μm -gate-length device having a source-to-drain spacing of 10 μm . The 200- μm -wide device exhibited a zero-gate-bias saturation current of 40 mA at a drain bias of 4 to 5 V and had a pinch-off voltage of about -8 V. The transconductance per unit gate width of several devices across the wafer was in the 32 to 42 mS/mm range. At a positive gate bias of 1 V (enhancement-mode operation), the saturation current and transconductance, as shown in

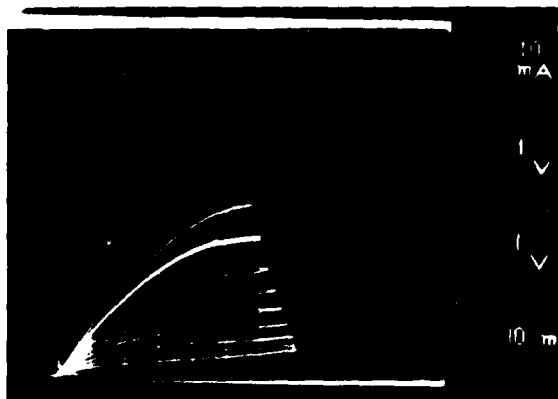


Figure 1-2. Typical I-V characteristics of a $4 \times 200\text{-}\mu\text{m}$ $p^+\text{-AlInAs/InP}$ JFET (with buffer layer). The zero-gate-bias curve is second from the top.

101818-2

Figure 1-2, increased to 50 mA and 50 mS/mm, respectively. Considering the long gate length and large source-drain spacing used, these values of scaled transconductance compare very favorably with conventionally fabricated InP JFETs.³⁻⁹ Although the transconductance and pinch-off voltage are quite reasonable, further improvement could be expected by reducing the substantial gate-source junction leakage current observed in these devices ($300\text{ }\mu\text{A}$ at pinch-off). One possible explanation for the high leakage is a large generation rate in the AlInAs buffer region. Other possibilities include interfacial trapping centers caused by a slight lattice mismatch and/or insufficient surface-cleaning procedures prior to MBE growth. The exact cause and remedy of this problem are still under investigation.

Selected $4\text{-}\mu\text{m}$ -gate-length devices were cleaved from the wafer and bonded to carrier packages for RF characterization. Small-signal microwave performance measurements showed a unity-power-gain frequency f_{max} of 3.2 GHz and a unity-current-gain frequency f_T of 2 GHz. Improvements in the high-frequency performance could be achieved by scaling down the gate length and employing additional source-drain implants to reduce parasitic resistance.

These results indicate that the selective growth method is a viable technique for fabricating high-frequency, high-power junction FETs in the InP-based materials system.

J.D. Woodhouse M.J. Manfra
J.P. Donnelly R.J. Bailey

1.2 REDUCTION OF INTERMODULATION DISTORTION IN INTERFEROMETRIC OPTICAL MODULATORS

In previous reports, it was shown theoretically¹⁰ and experimentally¹¹ that the dynamic range of analog optical-fiber communication links employing interferometric external optical modulators could be limited by modulator nonlinearities. Specifically, two-tone intermodulation (IM) distortion was investigated. Here, a dual-polarization technique for reducing IM distortion in interferometric modulators is described.

The dual-polarization optical link is illustrated in Figure 1-3 and consists of an optical source, an interferometric modulator, and an optical detector. It is assumed that the modulator supports single TE and TM modes. A polarizer (or polarization-preserving fiber) placed before the modulator is used to adjust the relative amounts of TE and TM input optical power. For each polarization, the output optical power P_{out} from the modulator can be expressed as

$$P_{out}(t) = \frac{P_{in}}{2} \left\{ 1 + \cos \left[\frac{\pi V_{in}(t)}{V_{\pi}} + \theta \right] \right\}$$

where $V_{in}(t)$ is the modulator drive voltage, V_{π} is the voltage change required for full on-off modulation, θ is a constant phase bias, and P_{in} is the input optical power. The detector output voltage $V_{out}(t)$ varies linearly with the sum of the two polarization components of the modulator output power.

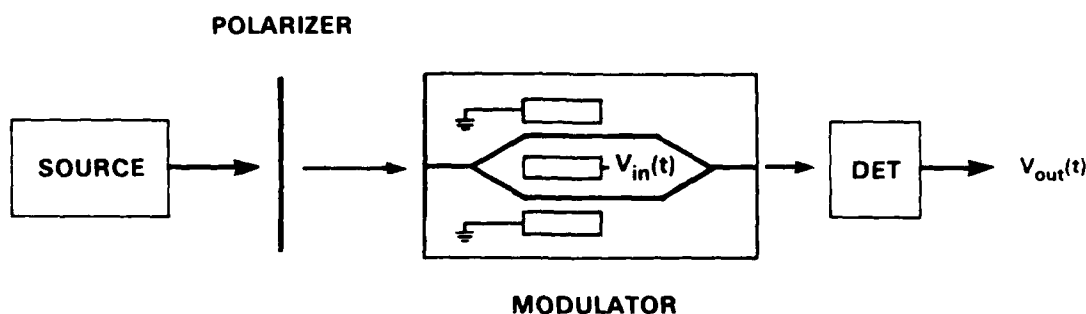


Figure 1-3. Analog optical communication link consisting of constant-power optical source, polarizer, interferometric modulator, and detector.

To analyze intermodulation distortion, it is assumed that the modulator drive voltage $V_{in}(t)$ consists of two simultaneous sinusoidal signals at frequencies ω_1 and ω_2 , each of amplitude V_m . As previously shown,¹⁰ for small depths of modulation the output power spectral amplitudes $P_{1,0}$ for the fundamentals (ω_1 and ω_2), and $P_{1,2}$ for the dominant intermodulation signals ($2\omega_2 - \omega_1$ and $2\omega_1 - \omega_2$), are given by the expressions

$$P_{1,0} \approx -\frac{1}{2} P_{in} \frac{\pi V_m}{V_{\pi}} \sin \theta + \text{higher-order terms}$$

$$P_{1,2} \approx -\frac{1}{16} P_{in} \left(\frac{\pi V_m}{V_{\pi}} \right)^3 \sin \theta + \text{higher-order terms}$$

indicating a dominant linear and cubic drive-voltage dependence at the fundamental and IM frequencies, respectively. Two sets of equations like those preceding describe the TE and TM responses.

Typically, an electro-optic modulator can be designed to provide different sensitivity for the two polarization components such that

$$V_{\pi}^{TM} = \gamma V_{\pi}^{TE}.$$

This difference in sensitivity can be exploited to suppress selectively the dominant cubic term of the IM distortion. This is accomplished by adjusting the two polarization components of the input optical power, P_{in}^{TE} and P_{in}^{TM} , and the phase bias, θ^{TE} and θ^{TM} , for each polarization such that

$$P_{in}^{TE} (V_{\pi}^{TM})^3 \sin \theta^{TE} = -P_{in}^{TM} (V_{\pi}^{TE})^3 \sin \theta^{TM}.$$

For a LiNbO_3 device, γ is typically about three; therefore if the dc phase biases are set to

$$\theta_{TM} = -\frac{\pi}{2}, \quad \theta_{TE} = \frac{\pi}{2},$$

then the ratio of TM to TE power would be ~ 27 for optimum third-order IM-distortion cancellation. Only the higher-order components of the $P_{1,2}$ IM distortion would remain. Since most of the input power is now TM-polarized, a consequence of this technique is a reduction in sensitivity at the fundamental frequency by approximately a factor of γ , as compared to using only TE-polarized light. However, significant increases in system dynamic range can be achieved, particularly for applications which have stringent IM-suppression requirements and are not limited by electrical drive power.

The total normalized electrical output power of the link at the fundamental and IM frequencies, as a function of the normalized modulator electrical drive power, is shown in Figure 1-4 by plotting $20 \log (|P_{kl}^{TE} + P_{kl}^{TM}| / P_{in})$ versus $20 \log (2V_m / V_{\pi}^{TE})$ for $P_{1,0}$ and $P_{1,2}$ where P_{in} is the total optical input power. The dashed lines indicate the results when all the input is TE-polarized, and the solid lines show the dual-polarization results for optimum IM distortion reduction with $\gamma = 3$. A normalized output power of 0 dB corresponds to full on-off modulation of the total optical power. As can be seen, a significant reduction in IM distortion can be achieved for a given depth of modulation at the fundamental frequency. As the depth of modulation decreases, the reduction in IM distortion increases. Likewise, if the IM suppression is specified, the fundamental output power from the detector can be substantially increased. As shown in Figure 1-4, a 9-dB increase in fundamental output power can be obtained with the dual-polarization technique if a 65-dB IM suppression level is specified.

Experimental results were obtained by means of a LiNbO_3 interferometric modulator designed for operation at $1.3 \mu\text{m}$. Two sinusoidal signals of equal amplitude at frequencies of 50 and 52 kHz were combined and applied to one set of electrodes on the device. A dc voltage was applied to a second electrode to adjust the relative TE and TM phase bias, and a polarizer was placed before the device input to adjust the relative optical input power between the two

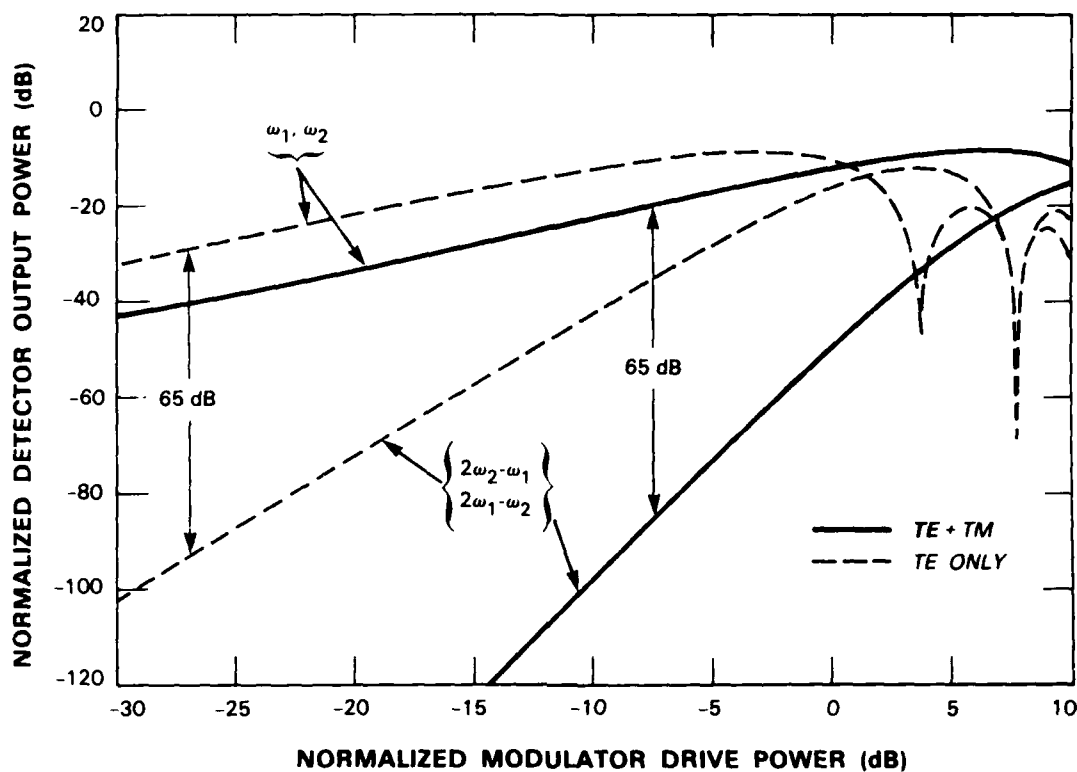


Figure 1-4. Plot of detector electrical output power level, $20 \log (|P_{k1}^{TE} + P_{k1}^{TM}| / P_{in})$, for the fundamental, $P_{1,0}$, and third-order IM product, $P_{1,2}$, as a function of modulator electrical drive power, $20 \log (2V_m / V_{\pi}^{TE})$. Dashed lines indicate single-polarization operation. Solid lines indicate optimized dual-polarization operation with $\gamma = 3$.

polarizations. Experimental and theoretical values of IM suppression for both single- and dual-polarization operation are shown in Table 1-1 for several values of electrical drive power. Theoretical values of the normalized fundamental output power of the link are also shown. For a given depth of modulation, the largest reduction in IM distortion measured was 21 dB, from -46 to -67 dB, at a normalized output power of ~ -20 dB.

L.M. Johnson

TABLE 1-1						
Summary of Experimental and Theoretical Results						
Drive Power 20 log (2V _m /V _π ^{TE})	Fundamental Output Power (dB) (Theory) (Normalized)		IM Suppression (dB)			
			TE Only		TE + TM	
	TE	TE + TM	Exp	Theory	Exp	Theory
-28	-31	-41	-65	-66		-145
-23	-26	-37	-55	-56		-125
-18	-21	-30	-46	-46		-100
-8	-11	-21	-23	-25	-67	-68
-2	-10	-16	-10	-11	-44	-44

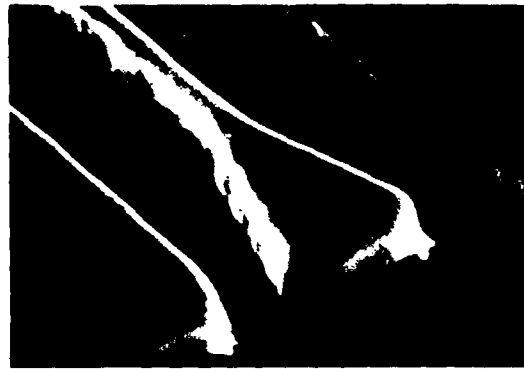
1.3 InGaAsP/InP BURIED-HETEROSTRUCTURE LASERS WITH CONCURRENTLY FABRICATED STRIPES AND MIRRORS

InGaAsP/InP buried-heterostructure (BH) lasers with noncleaved mirrors are suitable for monolithic integration and batch processing and have received considerable attention in recent years. High-performance lasers with good-quality mirrors have been demonstrated.¹²⁻¹⁶ However, the BH stripes and the mirrors were fabricated separately, in often complicated processes. We have developed a new fabrication process in which the laser stripe and the mirror are fabricated concurrently. Such a process not only is simpler and more controllable but also offers built-in alignment of the mirror and the stripe.

The laser-fabrication process involves the use of ion-beam-assisted etching (IBAE) to simultaneously define the laser stripes and mirrors, and mass transport to bury the active regions and smooth the mirrors at the same time. A similar process was used recently to demonstrate high-performance BH lasers with cleaved mirrors.¹⁷ In contrast to the previous process, the mass transport is carried out at a higher temperature of ~750°C for 0.5 to 2 h, which is needed to completely smooth the mirrors. Shown in Figure 1-5 is a scanning-electron-microscope (SEM) photograph of a laser mesa after mass transport. Typical mesas have vertical sidewalls and are 3 to 4 μm wide except at the end regions. The laser mesa shown has a tapered end region with a cylindrical mirror designed for reduced output beam divergence.¹⁸

The fabricated lasers have good operating characteristics. Nearly 70 percent of the lasers which have one flat etched and mass-transported mirror (with the other mirror cleaved) have threshold currents between 16 and 26 mA. These devices are 250 μm long and have active regions which are ~0.2 μm thick and 1.5 μm wide. Other lasers which have a 420-μm-long cavity

Figure 1-5. SEM perspective view of IBAE-defined cylindrical-mirror laser after etching and mass transport. The supporting mesa regions on either side of the laser mesa are also shown.



and both mirrors etched and mass-transported (with one mirror flat and the other mirror cylindrically curved) have threshold currents as low as 22 mA. The differential quantum efficiencies just above threshold are as high as 24 percent and are similar for output from the etched and the cleaved mirrors. Output powers >15 mW were measured from the uncoated etched mirrors. This performance is comparable to that obtained for lasers with wet-chemical-etched and mass-transported mirrors^{12,13} as well as for the best of the other InGaAsP/InP lasers with dry-etched mirrors.¹⁴⁻¹⁶

The far-field patterns in the junction plane of three devices with etched and mass-transported mirrors are shown in Figure 1-6. One device has a flat mirror and the other two have cylindrical mirrors. The beam divergence for the flat etched mirror is similar to that for a cleaved mirror. There is, however, a ± 20 percent device-to-device variation in the measured beam divergences for this wafer, probably due to variations in the active-layer thickness and width. As expected, cylindrical-mirror lasers with a larger value of L , the length of the tapered region, have a larger emitting spot and thus a smaller beam divergence. The full-width-at-half-maximum (FWHM) beam divergence is only 13° for the device with $L = 18 \mu\text{m}$. The cylindrical-mirror lasers can be designed to yield diffraction-limited beam divergences by properly choosing the radius of curvature R of the mirror with respect to L . An approximate, Gaussian-mode analysis can be used to estimate the beam divergence. Based on such an analysis, the predicted beam divergences are 10.5° for a device with $R = 12$ and $L = 18 \mu\text{m}$, and 19° for a device with $R = 8$ and $L = 8 \mu\text{m}$. The predicted divergences are slightly lower than the measured values shown in Figure 1-6, since the idealized Gaussian modes have the smallest beam divergence.

It is worth noting that the large-numerical-aperture cylindrical mirrors achieved here cannot be formed by wet-chemical etching, as the latter results in sloped sidewalls and severely distorted mirror shapes because of the crystallographic orientation dependence of the etching. The present use of dry etching also makes possible concurrent fabrication of the mirrors and the stripes, since the narrow stripe mesas have vertical sidewalls and result in narrow transported regions (needed

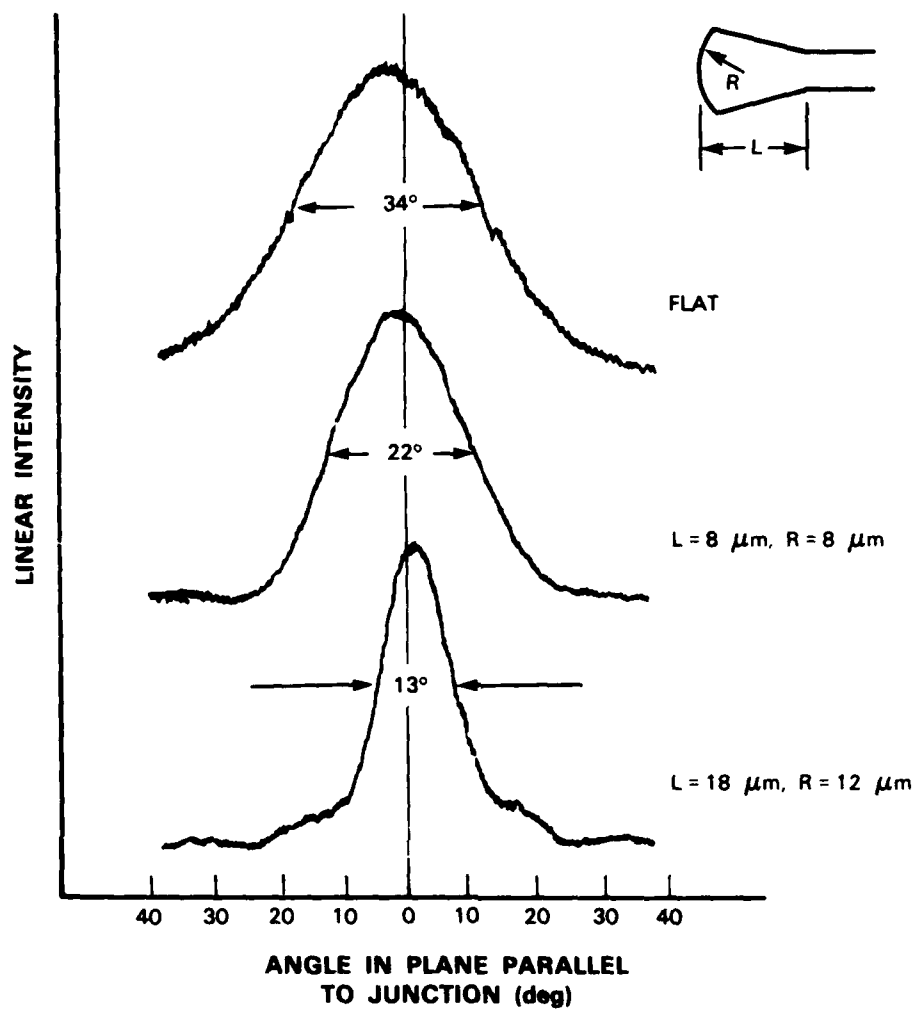


Figure 1-6. Far-field patterns of IBAE-defined etched-mirror lasers.

for low current leakage) even at the high mass-transport temperature used for smoothing the mirrors. In conclusion, the present concurrent fabrication technique offers advantages such as built-in mirror-stripe alignment and controlled fabrication of highly curved mirrors as demonstrated by the fabrication of lasers with small and predictable beam divergences.

D. Yap
J.N. Walpole
Z.L. Liao

1.4 Y-JUNCTION-COUPLED InGaAsP/InP BURIED-HETEROSTRUCTURE LASER ARRAYS

In recent years, much effort has been devoted to the development of coherent diode laser arrays. An effective method for coupling these lasers involves the incorporation of Y-junctions to connect the lasing stripes.¹⁹ This coupling scheme favors the excitation of the in-phase array modes rather than the 180° out-of-phase modes favored by other array structures. Here we report the first coherent arrays of InGaAsP/InP BH lasers that are coupled by Y-junctions. In contrast to previously reported coherent InGaAsP/InP laser arrays,²⁰⁻²² the present arrays are strongly index-guided and have the potential for low threshold currents and stable, single-lobe outputs at high powers.

A schematic illustration of the Y-junction-coupled array structure is shown in Figure 1-7(a). The arrays have eight stripes on one end and nine stripes on the other end. The mesa structure was fabricated by the combined use of IBAE and mass transport with which high-performance single-stripe lasers have recently been demonstrated.¹⁷ The capability of the dry-etching technique to form narrow grooves with vertical sidewalls without regard for the crystallographic orientation is crucial to the fabrication of the present array structure, because relatively closely spaced mesa stripes and sharply defined Y-junctions can be formed. Smaller stripe spacings result in improved array fill factors and, thus, fewer lobes in the far-field pattern. More sharply defined Y-junctions yield lower losses and stronger coupling. Figure 1-7(b) shows a top view of an IBAE-defined laser mesa pattern. The stripes are 2 μm wide and have a spacing of 6 μm . The branch angle of each Y-junction is 10°. Such a structure cannot be defined by conventional wet-chemical etching techniques (which are dependent on the crystallographic direction), since the mesa sidewalls would be sloped and thus the Y-junctions would be severely blunted.

The far-field pattern from the eight-stripe end of a Y-junction-coupled array is shown in Figure 1-8. This array has a threshold current of 300 mA and is 470 μm long. Since typical threshold currents measured for 400- μm -long single-stripe lasers from the same wafer are 26 mA, we estimate that the increase in the threshold current due to scattering and mode-mismatch losses at the Y-junctions is 25 to 30 percent. Note that the stripes emit primarily in-phase rather than 180° out-of-phase. The presence of the strong narrow lobes in the far-field pattern indicates that good coherence between the lasing stripes has been achieved.

Spatially resolved emission spectra indicate that most of the stripes emit in several longitudinal modes. At most, 4 to 5 stripes are phase-locked at a given longitudinal mode. Also, for a given longitudinal mode the power in the various locked stripes is not the same. The 4° FWHM divergence of the central far-field lobe shown in Figure 1-8 is consistent with these observations. Power in the non-phase-locked longitudinal modes contributes to the baseline seen in the far-field pattern. Improved phase-locking which extends over more stripes can probably be obtained by the use of more uniform wafers and improved photolithographic definition of the stripes and branches.

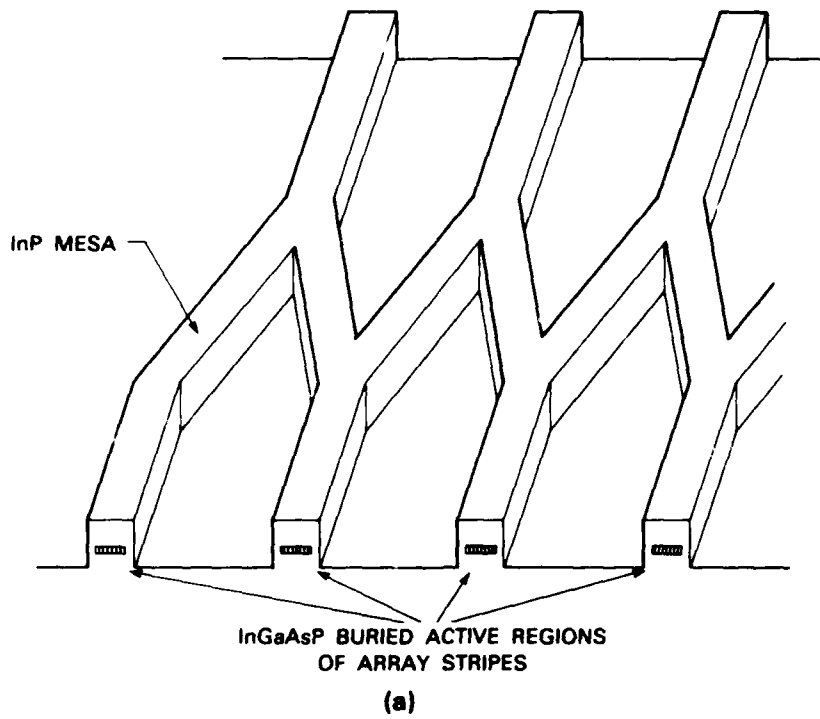


Figure 1-7. Y-junction-coupled laser array: (a) schematic illustration, and (b) top view of a portion of an IBAE-defined mesa.

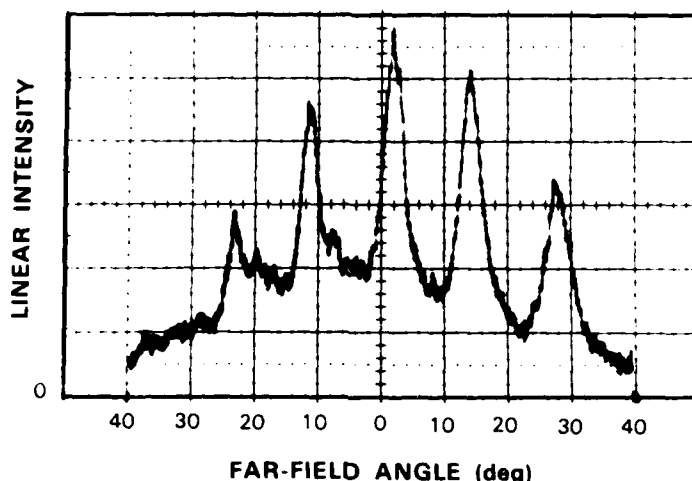


Figure 1-8. Far-field pattern in the junction plane of a Y-junction-coupled laser array. The laser was excited at 1.5 times the threshold current.

The number of far-field lobes emitted by the Y-junction-coupled laser array can be decreased by improving the fill-factor of the array. This can be achieved by fabricating cylindrical mirrors at the ends of each stripe. The cylindrical mirrors can be fabricated by IBAE and mass transport in the same process steps as the stripes (see Section 1.3).

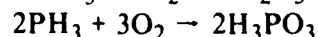
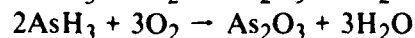
In conclusion, we have demonstrated coherent linear arrays of mass-transported InGaAsP/InP BH lasers. These Y-junction-coupled arrays show in-phase emission and strong phase coherence.

D. Yap
J.N. Walpole
Z.L. Liao

1.5 HYDRIDE ADSORPTION ON IMPREGNATED CARBON

The incomplete pyrolysis of the hydrides arsine (AsH_3) and phosphine (PH_3) in organometallic-vapor-phase-epitaxial (OMVPE) growth systems can result in significant environmental release of these highly toxic materials. This study was conducted to determine if adsorption of these materials on impregnated carbon is a safe and effective way to control emissions of arsine and phosphine from OMVPE systems.

Carbons impregnated with copper, chromium, and silver catalyze hydride oxidation. For arsine and phosphine, the appropriate reactions are thought to be:²³



where the reactions as shown are exothermic, liberating in excess of 200 kcal/gmol.

Existing data in the literature could not be used because they apply to adsorption of very dilute quantities (ppm level) of the hydrides in air, characteristic of large industrial ventilation systems. OMVPE systems, on the other hand, typically operate with relatively low flows (10 to 100 slpm) of a strongly reducing carrier gas (H_2) containing ~1 percent hydride. Scrubbing the unpyrolyzed hydrides under these conditions is best accomplished by a two-step process, with the first being primarily physical and chemical adsorption of the hydride on the carbon during the actual OMVPE run. Then the carbon bed is oxidized to convert the hydrides to arsenic oxides and/or phosphoric acid by the reactions shown above. Chemisorption and oxidation of the hydride are necessary to prevent desorption.²⁴

Our studies were carried out with a test cell which consisted of a stainless steel canister which held 400 g carbon.[†] The canister, 7.5-cm diam. by 35 cm long, was a size that could readily be incorporated into the exhaust plumbing of most OMVPE systems. It had a removable top with metal-seal flange for replacing the carbon charge and thermocouples inserted radially into the carbon at four different bed heights. These proved useful for tracking the adsorption and oxidation reactions as they progressed along the direction of flow. The exhaust from the cell was monitored for the hydride concentration.[‡]

Initial studies were conducted to determine how bed depth and flow affected the carbon capacity for arsine. Oxidation was then studied by flowing air through the cell, and bed temperatures were measured for different air flows. During the third phase of this work, the test cell was attached to an OMVPE system and placed in the exhaust section following particulate filters used to remove arsenic and phosphorus. In this configuration, the total carbon capacities for arsine and phosphine were obtained from the repeated use of the two-step, adsorption-oxidation process.

These studies showed that increasing the residence time of the arsine in the bed, either by decreasing the flow or increasing the bed depth, increased the weight percent of arsine adsorbed on the bed. In all runs, no arsine was detected (<5 ppb) at the output of the test cell until breakthrough occurred, and then concentrations rapidly increased and went above the saturation limit of the hydride monitor (5 ppm). Desorption of arsine was found to occur when inert gas was used to purge the bed before oxidation.

During oxidation, restricting the air flow through the cell to 250 sccm or less kept the bed temperatures below 180°C, as recommended by the carbon manufacturer. Greater air flows produce higher temperatures and increase the risk of bed ignition. The thermocouples were useful both for establishing an acceptable air flow and indicating the completion of the reaction. Oxidation rejuvenated the bed even though no measurable desorption occurred.

[†]The impregnated carbon used in all the experiments reported here was Calgon Corp., Type ASC 12 × 30 mesh.

[‡]Hydrides were sensed with the MDA Scientific Co., Model 7100 monitor.

Figure 1-9 shows the results of the multiple run tests made with the test cell on the OMVPE system. In these, 10 slpm hydrogen containing 1 percent arsine or phosphine were passed through the 400-g bed (18 cm deep). The adsorption run was terminated when a thermocouple 5 cm from the cell outlet peaked in temperature (typically 60°C). With this as an endpoint criterion, rather than hydride breakthrough, little or no desorption occurred during purging and oxidation, and a more accurate determination could be made of the total hydride adsorbed. After the bed was purged with nitrogen, 250 sccm air was passed through the cell until oxidation was complete (bed temperatures back down to below 30°C). The adsorption step was then repeated. As shown in Figure 1-9, the bed capacity dropped off slowly, and six runs with the same carbon charge were possible in both the arsine and phosphine adsorption experiments. On the final runs, low levels of hydride were detected in the exhaust throughout the run. The total carbon adsorption weight capacities were 19 percent phosphine and 39 percent arsine.

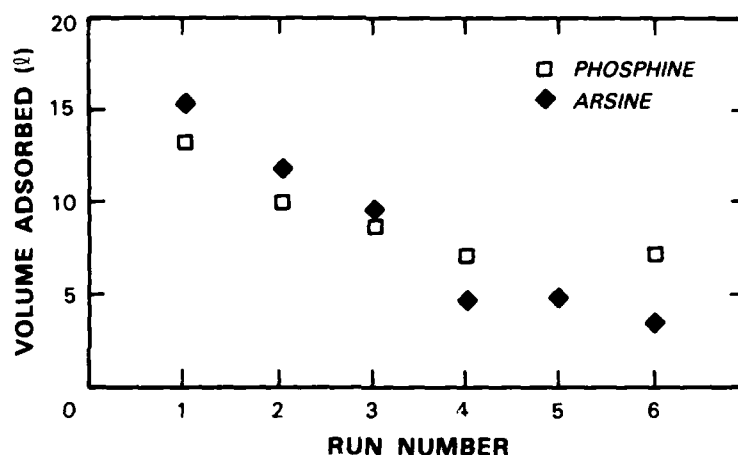


Figure 1-9. Volume of hydride adsorbed during six adsorption/oxidation runs. (The fifth run of the phosphine adsorption test was inadvertently run at a different concentration and the volume was not accurately determined. For purposes of determining the total capacity, the volume adsorbed was assumed to be the same as during the fourth and sixth runs.)

In summary, we have used impregnated carbon to safely and effectively control arsine and phosphine emissions from OMVPE systems. Concentration, flow, and bed depth affect the amount of hydride that can be adsorbed before breakthrough occurs. Imbedded thermocouples are useful for monitoring hydride adsorption to prevent breakthrough and minimize desorption. Oxidation increases total adsorption capacity, but it must be controlled to prevent overheating. After oxidation, hydrides could not be detected when the cell was purged or when it was opened for carbon removal. A full account of these experiments is presented elsewhere.²⁵⁻²⁶

P.L. Greenley†
S.C. Palmateer
S.H. Groves

†MIT Environmental Medical Service, Industrial Hygiene Office.

REFERENCES

1. Solid State Research Report, Lincoln Laboratory, MIT (1987:3), p.1, DTIC AD-A192837.
2. J.D. Oberstar, B.G. Streetman, J.E. Baker, and P. Williams, J. Electrochem. Soc. **129**, 1312 (1982).
3. J.B. Boos, H.B. Dietrich, T.H. Weng, K.J. Slegler, S.C. Binari, and R. L. Henry, IEEE Electron Device Lett. **EDL-3**, 256 (1982).
4. J.B. Boos, S.C. Binari, G. Kelner, P.E. Thompson, T.H. Weng, N.A. Papanicolaou, and R.L. Henry, IEEE Electron Device Lett. **EDL-5**, 273 (1984).
5. J.D. Woodhouse and J.P. Donnelly, IEEE Electron Device Lett. **EDL-7**, 387 (1986).
6. C.L. Chen, K.W. Wang, and S.M. Parker, IEEE Electron Device Lett. **EDL-8**, 483 (1987).
7. S.J. Kim, K.W. Wang, G.P. Vella-Coleiro, J.W. Latze, Y. Ota, and G. Ruth, IEEE Electron Device Lett. **EDL-8**, 528 (1987).
8. J.B. Boos, T.H. Weng, S.C. Binari, G. Kelner, and R.L. Henry, IEDM Tech. Digest (1983), pp. 625-627.
9. C. Fan and P.K.L. Yu, Electron. Lett. **23**, 981 (1987).
10. Solid State Research Report, Lincoln Laboratory, MIT (1986:2), p.1, DTIC AD-A180799.
11. *Ibid.* (1987:2), p. 7, DTIC AD-A188388.
12. Z.L. Liao, J.N. Walpole, and D.Z. Tsang, Appl. Phys. Lett. **44**, 945 (1984), DTIC AD-A147996.
13. Z.L. Liao and J.N. Walpole, Appl. Phys. Lett. **50**, 528 (1987), DTIC AD-A180887.
14. H. Saito, Y. Noguchi, and H. Nagai, Electron. Lett. **22**, 1157 (1986).
15. L.R. Harriott, R.E. Scotti, K.D. Cummings, and A.F. Ambrose, J. Vac. Sci. Technol. B **5**, 207 (1987).
16. N. Bouadma, J.F. Hogrel, J. Charil, and M. Carre, IEEE J. Quantum Electron. **QE-23**, 909 (1987).
17. D. Yap, Z.L. Liao, D.Z. Tsang, and J.N. Walpole, accepted by Appl. Phys. Lett.
18. J.N. Walpole, Z.L. Liao, L.J. Missaggia, and D. Yap, Appl. Phys. Lett. **50**, 1219 (1987).
19. D.F. Welch, W. Streifer, P.S. Cross, and D.R. Scifres, IEEE J. Quantum Electron. **QE-23**, 752 (1987), and references therein.

20. E. Kapon, Z. Rav-Noy, S. Margalit, and A. Yariv, J. Lightwave Technol. **LT-4**, 919 (1986), and references therein.
21. M. Razeghi, R. Blondeau, M. Krakowski, B. deCremoux, J.P. Duchemin, F. Lozes, M. Martinot, and M.A. Bensoussan, Appl. Phys. Lett. **50**, 230 (1987).
22. D. Botez, T. Pham, and D. Tran, Electron. Lett. **23**, 417 (1987).
23. W.G. Schuliger, Calgon Corp., private communication.
24. G. Haache, J.S. Brinen, and H. Burkhard, J. Electrochem. Soc. **135**, 715 (1988).
25. P.L. Greenley, Proc. American Industrial Hygiene Conference, Montreal, Canada, 1987.
26. P.L. Greenley, S.C. Palmateer, and S.H. Groves, to be published.

2. QUANTUM ELECTRONICS

2.1 MODELING OF Q-SWITCHED, FOUR-LEVEL LASERS WITH NONZERO LOWER-LEVEL LIFETIME

A simple model to describe Q-switched, four-level lasers with nonzero lower-level lifetime has been developed and used to evaluate efficiency in Nd³⁺ lasers. A typical assumption in modeling Q-switched Nd³⁺ lasers is that the lower-laser-level relaxation rate is infinitely fast, but this assumption is not supported by experimental measurements of this lifetime, which have ranged from 10 ns to 1 μ s. Some attempts have been made to include the effect of the relaxation in models of Q-switched Nd³⁺ lasers,¹ but the energy level structure of the Nd³⁺ ion was not properly taken into account. Our model shows that the extraction efficiency, which is the fraction of the upper manifold population that becomes extracted by photons, depends on the ratio of the initial upper-state population density to the threshold population density, the ratio of the lower-laser-level lifetime to the cavity lifetime, and Boltzmann occupation factors of the laser transition. If the lower-level lifetime is much longer than the cavity lifetime, the model predicts that the efficiency of a 1.064- μ m Nd:YAG laser is only 68 percent of that expected in the case of infinitely fast lower-level relaxation.

The energy level diagram of the laser and ground-state manifolds for the 1.06- μ m Nd:YAG transition is shown in Figure 2-1. It is assumed that the lower laser level is unoccupied in thermal equilibrium because it is sufficiently above the ground state. It is also assumed that the crystal field levels within each manifold are in quasi-thermal equilibrium at all times and, thus, their populations are Boltzmann distributed. The laser transition is between two crystal field levels *u* and *l* that have degeneracies *g_u* and *g_l* and population densities *N_u* and *N_l*, respectively. The ratios of *N_u* and *N_l* to the respective total manifold populations are constants *f_u* and *f_l* determined by the Boltzmann distribution.

The starting point of the model is the laser rate equations

$$\frac{d\phi}{dt} = \phi \left[c\sigma \left(N_u - \frac{g_u}{g_l} N_l \right) \frac{L}{L'} - \frac{\delta}{t_r} \right] \quad , \quad (2-1a)$$

$$\frac{dN_u}{dt} = -f_u \left(N_u - \frac{g_u}{g_l} N_l \right) c\sigma\phi \quad , \quad (2-1b)$$

and

$$\frac{dN_l}{dt} = f_l \left(N_u - \frac{g_u}{g_l} N_l \right) c\sigma\phi - \frac{N_l}{\tau_l} \quad . \quad (2-1c)$$

Here *t* is time, σ is the stimulated emission cross section, τ_l is the lifetime of the lower laser level, ϕ is the cavity photon density, *c* is the speed of light, *L* is the length of the gain medium, *L'* is the cavity length, *t_r* is the cavity round-trip time, and δ is the fractional cavity loss per round trip. In Nd:YAG all energy levels have a degeneracy of 2. By appropriate substitutions, these rate equations can be written in terms of dimensionless quantities.

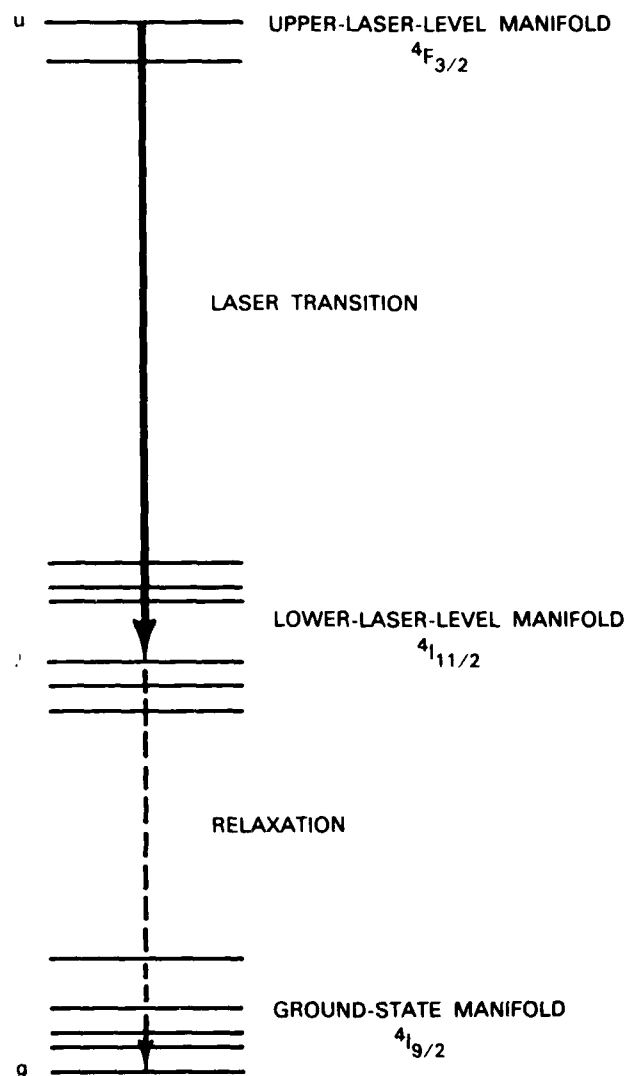


Figure 2-1. Energy level diagram of the 1.064- μm Nd:YAG transition.

101818-7

The rate equations have been solved numerically. It has been assumed that $N_l(0) = 0$ and that $\phi(0)$ is small compared to the peak value of $\phi(t)$. The ratio r , given by $r = N_u(0)/N_t$, where N_t is the threshold population density, has been varied. The extraction efficiency η_{ex} is the ratio of the total number of stimulated photons to the total initial upper manifold population given by $N_u(0)/f_u$. The number of stimulated photons is calculated by determining the rate of stimulated emission and integrating over all time.

Figure 2-2 shows $\eta_{\text{ex}}(r, \tau)$ for the 1.064- μm transition in Nd:YAG at room temperature as a function of r and τ , where τ is the ratio of τ_l to the cavity lifetime τ_c given by t_r/δ . We can see

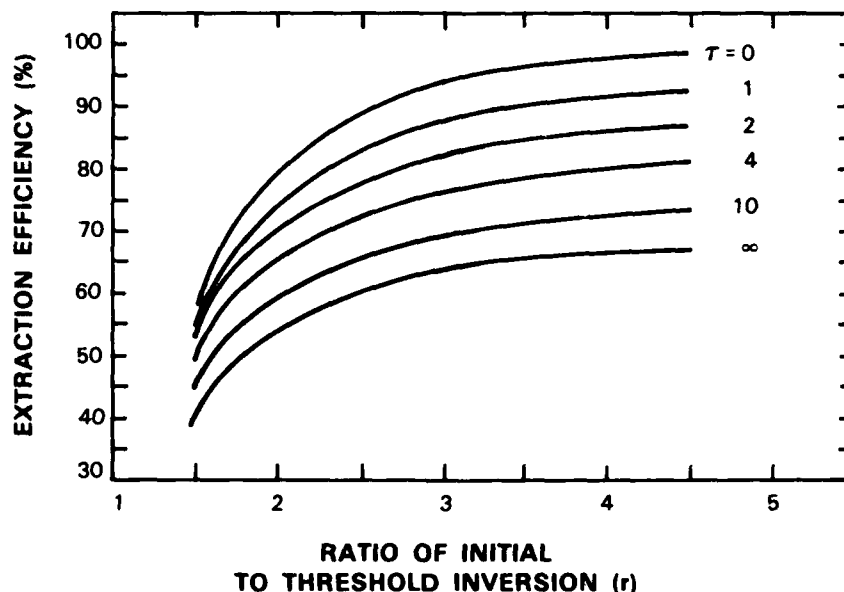


Figure 2-2. Extraction efficiency as a function of the ratio r of the initial population inversion density to the threshold inversion density and the ratio τ of the lower-laser-level lifetime to the cavity lifetime.

that the nonzero lower-laser-level lifetime can reduce extraction efficiency substantially. In the worst case of $\tau = \infty$,

$$\eta_{ex}(r, \infty) = \eta_{ex}(r, 0) f_u / (f_u + f_l) \quad (2-2)$$

and $\eta_{ex}(r, \infty)$ is reduced by 68 percent relative to $\eta_{ex}(r, 0)$ in Nd:YAG. Typical cavity lifetimes for Q-switched Nd³⁺ lasers are 10 ns or less. Thus, even with the most optimistic estimate of lower-laser-level lifetime in Nd:YAG, $\tau > 1$.

In summary, modeling shows that nonzero lower-laser-level lifetime in Nd³⁺ lasers can reduce extraction efficiency in Q-switched lasers. It may be possible to ameliorate this problem by finding laser materials with either higher lower-state relaxation rates or more favorable Boltzmann occupation factors.

T.Y. Fan

2.2 INTRACAVITY FREQUENCY MODULATION OF Nd:YAG LASER RADIATION

Intracavity frequency modulation of laser radiation has attracted attention since it was first demonstrated in 1964.²⁻⁵ This modulation has several potential applications including spectroscopy⁶⁻⁹ and optical metrology.¹⁰ Our interest in frequency-modulated lasers stems from our desire for a Nd:YAG laser that operates over a wide spectral range and yet emits radiation simultaneously at each allowed cavity frequency over this range.¹¹⁻¹⁴

Intracavity frequency modulation of laser radiation may be accomplished by modulating the voltage on an intracavity electro-optic crystal at very nearly (but not exactly) the longitudinal-mode frequency interval of the laser cavity. Under ideal conditions, the result of this modulation produces a laser radiation field given by

$$E = E_0 \cos (\omega t + \Gamma \sin \omega_m t) \quad (2-3)$$

where ω is the carrier frequency, ω_m is the modulation frequency, and Γ is the depth of frequency modulation. The depth of frequency modulation is given by

$$\Gamma = (\delta / \pi) \omega_c / (\omega_c - \omega_m) \quad (2-4)$$

where δ is the depth of modulation for a single laser round trip (proportional to the modulating voltage applied to the electro-optic crystal) and $\omega_c = \pi c / L$ is the laser cavity mode spacing expressed in terms of the cavity length L and the velocity of light c . Equation (2-3) may be rewritten in terms of Bessel functions as

$$E = E_0 \sum_{n=-\infty}^{\infty} J_n (\Gamma) \cos[(\omega + n\omega_m)t] \quad (2-5)$$

The frequency spectra of the modulated laser consist of a series of frequencies ω_n separated by the modulation frequency ω_m , and with powers proportional to the square of the Bessel functions $J_n(\Gamma)$. Figure 2-3 shows the theoretical spectral power distribution of frequency-modulated radiation at various depths of modulation both for a single carrier frequency and for two carrier frequencies corresponding to adjacent cavity modes. The frequency extent of the modulated radiation is $2\Gamma \omega_m$.

By inserting a LiNbO_3 phase modulation crystal inside a $1.32\text{-}\mu\text{m}$ Nd:YAG laser cavity, we have obtained frequency modulation of the laser output radiation. Figure 2-4 illustrates the spectral profiles of the Nd:YAG laser at various levels of modulation voltage applied to the LiNbO_3 crystal. These spectral profiles were measured by a scanning confocal Fabry-Perot spectrum analyzer with a free-spectral range of 8 GHz and a finesse of about 200. The depth of modulation of each spectral profile was obtained by comparing that profile with theoretically generated spectral profiles. At zero applied modulation, the Nd:YAG laser operated on three adjacent longitudinal cavity modes in the TEM_{00} mode with an output power of 500 mW. Applying a sufficiently strong modulation voltage ($>5 \text{ V}_{\text{rms}}$) greatly improved the coherence of the laser output. This is illustrated by the top two spectral plots in Figure 2-4(a). In the free-running state the adjacent cavity modes operate incoherently relative to one another, while in the frequency-modulated state the output radiation is completely coherent and consists of a single carrier frequency with side-band frequencies on both sides. Doubling the modulation voltage gave a spectral profile that could not be fit by the Bessel function spectrum of a single modulated carrier frequency. However, a good theoretical fit was possible by assuming two carrier frequencies corresponding to adjacent laser cavity modes and that these dual carriers were incoherent relative to one another. At higher modulation voltages, the spectral profiles could usually be matched to theoretical profiles by assuming either single or dual adjacent carrier frequencies. In many cases, the laser would

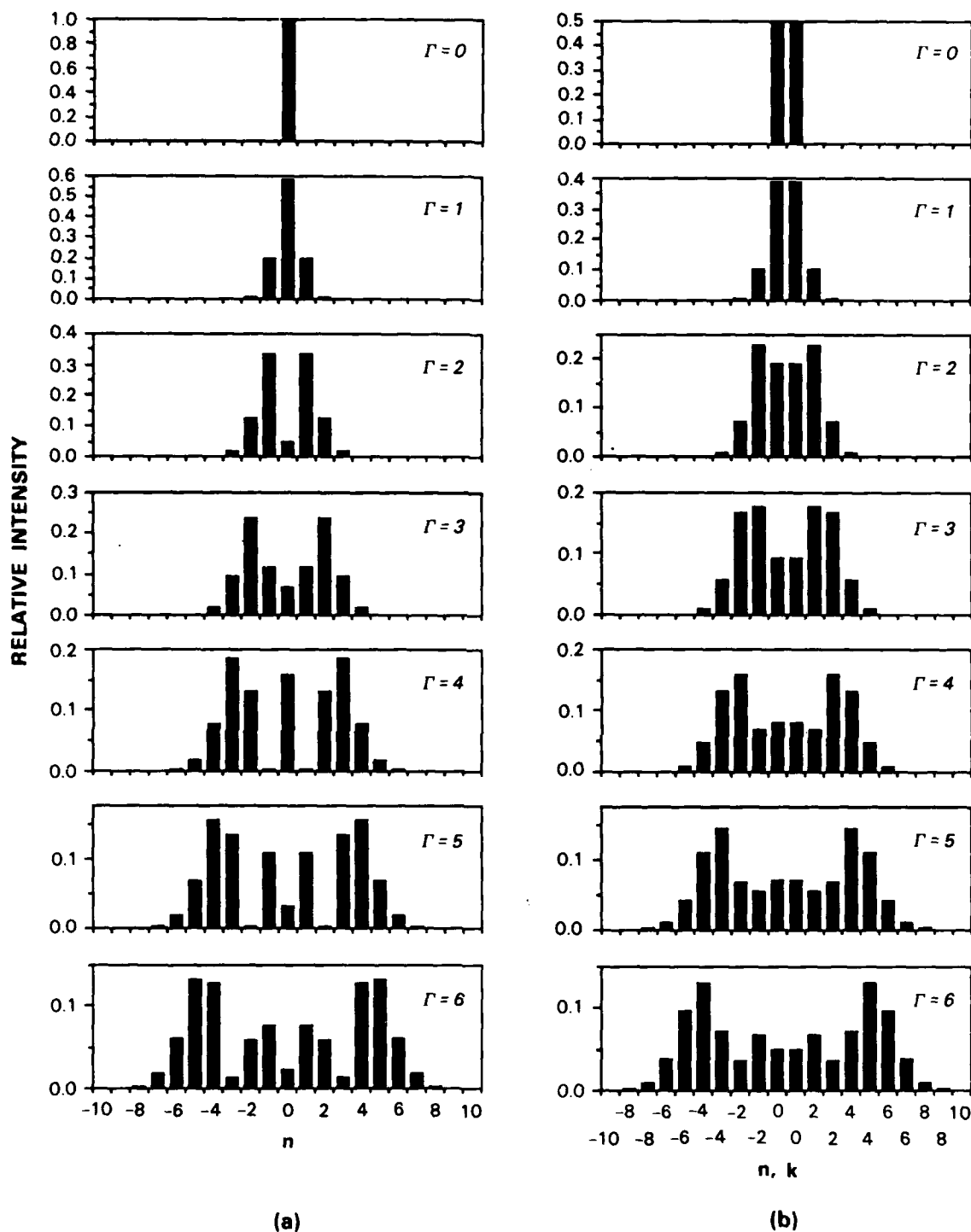


Figure 2-3. Calculated frequency-modulation spectra for various depths of modulation Γ : (a) single carrier frequency ω_0 ; $\omega = \omega_0 + n\omega_m$ and (b) two carrier frequencies ω_0 and ω_0' corresponding to adjacent cavity modes; $\omega_n = \omega_0 + n\omega_m$ and $\omega_k' = \omega_0' + k\omega_m$. The two carrier frequencies are assumed to be incoherent relative to one another. For the purpose of this figure, the sideband intensities of nearly the same frequency from different carrier frequencies are added incoherently.

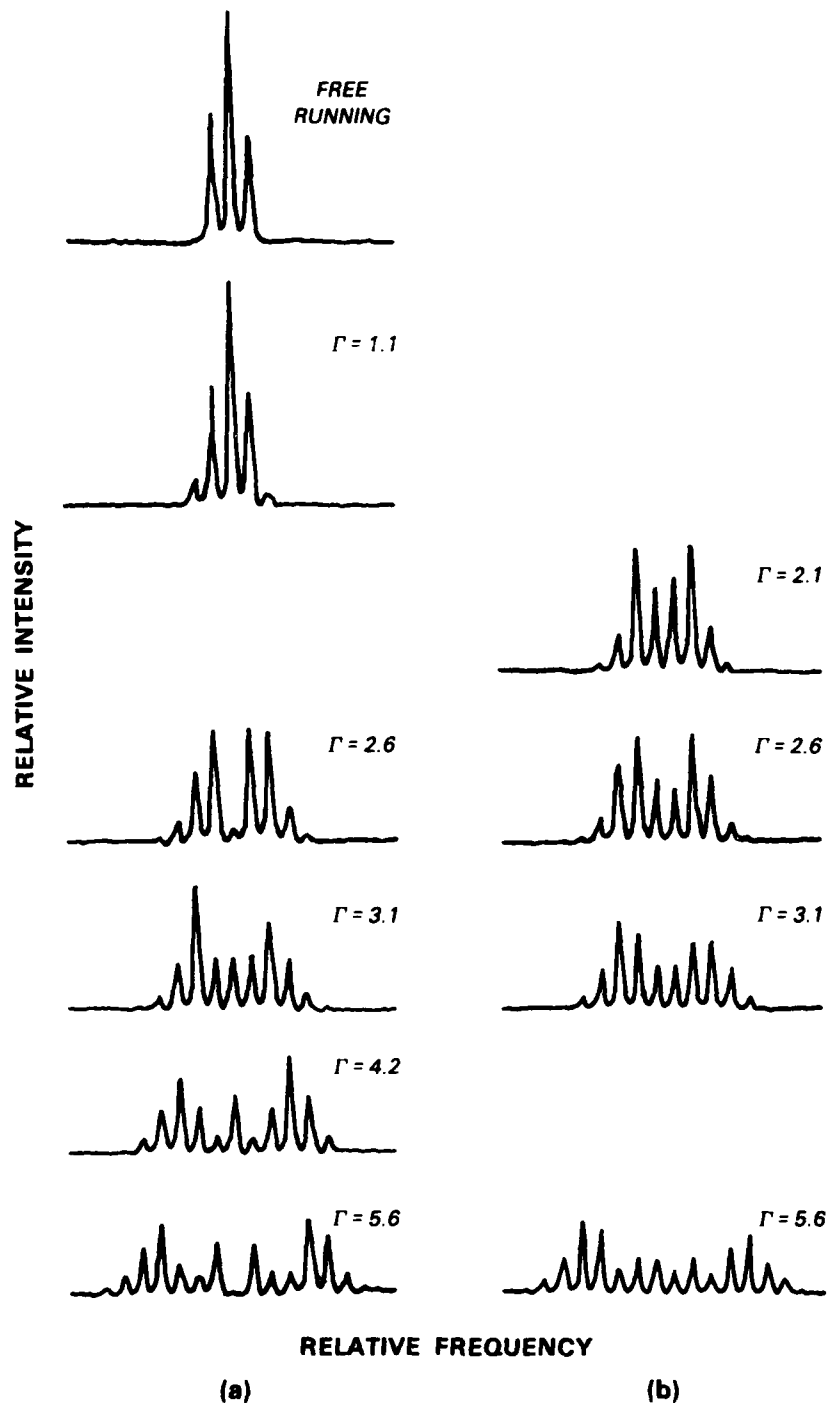


Figure 2-4. Measured frequency-modulation spectra of a 1.32- μm Nd:YAG laser for various depths of modulation Γ . The laser had a cavity mode spacing of 150.000 MHz and was modulated at 149.800 MHz. (a) Spectral profiles of the frequency-modulated laser when operating with a single carrier frequency. The laser free-running spectral profile is shown in the uppermost plot. (b) Spectral profiles of the frequency-modulated laser when operating with two carrier frequencies corresponding to adjacent cavity modes.

operate on either single or dual carrier frequencies depending sensitively on the laser cavity alignment. Most often, the laser appeared to operate on dual adjacent carrier frequencies.

Figures 2-5 and 2-6 show the experimentally measured dependence of the depth of modulation on both modulation voltage and frequency. As can be seen, the dependence is in good qualitative agreement with that expected from Equation (2-4).

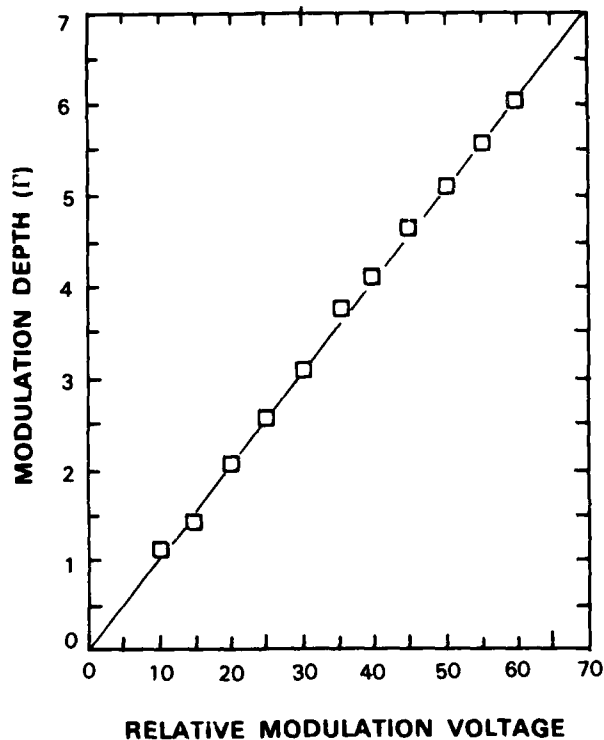


Figure 2-5. Measured depth of frequency modulation Γ as a function of the relative sinusoidal drive voltage applied to the intracavity LiNbO_3 crystal.

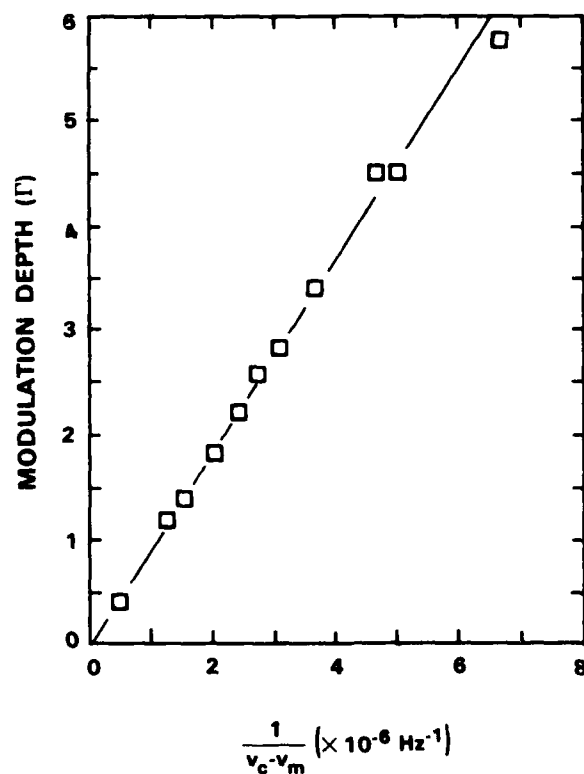


Figure 2-6. Measured depth of frequency modulation Γ as a function of the inverse of the difference between the cavity mode spacing ($\nu_c = \omega_c/2\pi$) and the modulation frequency ($\nu_m = \omega_m/2\pi$).

An interesting demonstration of the coherence of a frequency-modulated laser was obtained by sum-frequency mixing the output of two frequency-modulated Nd:YAG lasers, one operating at 1.06 and the other at 1.32 μm . Each Nd:YAG laser was modulated with the same depth and frequency but with a 180° phase difference. Sum-frequency mixing the radiation from these frequency-modulated lasers in a nonlinear crystal gives an unmodulated sum frequency.¹⁵ Figure 2-7 shows the spectral profiles of both Nd:YAG lasers and of the sum radiation for both 180° and 0° phase differences between the two Nd:YAG laser modulations.

T.H. Jeys

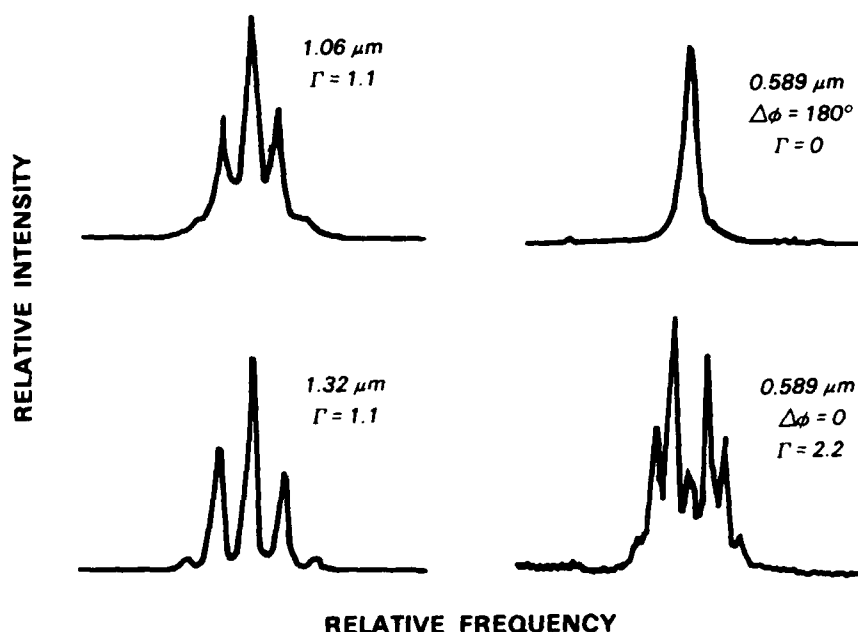


Figure 2-7. Spectral profiles of frequency-modulated 1.06- and 1.32- μm Nd:YAG lasers and their sum radiation at 0.589 μm . The modulation depth of the sum radiation could be varied from zero to twice that of the Nd:YAG laser by adjusting the phase difference $\Delta\phi$ between the two laser modulations. The single-frequency result at $\Delta\phi = 180^\circ$ confirms that each Nd:YAG laser was operating with a single carrier frequency.

2.3 MEASUREMENT OF DOUBLING EFFICIENCY USING 150- μs MACROPULSES FROM A Nd:YAG LASER

A long-pulse Nd:YAG laser system has been modified during the last three months to produce mode-locked pulse envelopes (macropulses) with durations between 10 and 200 μs . The ability to operate with mode-locked pulse envelopes of 1 to 2 μs to resemble the large multibeam laser system has also been maintained.

Initial frequency-doubling experiments with this newly modified system were carried out with 150- μs macropulses having the temporal envelope shown in Figure 2-8. This pulse length is of particular interest since it can serve as a pump for a $\text{Ti:Al}_2\text{O}_3$ laser emitting 150- μs pulses to simulate a diode array. At this pulse length, the Nd:YAG laser produces a macropulse energy of almost 2 J. However, thermal birefringence when the laser system is operating at 10 Hz produces a depolarizing effect which reduces the useful energy for frequency conversion to 1.3 to 1.4 J per pulse.

Second harmonic generation (SHG) experiments were carried out to establish the capabilities of various nonlinear crystals for frequency doubling with the laser operating in this 150- μs configuration. For these experiments the laser beam was reduced to a diameter of ~ 1 mm. The results obtained with the various crystals are summarized below.

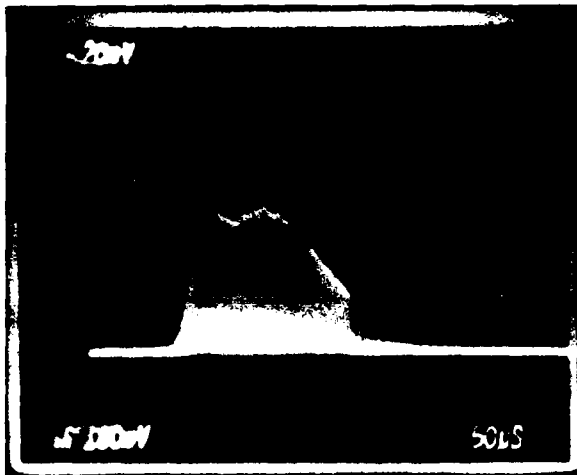


Figure 2-8. Oscilloscope trace of laser input to frequency-doubling crystals.

101818-14

Two LiIO_3 crystals were used. At the highest input level (1.3 J at 10 Hz) an external SHG efficiency of 30 percent was obtained with an antireflection-coated 25-mm crystal, and an external efficiency of 20.3 percent with an uncoated 15-mm crystal. These values correspond to internal efficiencies of 31.2 and 25.2 percent, respectively, which are far below the internal SHG efficiencies previously obtained¹⁶ with LiIO_3 using 100- μs Nd:YAG macropulses.

Three antireflection-coated KD*P crystals with lengths of 25, 40, and 50 mm were used in this study. At 1.3 J they had internal SHG efficiencies of 26.5, 18.3, and 15.5 percent, respectively. These values represent an improvement over results previously obtained with a 100- μs pulse, but are far below the SHG efficiencies achieved in these crystals when irradiated with 1- μs pulses.¹⁷

A 7.2-mm uncoated $\beta\text{-BaB}_2\text{O}_4$ crystal yielded an internal SHG efficiency of 24 percent. However, the efficiency had not saturated at the highest fundamental input level, which corresponded to $\sim 90 \text{ MW/cm}^2$.

LA*P is a relatively new nonlinear crystal which has been described as superior to KD*P and to $\beta\text{-BaB}_2\text{O}_4$ for frequency conversion.¹⁸ A 25-mm LA*P crystal (90 percent deuterated) was obtained and tested, with disappointing results. A maximum of 5 percent external SHG efficiency was achieved at $\sim 47 \text{ MW/cm}^2$, decreasing to 4 percent at 90 MW/cm^2 . The crystal was found to be subject to damage easily by cleavage and relatively slight mechanical pressure. Further studies with this sample will be undertaken to establish why its conversion efficiency falls so far below expectations.

A flux-grown 4.2-mm KTP crystal sustained surface damage after being subjected to ~ 50 pulses at 40 MW/cm^2 . Prior to the onset of damage, an internal SHG efficiency of 23 percent had been attained.

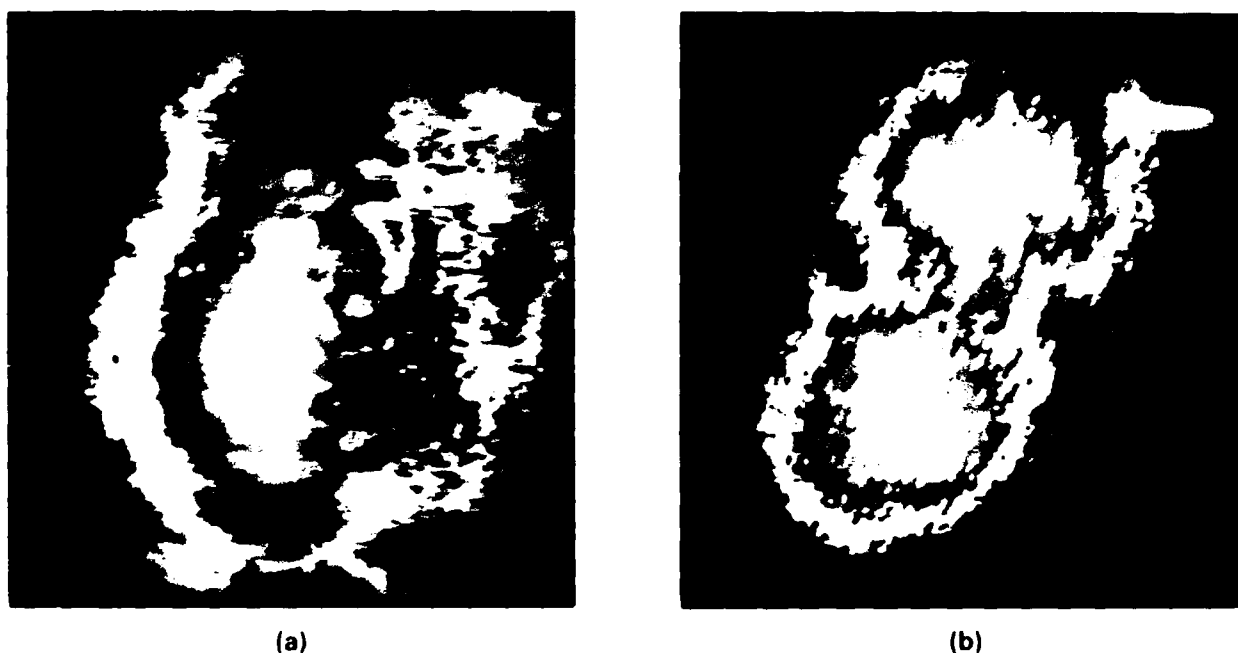


Figure 2-9. Spatial properties of (a) Nd:YAG laser system output at $1.064 \mu\text{m}$ and (b) the second harmonic generated in a LiIO_3 crystal at $0.532 \mu\text{m}$. The light areas in the centers are generally the regions of most intense radiation, but some of the hot spots within those regions appear as dark islands. The lighter regions on the perimeter represent areas of lower intensity than in the intervening dark region.

The frequency conversion efficiencies obtained in the various nonlinear materials, as described above, are uniformly disappointing. Even in the best case, namely, using a 25-mm LiIO_3 crystal, the second harmonic output pulse is limited to $\sim 400 \text{ mJ}$. The relatively low conversion efficiencies are believed to be due to the multimode nature of the Nd:YAG laser beam.

A number of experiments appear to support this hypothesis. First, a beam-focusing experiment indicated that the laser output is approximately five times diffraction limited. Next, a study of the beam after near-collimation, reduction to $\sim 1\text{-mm}$ diam. and passage through apertures varying from 0.4- to 1-mm diam. indicated the presence of hot spots within the beam. Finally, both the laser beam output and the frequency-doubled beam were studied directly and photographed, with the results shown in Figures 2-9(a) and (b), respectively. The fundamental beam shows considerable asymmetry and the presence of hot spots; however, the most notable feature when comparing the figures is the presence of two distinct maxima in the doubled beam in marked contrast to the fundamental. Although Figure 2-9(b) was obtained with a LiIO_3 crystal, similar results were obtained with $\beta\text{-BaB}_2\text{O}_4$ and KD^*P . Second harmonic output energy could be transferred from the upper to the lower peak or vice versa by rotating the crystal, but a single

maximum matching that of the fundamental could not be obtained. This indicates the presence of diverging phase fronts within the laser beam and illustrates the difficulty in achieving phase-matching of the entire laser output as the system is presently configured.

N. Menyuk
M.E. MacInnis

2.4 AMPLIFIED SPONTANEOUS EMISSION IN A Ti:Al₂O₃ AMPLIFIER

In recent experimental work,¹⁹ the time dependence of gain in a Ti:Al₂O₃ amplifier was measured. It was shown that the decay of gain was much more rapid than expected if only spontaneous decay was responsible for depletion of the upper state. Although it was conjectured that amplified spontaneous emission (ASE) might be responsible for this difference, the apparent difficulty²⁰⁻²⁶ of calculating ASE inhibited pursuit of this conjecture. The new rate equation given below shows unequivocally that the fast decay is a result of ASE.

The rate equation accounts for processes that directly affect the total population inversion in the amplifier. The population inversion density is equal to the gain per unit length, g , divided by the stimulated emission cross section σ . The total population inversion per unit area is proportional to $\gamma \equiv \int_0^L g dx$, where L is the length of the amplifier. The gain of the amplifier is e^γ , where the time dependence of γ satisfies the equation

$$\frac{d\gamma}{dt} = \left[-\gamma + \frac{I_{abs}}{I_{sat}^p} - \left(\frac{I_{in}}{I_{sat}} + \frac{\Omega}{4\pi} \right) (e^\gamma - 1) \right] \frac{1}{\tau} \quad (2-6)$$

The three terms in this equation describe the spontaneous emission rate, the pump rate, and the stimulated emission rate caused by the input to the amplifier and by ASE, respectively. Here, the ASE is modeled by an additional input intensity, $(\Omega/4\pi) I_{sat}$, assuming that the population inversion is spatially uniform.²⁷ I_{abs} is the pump intensity absorbed in the gain medium, Ω is the effective solid angle for ASE, τ is the lifetime of the excited state, I_{in} is the intensity input to the laser amplifier, I_{sat} is the saturation intensity, and I_{sat}^p is the saturation intensity for the pump.

Equation (2-6) is spatially integrated to describe the output of the amplifier. The inversion (proportional to γ) decays by spontaneous emission at a rate of $1/\tau$, is replenished by pumping, and is depleted by extraction of the energy either by a probe beam or by ASE. An assumption that has been made in obtaining Equation (2-6) is that the intensity comes to a steady state rapidly compared with the population inversion. The time scale for the intensity to reach steady state is determined by the time required to traverse the amplifier. As long as the net inversion does not change significantly on this time scale, Equation (2-6) can be derived from the usual set of spatially dependent Equations (2-1a,b,c). This assumption is no longer valid for high-power amplification of picosecond and femtosecond pulses.

Equation (2-6) also assumes a two-level model for the active medium. The lower state of the gain transition relaxes to the ground state, and the upper state of the pump transition relaxes to

the upper state of the gain transition in times that are short compared with the processes considered above. Such a model is applicable to many important laser transitions. The rate equation ignores the spatial distribution of the population inversion and ignores any change in optical intensity that is not related to a change in the population inversion, for instance, an absorption by the gain medium at the amplifying wavelength. These assumptions are valid for the Ti:Al₂O₃ amplifier experiment of Wall et al.¹⁹

In their experiment, a CW He-Ne laser or single-frequency Ti:Al₂O₃ laser²⁸ propagated almost collinearly with the pump laser (a frequency-doubled Nd:YAG laser). The amplified beam passed through a narrowband filter centered at the amplifying wavelength and was monitored by a photodiode. The photodiode signal was monitored as a function of time. The 10-ns pump pulse is short compared with the monitoring time of 4 μ s and the spontaneous emission lifetime of 3.15 μ s. The probe beam has an intensity that does not significantly deplete the upper state. Thus, I_{abs} and I_{in} in Equation (2-6) can be neglected after 10 ns. For this situation, the differential equation is separable (as long as Ω is not a function of time). Thus, the decay of γ depends only on its value and not on initial conditions. In the limit of no ASE, the analytic solution is an exponential, but in the general case, the equation must be solved numerically.

Figure 2-10 shows the measured amplified output as a function of time and the prediction of the rate equation for a case with $g_0L = \gamma(t=0) = 5.3$; the agreement is excellent. Without ASE, the signal would drop off half as fast. The 50-ns rise in the experimental data is caused by rise time of the detector and oscilloscope and the finite duration of the pump pulse, but is expected to have a minimal effect on the data after 50 ns.

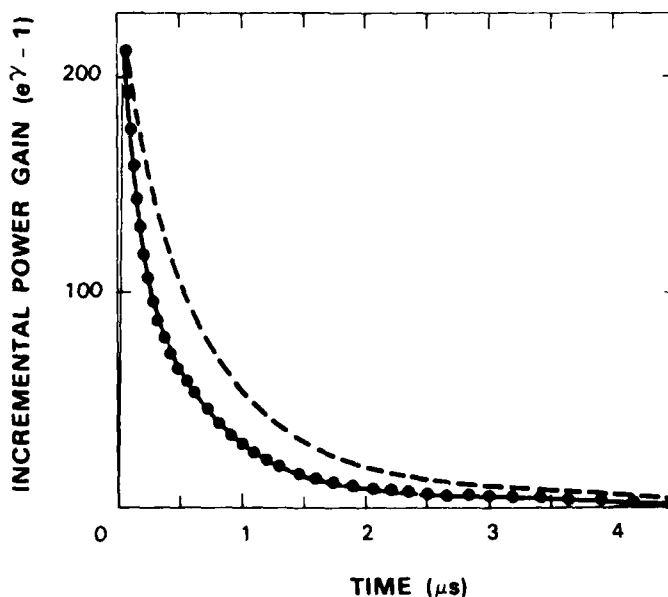


Figure 2-10. The decay (solid line) of the amplified signal at 791 nm in a Ti:Al₂O₃ crystal from Reference 10. The model (dots) gives an excellent fit to the decay with a solid angle parameter of 0.04. The experimentally measured initial value of γ is 5.27.

Similarly good fits of experimental data have been obtained for a series of different initial γ between 0.5 and 5. Each fit gives a different value for the solid angle parameter; these are plotted on a log-log scale in Figure 2-11. For the largest gains, the uncertainty is approximately the size of the boxes. For the low gains, the uncertainty is much larger because of the much lower experimental signals and the reduced contribution of ASE to gain depletion. For the lowest gain we estimate an uncertainty of approximately a factor of 2 in the solid angle parameter. In all the predictions, the fit to the experimental data is as good as that shown in Figure 2-10.

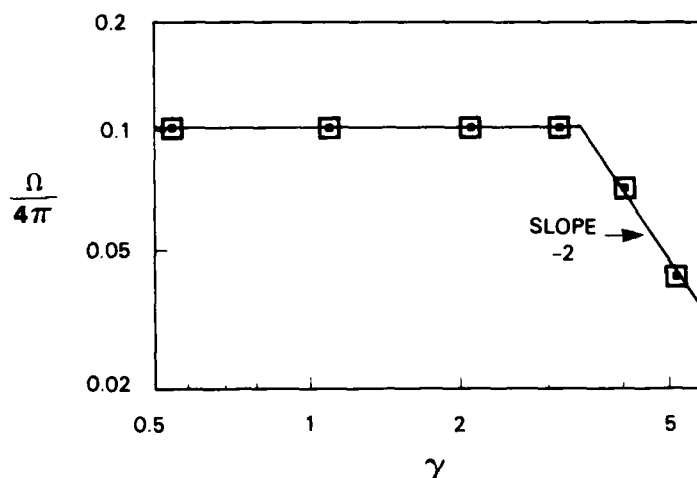


Figure 2-11. Log-log plot of solid angle parameters obtained from model versus amplifier gain. An intensity-independent solid angle is expected at low intensities. At high intensities such that the pump saturates the inversion, the solid angle is expected to decrease as γ^2 , shown as a line with slope -2 on this log-log plot.

We can estimate the solid angle parameter from the experimental geometry: the pump beam diameter is 3 mm, and the 1/e absorption length is 5 mm. This gives a ratio of the solid angle effective for ASE to the total solid angle, $\Omega/4\pi$, equal to 0.2 (see References 20 and 22). This estimate should be compared with the value of 0.1 that fits the experimental results. The factor of 2 discrepancy is not surprising in view of the approximations made in this model. At lower intensities, when the pump intensity is well below the saturation intensity, the solid angle parameter should be independent of the pump intensity, as observed.

However, for pump energies larger than the pump beam saturation energy density of 5 J/cm^2 (corresponding to $\gamma \geq 3$), the absorption length is expected to be somewhat longer than the 5 mm given above, which would result in a somewhat smaller solid angle. The variation in solid angle parameter at different gains shown in Figure 2-11 is ascribed to the saturation of the Ti^{3+} ions by the pump laser beam. If the pump beam saturates strongly, then the length of the pumped region is proportional to γ . The solid angle should then vary as γ^{-2} . This is displayed as a line with slope -2 on the log-log plot of Figure 2-11. Good agreement is obtained.

These results can also be used to predict gain measurements at other wavelengths. Figure 2-12 shows a comparison of the prediction (no adjustable parameters) with gain measurements at 633 nm; the agreement is very good. Also shown is the gain if there were no ASE. Although the difference between these two curves is small, the data fit significantly better to the rate equation including ASE. In doing these calculations, γ is evaluated for 800 nm, then multiplied by the ratio of the gain cross sections at 633 and 800 nm, which is 25, to obtain the signal intensity.

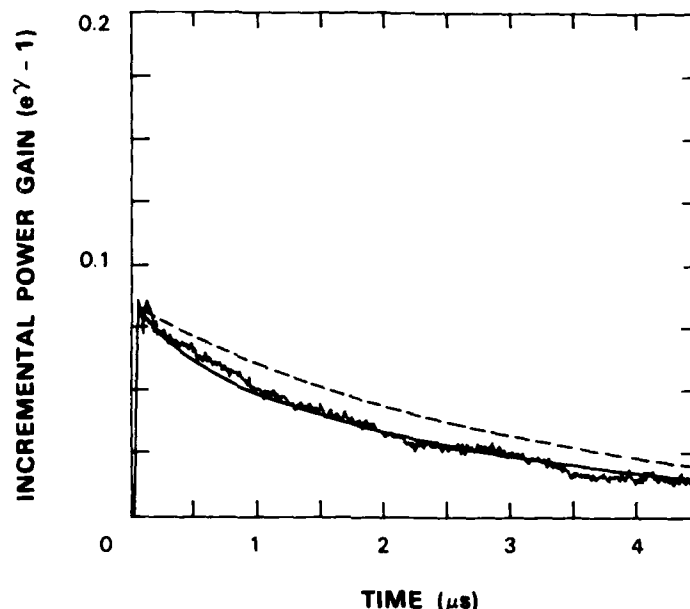


Figure 2-12. Decay of the amplified signal at 633 nm in a $\text{Ti:Al}_2\text{O}_3$ crystal from Reference 10. The model gives an excellent fit to the decay with no adjustable parameters. Also shown is the shape of the decay curve if amplified spontaneous emission is not included.

The rate equation approach is even simpler for a steady state calculation where the left side of Equation (2-6) is set to zero. Evaluating the extraction efficiency as a function of small signal gain gives good agreement with the detailed calculations¹⁹ for a small-aspect-ratio gain region. Thus, Equation (2-6) is expected to describe the approximate effects of ASE on the gain of laser amplifiers, including the possibility of time-dependent pumping and a time-dependent input. The limitation imposed by not considering the spatial variation of the inversion by ASE is probably not important for typical amplifier chains where ASE accounts for less than 50 percent of the output power.

The ease with which the effects of ASE can be calculated should promote better understanding of its role in amplifier chains. There is only one parameter required to do the calculations

and this can be estimated from the geometry. The simple model is applied successfully to an amplifier with a small aspect ratio ($L/D \sim 1.7$). Previous steady state treatments of this type^{21,23} have derivations which include the assumption of large aspect ratios (pencil-type geometry). The rate equation presented here suggests that previous work can be applied to small-aspect-ratio amplifiers. Further testing of the rate equation to understand its limitations is being done.

In conclusion, a simple rate equation including the effects of ASE gives very good agreement with time-dependent experiments. A better understanding of the effects of ASE on experimental results is obtained.

P.A. Schulz
R.L. Aggarwal
K.F. Wall

2.5 WAVELENGTH-INDEPENDENT FARADAY ISOLATOR

The dispersion of a Faraday material can be compensated by the dispersion of an optically active rotator to improve the wavelength independence by more than an order of magnitude. This concept was realized by Johnston and Proffitt²⁹ in building a unidirectional device for a ring laser; in that case only 2° rotation was required. By applying this concept to a 45° rotation, high isolation (>30 dB) over a broad wavelength region is achieved. The dispersion compensation is accomplished because both the Faraday rotation and the optical activity vary as the inverse square of the wavelength. Such a Faraday isolator has been built with better than 27-dB isolation from 700 to 900 nm.

The rotation of either a Faraday or an optically active rotator with 45° rotation at a reference wavelength λ_{ref} is given approximately by²⁹

$$\theta = \pm \frac{\pi}{4} \left(\frac{\lambda_{\text{ref}}}{\lambda} \right)^2 \quad (2-7)$$

By choosing the appropriate directions, the difference between the rotations in the Faraday and the optically active rotators is 0° in this approximation. For this case, perfect isolation is expected for a Faraday and a matched optically active rotator sandwiched between two orthogonal polarizers. In actual practice, because of nonuniformities in the magnetic field, imperfect polarizers, a slight mismatch in the reference wavelengths, and the approximation involved in Equation (2-7), isolation of >45 dB is difficult to achieve in a single isolator.³⁰ With appropriate choice of material, a single, fixed isolator can be used over a factor of 2 tuning range with >30 -dB isolation (0.1 percent backward transmission).

Another important parameter of a Faraday isolator is the forward transmission. Here, the approximate result is an important constraint. The transmission is given by

$$T = \sin^2 \left(\frac{\pi}{2} \frac{\lambda_{\text{ref}}^2}{\lambda^2} \right) \quad (2-8)$$

The usable wavelength range depends on how much intensity loss in the forward direction can be tolerated. For 50 percent forward transmission loss, the isolator can be used for wavelengths between 0.817 and $1.414 \lambda_{\text{ref}}$. For a reference wavelength of 780 nm , this constraint implies a wavelength range of 637 to 1100 nm , covering the entire near-infrared. Obviously, a different reference wavelength would shift the wavelength range. It should be noted that the approximation of Equation (2-7) is only accurate for wavelengths much longer than the absorption edge of the material. As the absorption edge is approached, a dispersion-free Faraday isolator could be built only if the Faraday and the optically active rotators are carefully matched, by having absorption edges close to each other. In an actual Faraday isolator, the forward transmission is also limited by the large number of surfaces and coatings and sometimes by absorption in the Faraday rotator material. In the following, the performance of such a Faraday isolator is described.

The Faraday isolator consists of an FR-5 glass Faraday rotator, an optically active quartz rotator, and two crystal polarizers. The Faraday and quartz rotators each have 45° rotation near 780 nm . They are not perfectly matched but were readily available in our laboratory. The two polarizers are aligned perpendicular to each other so there is no backward transmission. There is 90 percent forward transmission at 780 nm .

The backward isolation is limited by the problems described above and can be as good as the 45 dB achieved in a conventional isolator.³⁰ Figure 2-13 shows that our design has isolation $>27 \text{ dB}$ (backward transmission <0.2 percent) between 700 and 900 nm . Also shown in Figure 2-13 is the theoretical limit for an isolator with an 18-nm mismatch in the Faraday and the

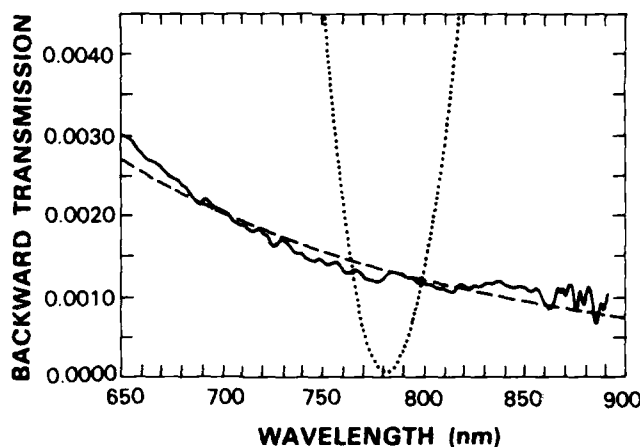


Figure 2-13. Backward transmission through Faraday isolator. The compensated Faraday isolator has a backward transmission (solid line) nearly independent of wavelength. The slight wavelength dependence is caused by a mismatch between the optically active rotator and the Faraday rotator of $\sim 1^\circ$ at 780 nm . Such a mismatch gives rise to an expected backward transmission (dashed line). The backward transmission of a conventional isolator is shown by the dotted line.

quartz rotators. An independent measurement of the wavelength mismatch gave a value of 20 ± 10 nm. The good agreement indicates that isolation significantly better than 30 dB should be achievable over the entire wavelength range.

Figure 2-14 shows the forward transmission through the Faraday isolator as a function of wavelength. The maximum forward transmission was ~ 93 percent as a result of reflection losses at the 12 optical surfaces (4 on each polarizer and 2 on each rotator). Also shown is the theoretical forward transmission which includes the wavelength dependence included in Equation (2-8). The actual transmission falls off faster than expected from the theory. Although we have not investigated this effect, it is likely caused by the coatings on the optical surfaces. The conventional isolator has somewhat better transmission, but as shown in Figure 2-13, it has very poor isolation away from its nominal wavelength.

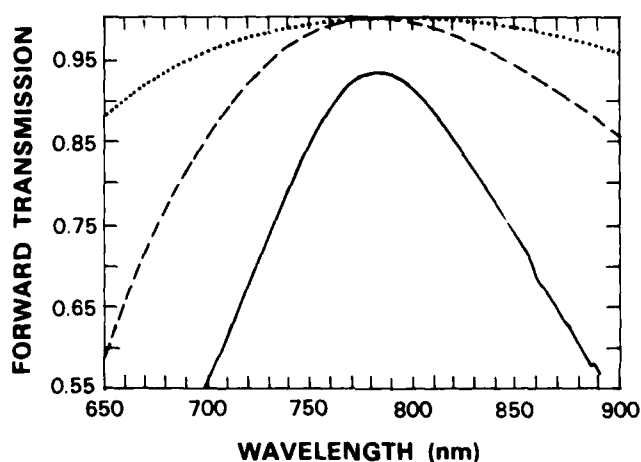


Figure 2-14. Forward transmission through Faraday isolator. The observed transmission (solid line) is smaller than expected (dashed line). The discrepancy may be caused by imperfect coatings. The expected transmission in a conventional isolator is shown by the dotted line.

In conclusion, a Faraday isolator that includes an optically active 45° rotator and a 45° Faraday rotator has been shown to give high isolation over a very wide wavelength range with no tuning. Such a device has been successfully demonstrated from 700 to 900 nm with over 55-percent transmission and over 27-dB isolation. Even better isolation with improved optics is expected.

P.A. Schulz
L.J. Belanger
S.K. McClung

REFERENCES

1. M. Michon, IEEE J. Quantum Electron. **QE-2**, 612 (1966).
2. S.E. Harris and R. Targ, Appl. Phys. Lett. **5**, 202 (1964).
3. S.E. Harris and O.P. McDuff, Appl. Phys. Lett. **5**, 205 (1964).
4. S.E. Harris and O.P. McDuff, IEEE J. Quantum Electron. **QE-1**, 245 (1965).
5. E.O. Ammann, B.J. McMurtry, and M.K. Oshman, IEEE J. Quantum Electron. **QE-1**, 263 (1965).
6. C.L. Tang and J.M. Telle, J. Appl. Phys. **45**, 4503 (1974).
7. G.C. Bjorklund, Opt. Lett. **5**, 15 (1980).
8. G.C. Bjorklund, M.D. Levenson, W. Length, and C. Ortiz, Appl. Phys. B **32**, 145 (1983).
9. S.R. Bramwell, D.M. Kane, and A.I. Ferguson, Int. Conf. on Quantum Electronics, San Francisco, CA, 1986, FCC6.
10. D.M. Kane, S.R. Bramwell, and A.I. Ferguson, in *Laser Spectroscopy VII*, T.W. Hansch and Y.R. Shen, eds., New York: Springer-Verlag (1986), p. 362.
11. Solid State Research Report, Lincoln Laboratory, MIT (1987:3), p. 25, DTIC AD-A192837.
12. D.J. Kuizenga and A.E. Siegman, IEEE J. Quantum Electron. **QE-6**, 673 (1970).
13. D.M. Kane, S.R. Bramwell, and A.I. Ferguson, Appl. Phys. B **39**, 171 (1986).
14. D.M. Kane, S.R. Bramwell, and A.I. Ferguson, Appl. Phys. B **40**, 147 (1986).
15. S.R. Bramwell, A.I. Ferguson, and D.M. Kane, Opt. Comm. **61**, 87 (1987).
16. Solid State Research Report, Lincoln Laboratory, MIT (1987:1), p. 28, DTIC AD-A185987.
17. Ibid (1988:1), p. 28.
18. D. Eimerl, S. Velsko, L. Davis, F. Wang, G. Loiacono, and G. Kennedy, *Proceedings of 1988 Conference on Lasers and Electro-Optics*, paper TUJ2.
19. K. Wall, R.L. Aggarwal, R.E. Fahey, and A.J. Strauss, IEEE J. Quantum Electron. **QE-24** (1988).
20. D.D. Lowenthal and J.M. Eggleston, IEEE J. Quantum Electron. **QE-22**, 1165 (1986).
21. G. Haag, M. Munz, and G. Marowsky, IEEE J. Quantum Electron. **QE-19**, 1149 (1983).

22. H. Maeda and A. Yariv, Phys. Lett. A **43**, 383 (1973).
23. L. Allen and G.I. Peters, Phys. Rev. A **8**, 2031 (1973).
24. U. Ganiel, A. Hurdy, G. Neumann, and D. Treves, IEEE J. Quantum Electron. **QE-11**, 881 (1975).
25. J.B. Moreno, G.A. Fisk, and J.M. Hoffman, J. Appl. Phys. **48**, 238 (1977).
26. J.B. Trenholme, NRL Memorandum Report **2480** (1972).
27. A.E. Siegman, *Lasers* (University Science Books, Mill Valley, Calif., 1986).
28. P.A. Schulz, IEEE J. Quantum Electron. **QE-24** (June 1988).
29. T.F. Johnston, Jr. and W. Proffitt, IEEE J. Quantum Electron. **QE-16**, 483 (1980).
30. D.J. Gauthier, P. Marum, and R.W. Boyd, Opt. Lett. **11**, 623 (1986).

3. MATERIALS RESEARCH

3.1 INFRARED ABSORPTION OF Ir AND IrSi THIN FILMS ON Si

Silicide Schottky-barrier detectors are among the most promising sensors for large-scale monolithic infrared imager arrays. State-of-the-art Schottky-barrier imager arrays employ PtSi detectors,^{1,2} which have a cutoff wavelength of $\sim 6 \mu\text{m}$. With the objective of obtaining longer cutoff wavelengths, we are working on the development of IrSi detectors. We recently reported³ the reproducible fabrication of such detectors with a cutoff wavelength of $\sim 10 \mu\text{m}$.

Silicide detectors incorporate a silicide-Si Schottky diode that is formed by depositing a noble metal film on a p-type Si substrate, then annealing to convert the metal to the corresponding silicide by reaction with the substrate. Photodetection is accomplished by the internal photoemission process, which includes formation of hole-electron pairs by infrared absorption in the silicide film, transport of excited holes to the silicide-Si interface, and finally, transfer of holes into the Si substrate by emission over the energy barrier at the silicide-Si interface. The photodetector quantum efficiency is a sensitive function of silicide film thickness, since a reduction in thickness increases the probability that carriers elastically scattered from the silicide surface will be emitted into the Si, but also decreases the optical absorption in the film. The optimal thickness depends on the optical characteristics of the silicide. In the case of PtSi, experimental values of these characteristics⁴⁻⁶ have been used in the design of high-performance detectors,¹ for which the optimal thickness is $\sim 20 \text{ \AA}$. In order to obtain such values for Ir and IrSi, which have not been reported previously, we have measured the infrared absorption of Ir and IrSi films on Si substrates as a function of film thickness. In addition, we have measured the absorption of Pt and PtSi films on Si substrates for comparison with the literature values.

Thin films of Ir ranging in thickness from 5 to 200 \AA , as measured with a quartz-crystal monitor, were deposited by e-beam evaporation of 99.9-percent-pure Ir on p-type Si wafers polished on both sides. To form IrSi, the samples were removed from the evaporator and annealed at 500°C for 30 min in a separate vacuum system. A similar procedure was employed to prepare PtSi/Si control samples. On the basis of earlier thickness comparisons made by transmission electron microscopy, it has been assumed that each silicide film is twice as thick as the metal film from which it was formed.

A Perkin-Elmer Model 983 spectrophotometer was used to measure the reflection R and transmission T of the film/substrate samples over the wavelength range from 2.5 to 25 μm for radiation illuminating the substrate at near-normal incidence, as shown schematically in Figure 3-1. The substrate absorption is negligible over this range except for lattice absorption bands near 9 and 17 μm . Outside these spectral bands, the absorption of the film, A_f , is equal to the absorption of the film/substrate sample, $A = 1 - R - T$. Outside the lattice bands, the measured values of R and T , and, therefore, the values of A_f , were essentially independent of wavelength. For each set of metal/Si and silicide/Si samples, the R and T data obtained at 4 μm as a function of film thickness were analyzed in detail in order to compare the results with those reported⁴ for PtSi films at this wavelength. The analysis, which uses the known optical constants of

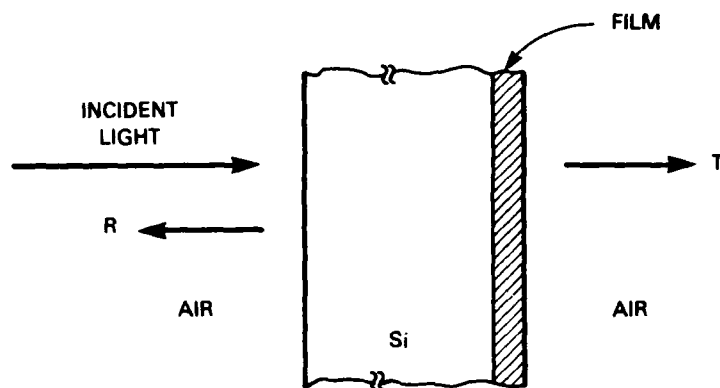


Figure 3-1. Configuration for measurement of reflection R and transmission T of film/substrate sample.

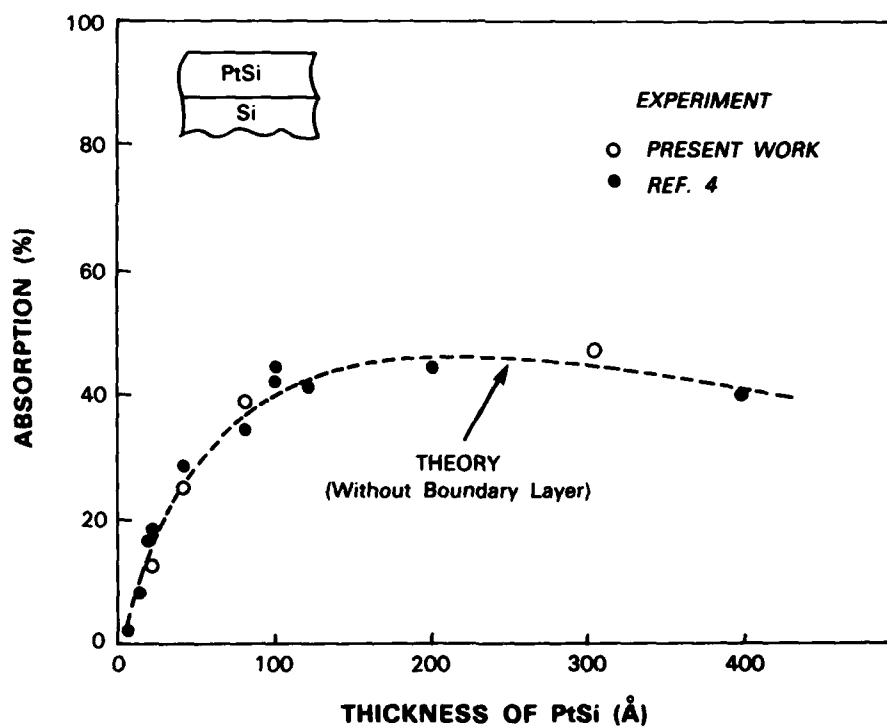


Figure 3-2. Absorption versus thickness for PtSi films on Si substrates.

Si to evaluate the reflection R_f and transmission T_f of the films, yields values of ϵ' and ϵ'' , the real and imaginary parts of the complex dielectric constant $\epsilon = \epsilon' + i\epsilon''$.

In Figure 3-2, the values of A_f at 4 μm obtained for the present PtSi films are plotted against film thickness. The results are in good agreement with those reported by Mooney.⁴ The theoretical curve shown in Figure 3-2 was calculated from the standard expression⁷ relating absorption to thickness by using the values $\epsilon' = -108$ and $\epsilon'' = 103$, which were found to give the best least-squares fit to the values of R_f , T_f , and A_f for all the PtSi/Si samples. The agreement between theory and experiment is excellent. Equally good agreement was obtained for the Pt films.

The situation is more complicated for the Ir and IrSi films. The values of A_f at 4 μm for these films are plotted against thickness in Figures 3-3(a) and (b), respectively. In neither case is satisfactory agreement between theory and experiment obtained by using a single pair of ϵ' and ϵ'' values. The best fits obtained by this procedure are represented by the dashed curves in Figure 3-3. For each set of films, the measured values of A_f initially fall well below the calculated curve. To account for the discrepancy, we propose that a boundary layer is present at the Ir-Si or IrSi-Si interface. To show that such a layer could account for the observations, we have calculated A_f versus thickness curves on the basis of a simple model, according to which films up to a certain thickness have the optical properties of the boundary layer, while thicker films consist of the fixed boundary layer and a variable overlayer of Ir or IrSi, as shown schematically in the insets of Figures 3-3(a) and (b). The values of ϵ' and ϵ'' for the boundary layer were found by fitting the data for thicknesses below 30 to 40 \AA , and these values were then adopted in obtaining ϵ' and ϵ'' values for the overlayer by fitting the data over the entire thickness range. The curves calculated by this procedure, which are shown as solid lines in Figure 3-3, are in very good agreement with the experimental results. The ϵ' and ϵ'' values for the boundary layers and overlayers, together with those for Pt and PtSi, are listed in Table 3-1.

The existence of the proposed boundary layers has been confirmed by Auger analysis. Figure 3-4 shows elemental depth profiles for both as-deposited and annealed Ir/Si and Pt/Si samples. Oxygen is detected at the Ir-Si and IrSi-Si interfaces, but not at the Pt-Si and PtSi-Si interfaces. Since Ir reacts very strongly with oxygen, it is not surprising that residual oxygen in the vacuum system is incorporated in the film at the beginning of Ir deposition. This gettered oxygen would remain at the Si interface during annealing, since Si is the dominant diffusion species during the formation of IrSi.

The thickness of the silicide films used in Schottky-barrier detectors is 50 \AA or less. Since the data of Figure 3-3 show that the presence of the boundary layer significantly reduces the infrared absorption of such thin films, elimination of this layer would improve detector quantum efficiency. We anticipate that such improvement can be achieved by carrying out the Ir deposition and annealing in an ultrahigh-vacuum system now being installed, which should have a substantially lower residual oxygen concentration than the systems used in the present experiments.

C. K. Chen
B-Y. Tsaur
M. C. Finn

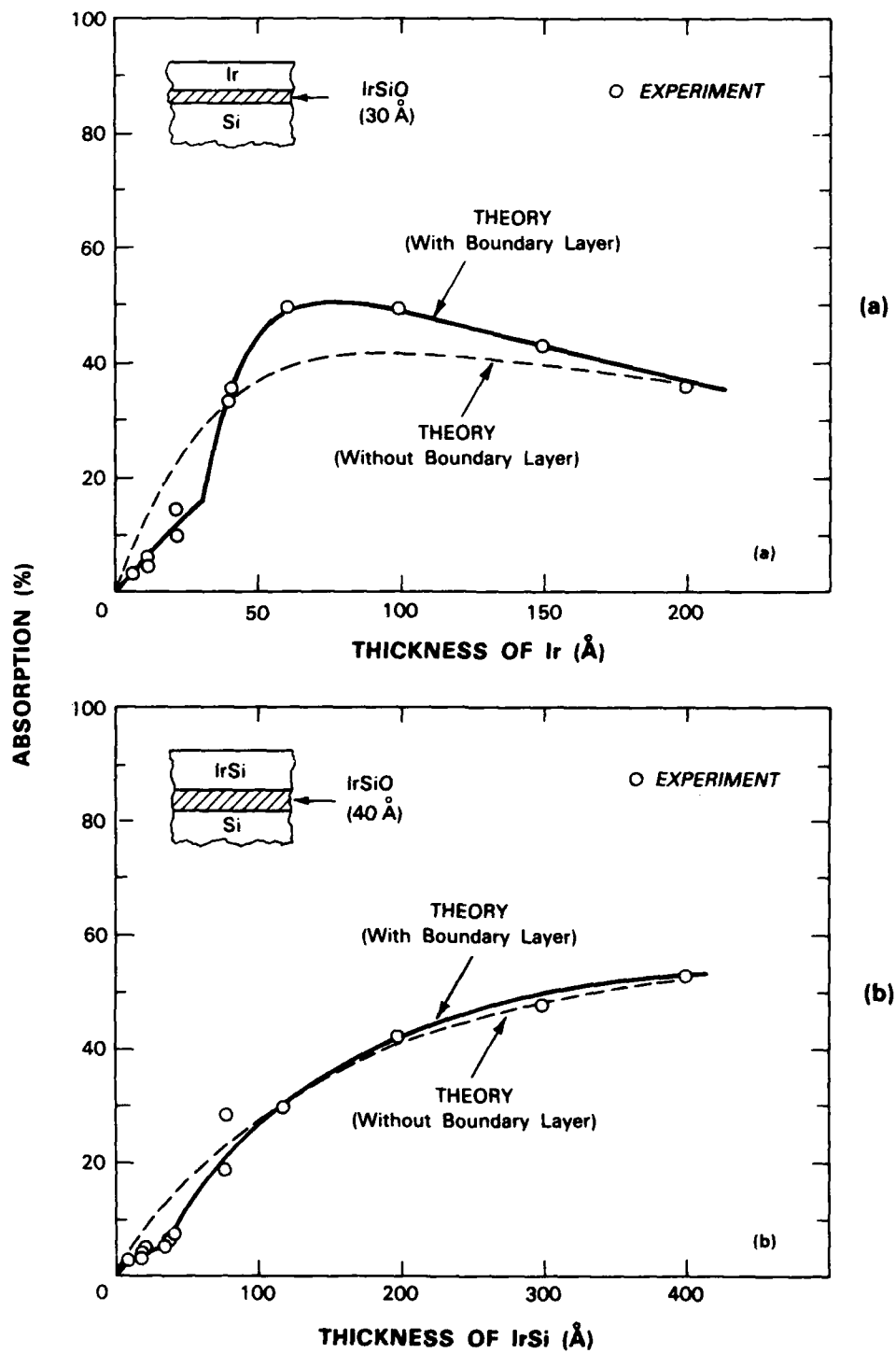


Figure 3-3. Absorption versus thickness for (a) Ir and (b) IrSi films on Si substrates.

TABLE 3-1		
Complex Dielectric Constants at 4 μm		
Material	ϵ'	ϵ''
Pt	-90	108
PtSi	-108	103
Ir		
Boundary Layer	-64	76
Overlayer	-340	490
IrSi		
Boundary Layer	0	16
Overlayer	-6	54

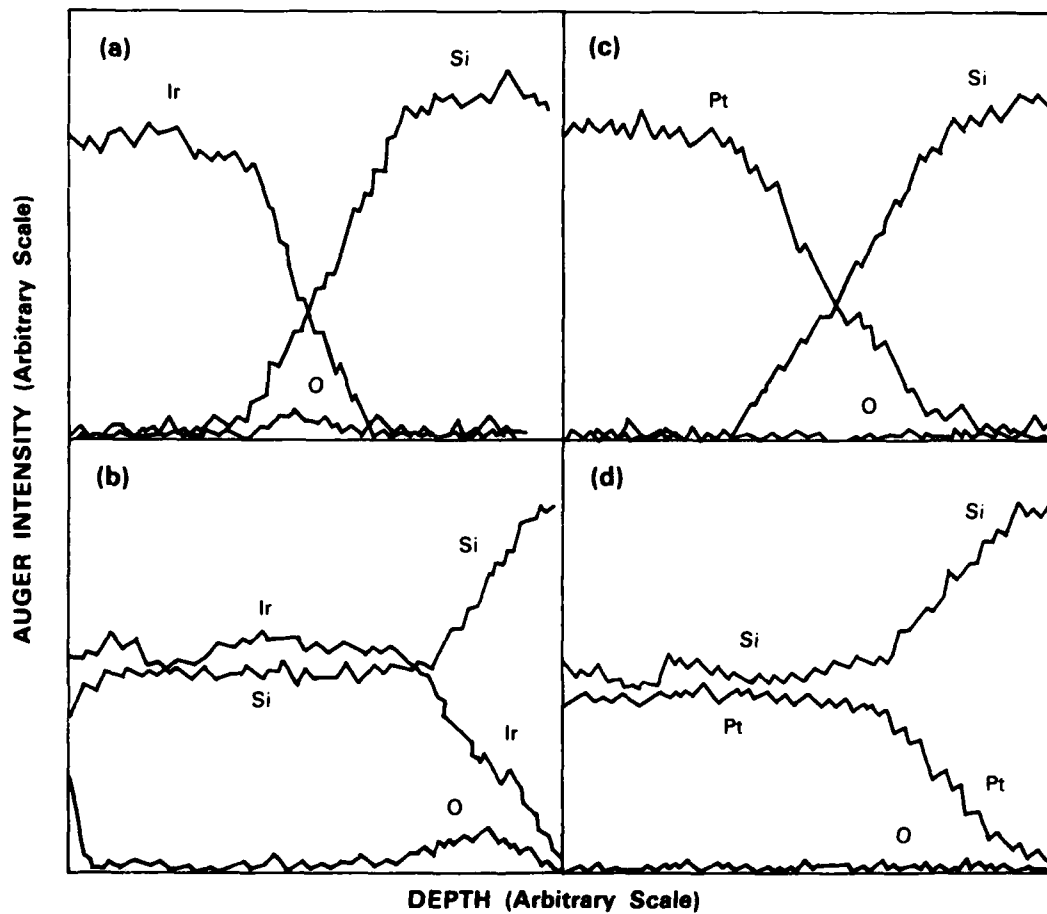


Figure 3-4. Elemental depth profiles obtained by Auger analysis for (a) Ir, (b) IrSi, (c) Pt, and (d) PtSi films on Si substrates.

3.2 100-MHz MODULATION OF GaAs/AlGaAs LED MONOLITHICALLY INTEGRATED WITH Si DRIVER CIRCUIT

Monolithic GaAs/Si (MGS) integration is potentially an advantageous technology for coupling Si VLSI circuits with GaAs/AlGaAs optoelectronic components and GaAs high-speed circuits. We have previously reported⁸ such integration of a GaAs/AlGaAs LED and a Si MOSFET, with LED modulation at rates up to 27 MHz accomplished by applying voltage pulses to the gate of the MOSFET. We now report the monolithic integration of a GaAs/AlGaAs LED with a Si driver circuit composed of 10 MOSFETs. Modulation rates of >100 MHz have been achieved.

The diagram for the LED/driver circuit is shown in Figure 3-5. Figure 3-6 is a photomicrograph of the completed circuit, which is based on a standard Si output buffer circuit with 2- μ m design rule. The MOSFET gate oxide thickness is 260 Å. The gate widths of the final driver transistors, Q_9 and Q_{10} , are 412 and 376 μ m, respectively. The LED replaces the buffer circuit output pad, so that the overall area remains the same. The LED anode is connected to the final driver stage by Cr/Au metallization, and the cathode is connected to ground through the heavily doped GaAs/Si heterointerface. The dimensions of the unmetallized opening for the LED output are 42×44 μ m.

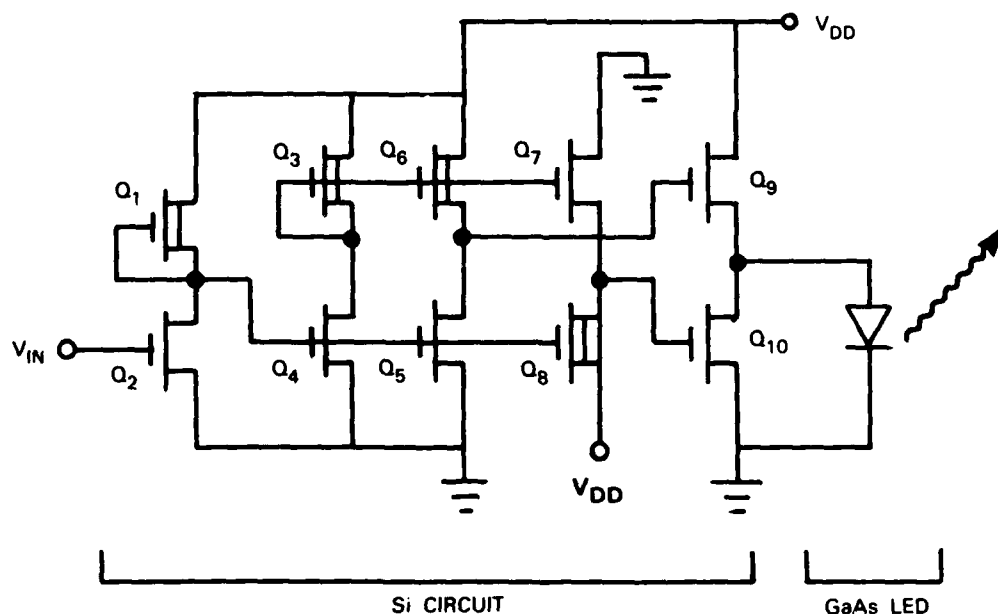


Figure 3-5. Circuit diagram of monolithically integrated LED/driver circuit.

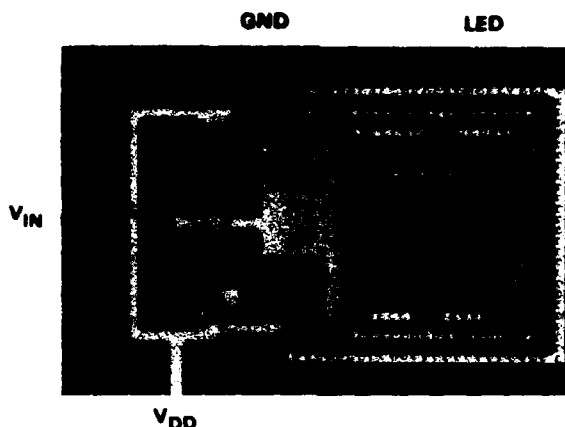


Figure 3-6. Photomicrograph of LED/driver circuit.

The sequence of processing steps was basically the same as the one used for LED/MOSFET fabrication.⁸ A p Si wafer slightly misoriented from (100) toward (111) was heavily implanted with arsenic to form n^+ islands where LEDs were to be fabricated. Around each island, Si MOSFETs were fabricated except for contact openings and metallization, using a poly-Si gate process. Successive layers of SiO_2 and Si_3N_4 were deposited over the entire wafer to protect the MOSFET structures during GaAs/AlGaAs epitaxy. Openings were etched in the $\text{Si}_3\text{N}_4/\text{SiO}_2$ film to expose the n^+ islands.

Molecular beam epitaxy was used to grow the following layers for the LED: 2- μm -thick n GaAs, 0.5- μm -thick n $\text{Al}_{0.3}\text{Ga}_{0.7}\text{As}$, 0.3- μm -thick nominally undoped GaAs, 0.5- μm -thick p $\text{Al}_{0.3}\text{Ga}_{0.7}\text{As}$, and 0.2- μm -thick p^+ GaAs. The growth procedure was similar to the one described previously,⁹ with growth temperatures of 580°C for GaAs and 710°C for AlGaAs. The material grown on the bare Si islands was single-crystal, while that deposited on the $\text{Si}_3\text{N}_4/\text{SiO}_2$ was polycrystalline.

The polycrystalline GaAs/AlGaAs material was removed by wet chemical etching, using a photoresist mask to protect the single-crystal layers. Plasma-enhanced chemical vapor deposition was used to deposit SiN_x over the entire wafer. Contact holes for the MOSFETs were etched in the nitride-oxide layer. Metallization was performed by evaporating and patterning Al to interconnect the Si devices. The LEDs were then fabricated in the single-crystal layers. Contact openings were etched for the LEDs, and Cr/Au was evaporated to form ohmic contacts to the anode and connect the anode to the driver transistors. Finally, Al was evaporated on the back of the Si wafer.

Very good operating characteristics were obtained for Si test devices and circuits fabricated on the same wafer as the LED/driver circuits. For enhancement- and depletion-mode MOSFETs, the respective transconductance values were about 100 and 120 mS/mm, the respective threshold

voltages were 0.85 and -3 V, the subthreshold slope was 0.1 V per decade of current, the subthreshold leakage current was $<10^{-13}$ A/ μ m gate length, and the breakdown voltage was about 7.5 V. The channel mobility estimated from transconductance measurements at low drain bias was about 540 cm²/V-s. For 19-stage ring oscillators, the gate delay was as low as 700 ps, and the power dissipation was 1.7 mW per gate. These results show that inclusion of the GaAs/AlGaAs epitaxial growth step in the present processing procedure does not lead to significant degradation of the Si devices and circuits.

For dc measurements of the LED light output, a microscope lens with numerical aperture of 0.65 was used to focus the light on a 1-cm-diam. p-i-n photodiode detector. Figure 3-7 shows the output power as a function of dc voltage applied to the input of the driver circuit. The LED is turned on when the voltage exceeds 2V. With the LED in the ON state, the current flow is about 9 mA, and the output power is about 0.3 μ W. To modulate the LED output, a stream of voltage pulses was applied to the input of the driver circuit with the drain bias at 5 V. For modulation measurements, the light was focused with the microscope lens on a 0.5-mm-diam. avalanche photodiode detector. Figure 3-8 shows the waveforms for the input voltage and light output when the voltage pulses were applied at a rate slightly higher than 100 MHz. Still higher modulation rates should be obtained by reducing the LED series resistance and the MOSFET gate length. The delay time of the light output with respect to the input voltage was measured by applying voltage pulses with a small duty cycle. The delay time, which results mainly from Si gate delays, is about 10 ns, in good agreement with the result of a circuit simulation.

In an initial LED lifetime measurement performed at room temperature for 144 h, the driver input and drain voltages were set at 5 V. The current through the LED was about 9 mA, corresponding to a current density of about 550 A/cm². The light output gradually decreased with time, probably because of the formation of dark-line and dark-spot defects. At the end of the run, the output was still above 70 percent of its initial value. This is a very encouraging result, in view of the fact that the GaAs/AlGaAs layers have a defect density of about 10⁷ cm⁻² and stress of more than 10⁹ dyne cm⁻². It is anticipated that improvement in the material quality will lead to greatly increased operating lifetime.

H.K. Choi
J.P. Mattia

G.W. Turner
B-Y. Tsaur

101121-4

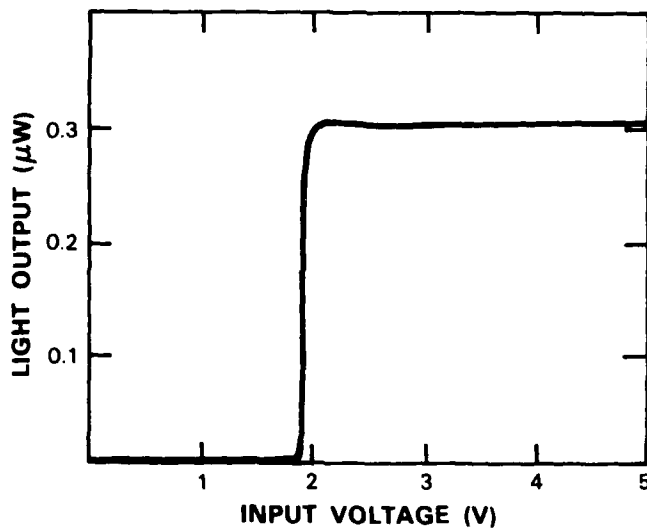


Figure 3-7. Dc light output of LED as a function of driver input voltage.

101818-21

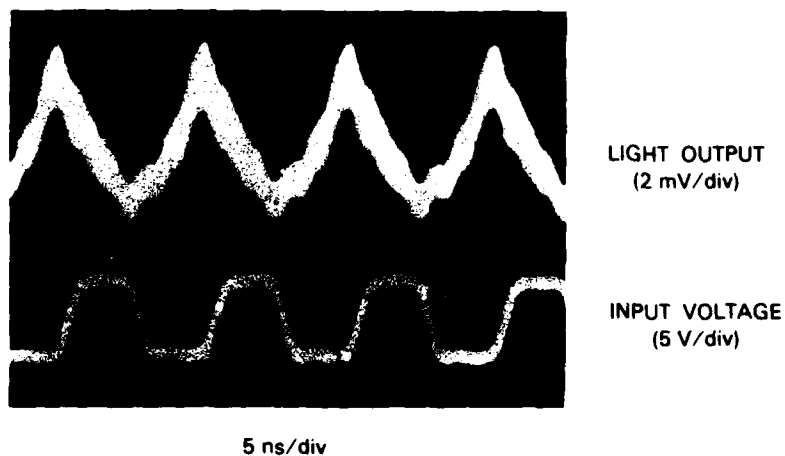


Figure 3-8. Waveforms of driver input voltage (5 V/div) and LED light output (5 mV/div) for modulation at 100 MHz.

REFERENCES

1. W.F. Kosonocky, F. V. Shallcross, T. S. Villani, and J. V. Groppe, IEEE Trans. Electron Devices **ED-22**, 1564 (1985).
2. M. Kimata, M. Denda, N. Yutani, S. Iwade, and N. Tsabouchi, IEEE ISSCC Digest of Technical Papers (1987), p. 110.
3. Solid State Research Report, Lincoln Laboratory, MIT (1988:1), p. 43.
4. J.M. Mooney, Ph.D. thesis, University of Arizona (1987), Chap. 4.
5. G.D. Mahan and D.T.F. Marple, Appl. Phys. Lett. **42**, 219 (1983).
6. J.M. Pimbley and W. Katz, Appl. Phys. Lett. **42**, 984 (1983).
7. A. Kahan, Appl. Opt. **3**, 314 (1964).
8. H.K. Choi, G.W. Turner, T.H. Windhorn, and B-Y. Tsaur, IEEE Electron Device Lett. **EDL-7**, 500 (1986).
9. H.K. Choi, G.W. Turner, and B-Y. Tsaur, IEEE Electron Device Lett. **EDL-7**, 241 (1986).

4. MICROELECTRONICS

4.1 DISCRETE FOURIER TRANSFORM CCD

A new CCD vector-matrix product device which is capable of performing a 16-point complex discrete Fourier transform (DFT) has been designed, and wafers have been fabricated. In this report, we describe the new input structure implemented on the DFT device. Test results indicate that the new structure yields more accurate CCD fixed-weight multipliers than those on the discrete cosine transform (DCT) device reported earlier.¹

A block diagram of a CCD DFT device is shown in Figure 4-1. The input vector x is represented by a complex time sequence. The output complex Fourier transform vector X is composed of the DCT and discrete sine transform (DST) of the input sequence. Each spectral output of the DFT chip is a summation of 32 products. Each product of this summation is computed by a CCD fixed-weight multiplier which is a single-channel CCD with two input gates as

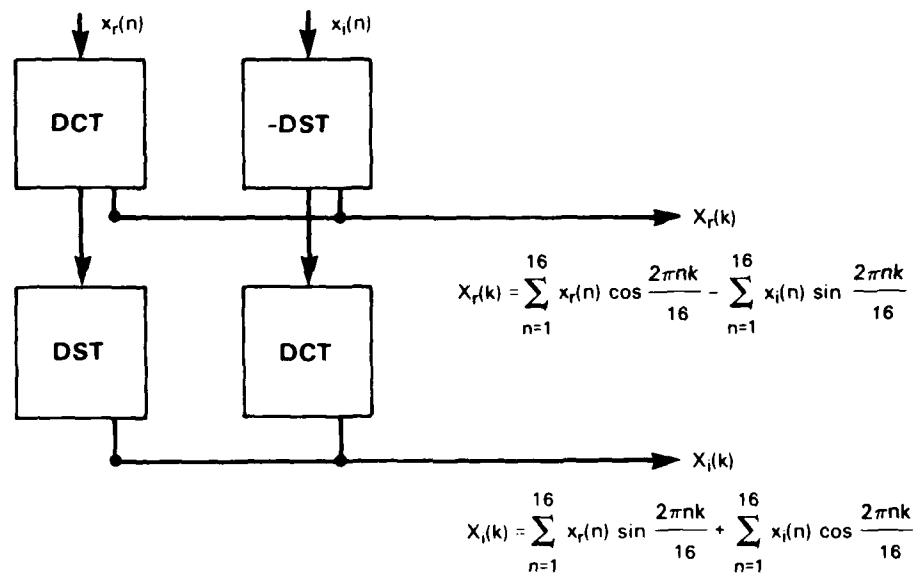


Figure 4-1. CCD discrete Fourier transform device concept.

shown in Figure 4-2. If a potential equilibration input method is used, the total amount of charge injected into this device can be expressed as²

$$Q_t = Q_s + Q_b \quad (4-1)$$

where $Q_s = C_0 (\pm A) (V_s - V_{\min}/2 - V_{\max}/2)$ is the four-quadrant signal charge and $Q_b = C_0 A (V_{\max}/2 - V_{\min}/2 + V_{th,g1} - V_{th,g2})$ is the bias charge. In the expression for Q_s , the + sign is used for a multiplier employing a normal input structure and corresponds to one with a positive weight, and the - sign is used for a device employing an inverting input and corresponds to a negative weight. In the normal input structure, the signal is applied to G_2 and V_{\min} is applied to G_1 ; in the inverting input structure, the signal is applied to G_1 and V_{\max} is applied to G_2 . In Equation (4-1), the input signal amplitude swing is limited to the range from V_{\min} to V_{\max} . Also C_0 is the oxide capacitance per unit area, A is the input gate area, and $V_{th,g1}$ and $V_{th,g2}$ are the threshold voltages of G_1 and G_2 , respectively.

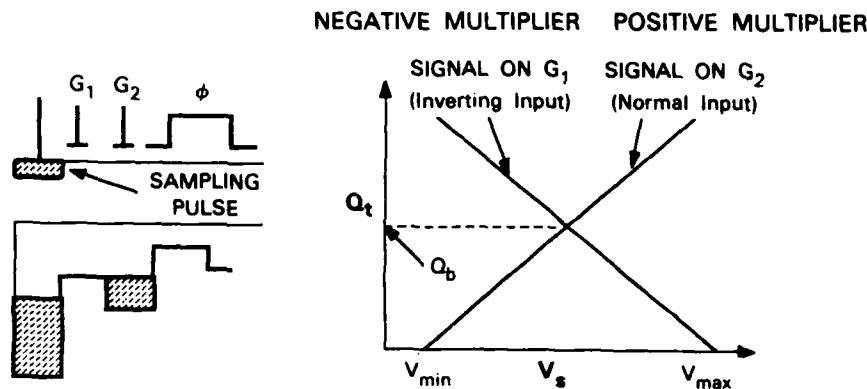
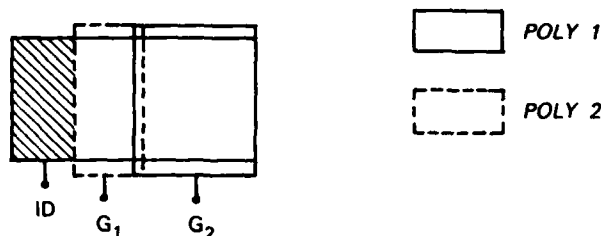


Figure 4-2. CCD fixed-weight multiplier with normal or inverting potential equilibration input structure.

In the conventional input structure shown in Figure 4-3, different levels of poly-Si are used for gates G_1 and G_2 . As can be seen in Equation (4-1), if there is any threshold nonuniformity between the poly-1 and -2 gates and if there is any process variation in defining the G_2 gate length, a computation error would be introduced by the fixed-weight multiplier. A new split-gate input structure (Figure 4-3) was used in designing the DFT chip to minimize the dependence of the device performance on the process control. The first and third gates of the split-gate structure are functionally equivalent to those of the conventional two-input-gate structure, while the second gate is biased at 15 V and serves as part of the storage well. In this new design, the input gate length is determined only by the pitch of the poly-1 gates, which is independent of etching variation. In addition, both the signal and reference voltages are applied to poly-1 gates; therefore, the device performance depends on the uniformity of one gate material only, rather than the uniformity of both poly-1 and -2 gates simultaneously.

● CONVENTIONAL STRUCTURE



● NEW SPLIT-GATE INPUT STRUCTURE

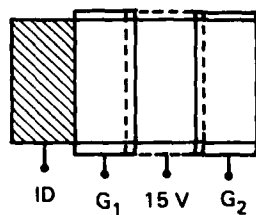


Figure 4-3. Conventional and new split-gate CCD input structures.

A photomicrograph of the DFT device is shown in Figure 4-4. The chip size is 7×9 mm. A double-poly-Si, double-metal CCD process with minimum feature size of $5 \mu\text{m}$ was used to fabricate the device. Table 4-1 presents a summary of the CCD fixed-weight multiplier performance, which shows that using split-gate input structure, multiplier weights within 1 percent of their design values have been achieved. The accuracy of the DFT device has been measured. For a given input vector, each element of the output vector computed by the device is digitized and compared with its expected output value. Test results indicate that the mean and standard deviation of computation errors of the DFT device are 11 and 6 mV, respectively. The maximum output of the device is ± 1500 mV. Therefore, the device has 8-bit accuracy. The above test results were obtained at 1-MHz clock rate. Preliminary test results indicate that at 10 MHz, the average computation error and standard deviation increase to 19.2 and 8.8 mV, respectively. At 10-MHz clock rate, harmonic distortion < -37 dB has been produced by the device. Currently, more high-speed tests are being carried out and results are being analyzed.

A.M. Chiang	G.A. Lincoln
P.C. Bennett	J.H. Reinold
B.B. Kosicki	K.F. Johnson
R.W. Mountain	

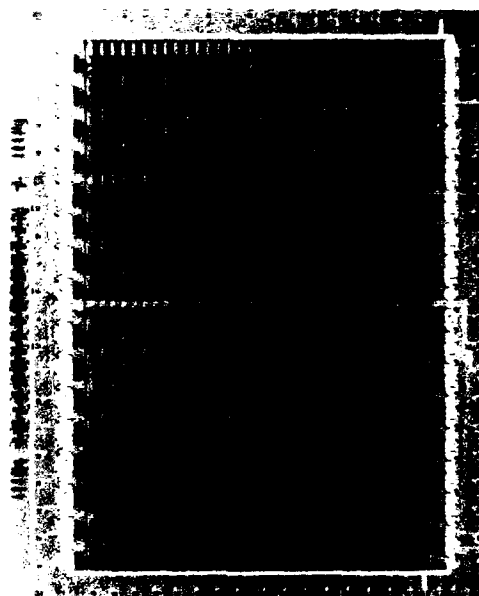


Figure 4-4. Photomicrograph of discrete Fourier transform CCD.

101818-25

TABLE 4-1				
Multiplier Accuracy				
Designed Weights	Measured Weights			
	Conventional Input		Split-Gate Input	
	Normalized Weight	Error (%)	Normalized Weight	Error (%)
1.0000	$1.0000 \pm .0057$	0.00	$1.0000 \pm .0066$	0.00
0.9250	$0.9260 \pm .0062$	0.1	$0.9150 \pm .0051$	1.0
0.7075	$0.7085 \pm .0047$	0.1	$0.7051 \pm .0068$	0.2
0.3835	$0.3833 \pm .0033$	0.02	$0.3801 \pm .0016$	0.3
-1.0000	$-1.0247 \pm .0044$	2.5	$1.0097 \pm .0067$	0.97
-0.9250	$-0.9486 \pm .0060$	2.4	$0.9243 \pm .0027$	0.07
-0.7075	$-0.7249 \pm .0038$	1.7	$0.7123 \pm .0051$	0.48
-0.3825	$-0.3947 \pm .0023$	1.02	$0.3849 \pm .0013$	0.2

4.2 BACK-ILLUMINATED THINNED CCD IMAGERS

A complete mounting/thinning/wire-bonding process has been developed to fabricate back-illuminated CCD imaging devices which have enhanced response in the blue and near-UV spectral region. A cross section of the finished device structure is shown in Figure 4-5.

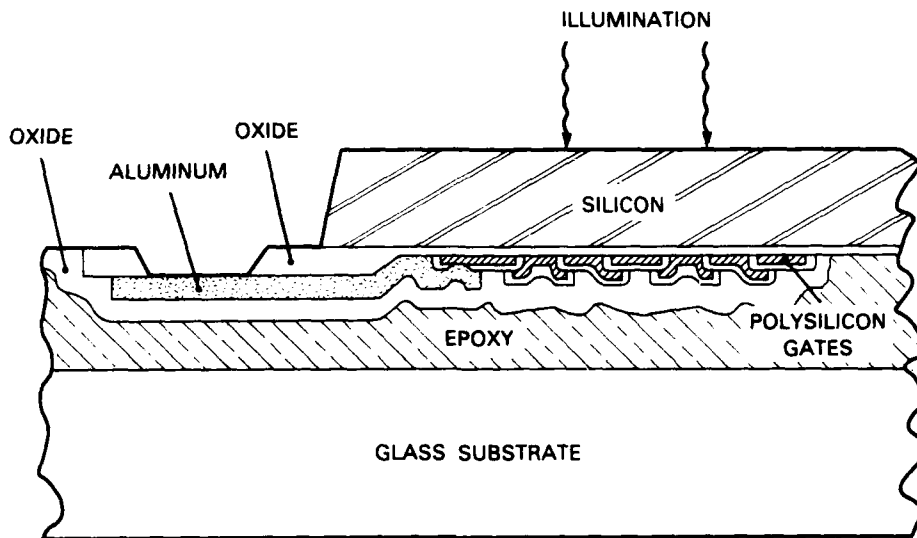


Figure 4-5. Cross-sectional view of thinned CCD device structure.

Key elements of the process for the back-illuminated imagers are shown in Table 4-2. Each step is compatible with conventional integrated circuit processes. The selection of the initial starting epitaxial material affects quality of the final surface finish. The worst back surface quality is observed on thinned devices fabricated on wafers of p^- epitaxial layers on p^+ substrates with resistivity $<0.01 \Omega\text{-cm}$. On these wafers, the slip lines due to the strain at the epitaxial-substrate interface are delineated after thinning. No slip lines are seen when using p^- epitaxial layers on either n^+ or p^+ substrates with resistivity $>0.01 \Omega\text{-cm}$. More point defects are developed on the back surface of thinned device wafers of p^- epitaxy on n^+ bulk than on p^- epitaxy on p^+ bulk. In addition to having fewer point defects, p^- epitaxy on p^+ wafers are also preferable to p^- on n^+ , because trace p^+ substrate material left on the thinned back surface is the correct type to enhance blue response. For these reasons, p^- on p^+ epitaxial wafers have been chosen for most future device processing.

After the CCD imagers are fabricated on the epitaxial wafer, an oxide layer is deposited over the front of the wafer to improve the adhesion between the wafer and the glass on which it will be mounted. The wafer is then mounted device-side toward the glass substrate using epoxy. We have improved the mounting process by changing from the original soft, low temperature (100°C) epoxy to a harder, higher temperature (300°C) epoxy. This mounting process is compatible with the photoresist and wire-bonding processes, and thinned wafers can endure the hot-sulfuric-acid cleaning process which is critical for proper back treatment.

TABLE 4-2**Fabrication Process for Backside-Illuminated Thinned Imagers**

1. Select proper p^-/p^+ epitaxial material.
2. Fabricate the CCD imager wafers.
3. Mount the front side of the imager to a glass substrate.
4. Mechanically remove most of the p^+ bulk.
5. Selectively etch the remaining p^+ bulk and expose the thin epitaxial layer.
6. Etch silicon and oxide to expose the pads.
7. Saw wafer into die, mount in package, and wire bond.

The wafer is then thinned by first lapping and polishing the majority of the p^+ substrate from the back. The remaining p^+ bulk is selectively etched away to the thin epitaxial layer. The number of defects seen on the etched surface is close to that of the original epitaxial wafer, with the addition of shallow etch-pits generated from point defects inside the p^+ bulk. The depth of these pits ranges from 500 to 5000 Å, depending on the vendor. So far, we have not observed any performance degradation related to these pits.

A plasma etching process is used on the back to remove all Si outside the active CCD array to expose the Al pads for wire-bonding. The photomask used to perform this step is aligned with respect to the front of the wafer using an infrared transmission mask aligner. A second photo step is then done to remove the SiO_2 on top of the Al pads. Figure 4-6 shows a whole wafer processed up to this step. Figure 4-7 shows Au-wire bonds to the Al pads supported by the epoxy underneath. The use of harder epoxy in the mounting process allows Al pads to be wire-bonded reliably by a wedge-wedge Al-wire bonder.

Several back-illuminated imagers have undergone initial electrical and optical evaluation. The noise and charge transfer efficiency of the devices appear to be equally as good as before thinning, as indicated by the results of an optical imaging test shown in Figure 4-8. A resolution chart has been imaged onto the device at light levels which produce 127 and 25 e/pixel [Figures 4-8(a) and (b), respectively], and the clarity of the patterns is indicative of good charge transfer efficiency at these low charge levels. The device noise is ~ 15 e rms at a 1-MHz data rate, which is the same as that of a typical front-illuminated device.

The most noticeable difference in the devices after thinning is that the dark current is highly nonuniform and up to 10 times higher than prior to thinning. This is because the bare etched surface is depleted and has a high surface generation rate. Variations in the dark current are the result of portions of the p^+ material remaining in some areas, while in others the etchant has reached the p^- epitaxial material. The residual p^+ suppresses the depletion and, therefore, the surface generation rate. Our future efforts will be directed at back-surface treatments which will

101818-33

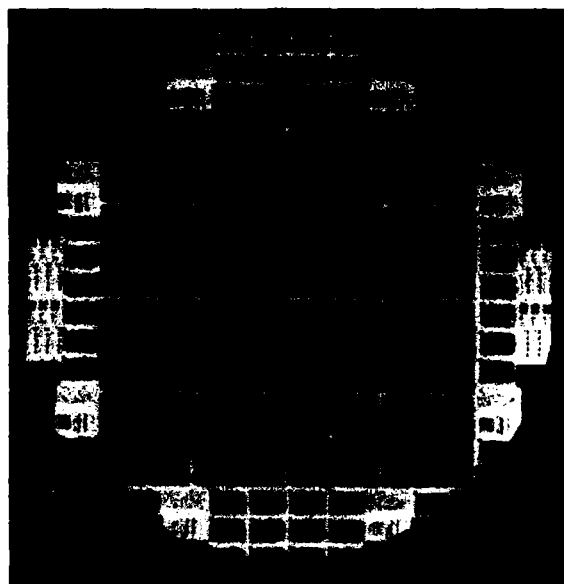


Figure 4-6. Whole 3-in wafer containing various types of imaging chips after mounting, thinning, and etching process.

101818-34

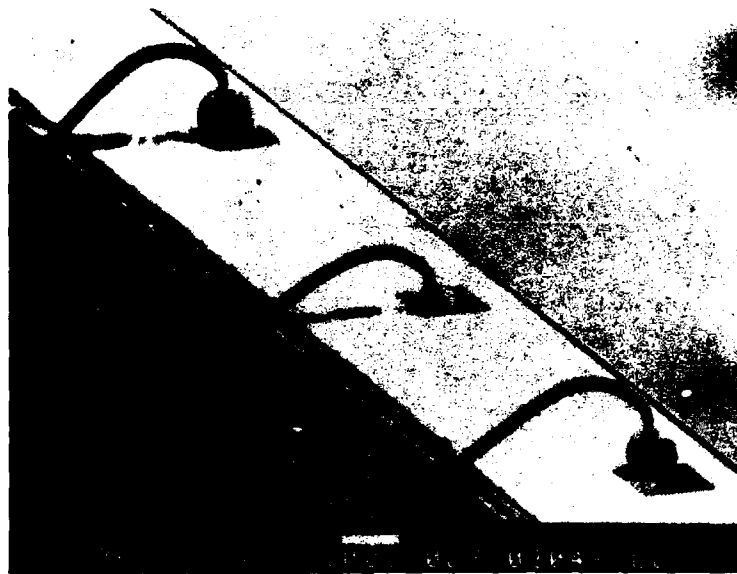


Figure 4-7. SEM photograph of wire bonds to thinned imaging chip.

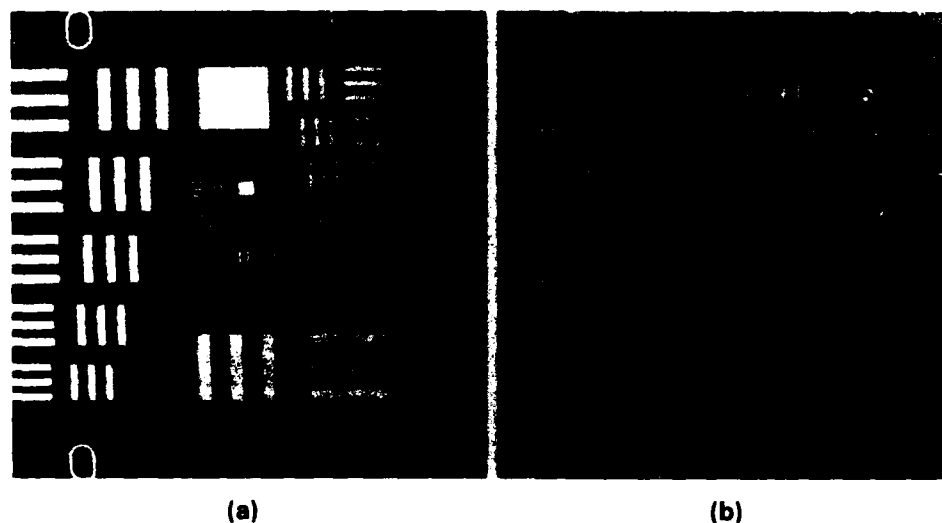


Figure 4-8. Resolution chart imaged onto thinned CCD at low light levels:
(a) 127 e/pixel, (b) 25 e/pixel.

maintain the surface in a state of accumulation in order to suppress the dark current and ensure high quantum efficiency. Section 4.3 presents results on the suitability of thin films of SiO_2 and Al_2O_3 for back-surface treatment.

J.C.M. Huang	M.A. Kaplan
B.E. Burke	B.B. Kosicki
P.J. Daniels	R.W. Mountain
A.R. Forte	N. Usiak
D.C. Harrison	

4.3 BACK STABILIZATION COATINGS FOR THINNED CCD IMAGERS

The response of thinned, back-illuminated CCD imagers could be improved in the visible and UV by introducing an electric field that drives photogenerated electrons deeper into the Si, towards the wells on the front of the device. One means of creating such an electric field would be to deposit on the back a transparent insulator that contains a negative charge. This negative charge would induce an accumulation of holes near the back, and the consequent band bending would drive electrons towards the front surface.

Aluminum oxide and Vycor films about 50 nm thick have been deposited on p- and n-type Si and overlaid with Al to fabricate MIS diodes. These devices were tested on an impedance bridge and the measured C-V curves analyzed. Table 4-3 reviews the results obtained with various deposited layers. Note that only e-beam-deposited Al_2O_3 yields net negative charge. A negative charge of $1.5 \times 10^{11} \text{ e/cm}^2$ would induce a field in the Si of about $1 \times 10^5 \text{ V/cm}$, which should be sufficient to increase the UV response of the CCD.

TABLE 4-3 Fixed Charge in Deposited Oxides		
Oxide	Deposition Method	Q_{ox} 10^{11} e/cm^2
SiO ₂	Thermal Oxidation	3.1
Vycor (7913)	E-beam (No O ₂)	12
Vycor (7910)	Sputter (No O ₂)	45
Al ₂ O ₃	Sputter (No O ₂)	32
Al ₂ O ₃	E-beam (No O ₂)	-5
Al ₂ O ₃	E-beam (4×10^{-5} Torr O ₂)	-1.1

It is interesting to note that the addition of O₂ to the e-beam system during deposition decreases the amount of negative charge. This is opposite to what might be expected from thermodynamic arguments, and suggests that the presence of oxygen alters the deposition kinetics of Al₂O₃ so that a more perfect oxide layer is deposited. This conclusion is supported by the higher breakdown voltage found for films deposited in the presence of O₂. In addition to breakdown at high fields, the diodes also exhibit marked hysteresis in bias stress tests. A positive bias on the Al electrode causes a negative shift in the fixed charge, while a negative bias causes a positive shift, leading eventually to a net positive fixed charge in the Al₂O₃. This hysteresis should not be a cause for concern in the devices while in operation, since the device will not be at elevated temperature or under an applied electric field. Also, this shift in net charge will, whether positive or negative, anneal out over a period of several days or weeks at room temperature, and the initial negative charge will return. Further, the first lot of samples, which has been unstressed, has retained negative charge for over five months.

The nature of the mobile charges in the Al₂O₃ films is not clear, as the defect species in bulk Al₂O₃ has not been definitively established. It is unlikely that alkali ions are the mobile species since deposited films of Al₂O₃ are used to block Na migration into SiO₂. The fixed charge induces a field in the oxide layer that is about $1 \times 10^5 \text{ V/cm}$ and this corresponds to a drop across the oxide of about 0.5 V. Such a voltage drop does not cause any motion of charge in bias stress tests and is below the breakdown voltage.

It appears, therefore, that deposition of Al₂O₃ will produce a stable accumulation of holes on the illuminated surface of a thinned imager and thereby improve the response of the back imager.

The first CCDs (both packaged and unpackaged devices) are now in the process of being coated with Al_2O_3 . The thickness chosen is 76 nm, so that the oxide layer will act as an antireflection coating and increase the photon flux at $\lambda = 500$ nm by about 50 percent.

J.A. Gregory
R.W. Mountain
R.V. Gray

REFERENCES

1. Solid State Research Report, Lincoln Laboratory, MIT (1987:3), p. 49, DTIC AD-A192837.
2. A.M. Chiang and B.E. Burke, IEEE J. Solid-State Circuits **SC-18**, 745 (1984).

5. ANALOG DEVICE TECHNOLOGY

5.1 PROCESS INTEGRATION OF SUPERCONDUCTING THIN FILMS AND DIELECTRIC THICK FILMS

Compact, superconductive analog signal processing devices with multigigahertz bandwidths have been constructed at Lincoln Laboratory. One of the most important elements in the architecture of these devices is delay lines. The low RF losses associated with superconductors allow electromagnetic delay lines, tens of meters long, to be built without appreciable loss, but their packing density is limited by crosstalk between adjacent lines. This crosstalk is minimized for striplines, where it falls exponentially with the distance between lines normalized to the distance b between ground planes (Figure 5-1). For crosstalk between 40 and 60 dB, the required separation is between 1.5 and 2 b . Hence, thinner dielectrics are desired because they allow a greater packing density and more delay per substrate.

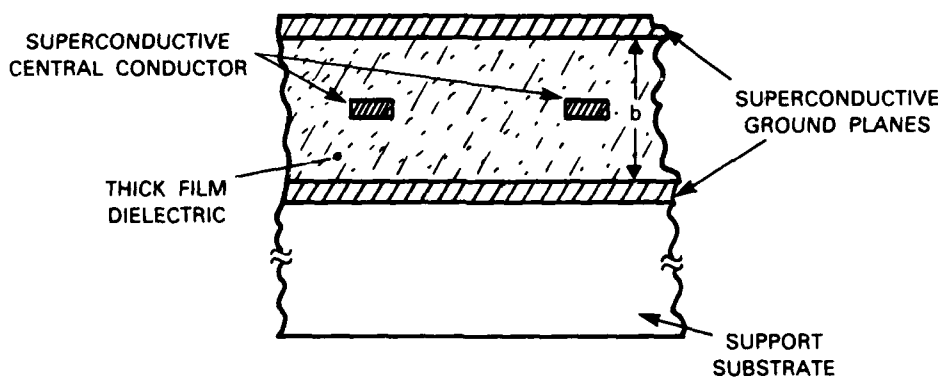


Figure 5-1. Basic structure for the stripline using an integrated superconductive-thin-film/dielectric-thick-film approach.

The minimum thickness of the dielectric is determined by allowable losses. To maintain the same characteristic impedance, the width of the line must be reduced in proportion to the thickness of the dielectric. Under these circumstances the attenuation of the lines is inversely proportional to the thickness. This imposes a lower limit on the thickness of the dielectric.

Most of our current devices use 125- μm -thick, 2-in.-diam. Si wafers for a maximum delay of 40 ns. This delay has been extended to 100 ns with the use of 50- μm -thick wafers, but this represents the limit of the present technology, since thinner or larger substrates are too fragile to handle and difficult to manufacture. A design that maximizes delay, however, would require thinner and larger substrates. For example, for high-quality Nb films, an optimum design leads to the following parameters: 14- μm -wide lines, distance between ground planes equal to 20 μm , and distance between lines equal to 32 μm . We assume a dielectric constant of 10. For this

optimized design, a total delay of 1 μ s can be accommodated in a 3-in substrate, with a maximum loss of 1 Np (8.69 dB) at 10 GHz and a maximum crosstalk of 50 dB between adjacent lines. For other design parameters, other dielectric thicknesses will be optimum, but, in general, for most applications a dielectric thickness between 10 and 25 μ m is desirable.

An alternative method to fabricate these lines is an integrated technology using thin-film superconductors and thick-film dielectrics. In this approach, shown schematically in Figure 5-1, a superconducting ground plane is first deposited on a support substrate, followed by a thick-film dielectric. A second superconductive thin film is then deposited on the dielectric layer and patterned, forming the center conductor of the delay line. This is followed by a second layer of the dielectric and the second ground plane.

There are many difficulties involved with developing a technology to fabricate this structure. The deposition method for the dielectric must provide uniform layers, low dielectric losses, and be compatible with the superconductive thin films. Thin-film methods for deposition of dielectrics are usually limited to the deposition of films up to 2 μ m thick and usually produce fairly lossy films. Low-loss dielectric bulk ceramics can be produced, but they usually require high firing temperatures ($>1300^{\circ}\text{C}$). Also, screen printing, the common method for formation of thick ceramic films, can only reliably produce films thicker than 50 μ m. These films are usually fired at temperatures higher than 850°C in oxidizing atmospheres, which would damage the underlying superconducting film. Recently, thick-film pastes that can be fired in N_2 and are capable of producing thick films with $\tan \delta \sim 10^{-3}$ at room temperature became available. These films contain low-melting-point glass mixed with a ceramic powder to lower the firing temperature of the ceramic.

We have utilized one of these thick-film pastes to study the feasibility of producing thin-film-superconductor/thick-film-dielectric integrated circuits. It was our hope that at lower operating temperatures the losses associated with these ceramic thick films would be lowered enough to warrant their use in practical analog signal processing devices.

The basic structure used as a test vehicle for the development of this technology is illustrated in Figure 5-2. An LC resonator is used to identify possible problems with the process and at the same time evaluate the dielectric loss at low temperatures.

The superconductor used in this structure is NbN because it is much less reactive than Nb. Thin films of NbN are deposited by reactive sputtering in an Ar-5% N_2 atmosphere on a 2-in-diam. oxidized Si wafer using an RF diode system. The NbN layer used to define the bottom electrode and the inductor is 5000 \AA thick.

The thin dielectric layer between the NbN and the ceramic layer shown in Figure 5-2 has two functions. As an interface layer, it enhances the adhesion of the ceramic layer to the superconductor. As a diffusion layer, it prevents the reaction of the ceramic with the NbN and the oxidation of the latter during the firing cycle for the ceramic. Candidate materials for this layer were selected based on their thermodynamic stability. Among the oxides more stable than Nb_2O_5 ,

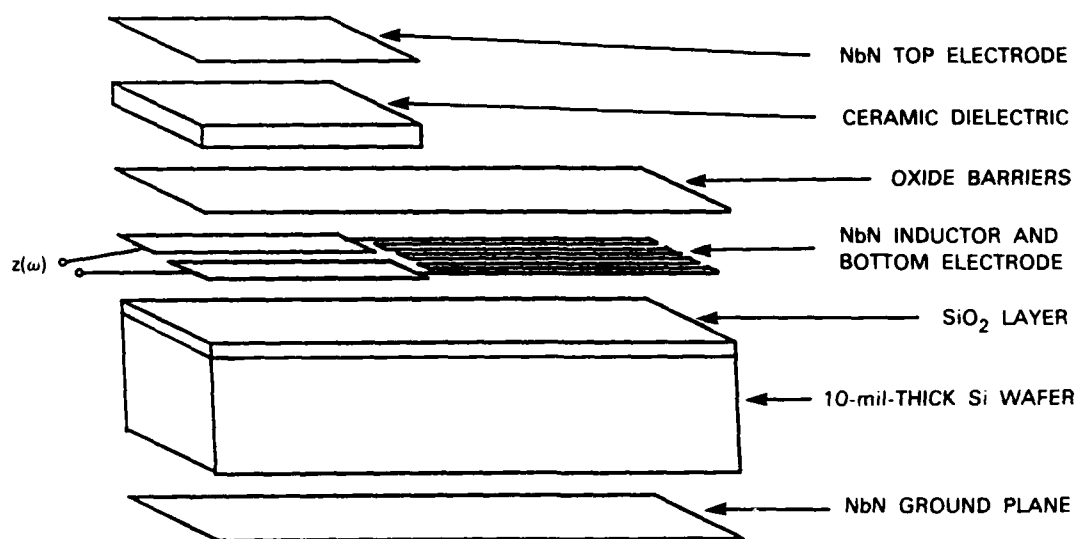


Figure 5-2. Exploded view of the L-C resonator test structure.

we chose SiO , MgO , and Al_2O_3 because of their known compatibility with NbN. A series of high-temperature (annealing) experiments were carried out to test the adequacy of these layers, leading us to choose a multilayer dielectric. First, a thin layer of SiO_2 (500\AA) is deposited on the NbN without exposing it to the air. The two films are then etched utilizing reactive ion etching (RIE). After patterning, a second layer of SiO_2 (7000\AA) and a layer of MgO (1000\AA) are deposited. This combination was found to minimize the degradation of the superconducting thin film.

The thick-film paste used for this structure is Electro Science Laboratory (ESL) 4906, which is N_2 -firable and is reported by the manufacturer to have a $\tan \delta$ of 10^{-3} at low frequency (1 kHz) and at room temperature. Numerous other pastes were also examined but were found to be incompatible with some step of the fabrication procedure. In order to form films of the desired thickness, a spin-on process was developed. The paste was diluted in thinner provided by ESL and spun on the patterned wafer. Films 10 to $20\text{ }\mu\text{m}$ thick could be easily produced using this method. A liftoff procedure was used to define the ceramic area. We used a thick-film photopolymer that was laminated onto the wafer using the same technology as for metal plating. The photoresist was then patterned using conventional photolithography. Dielectric paste was then spun onto the photoresist-patterned wafer and dried. The liftoff was accomplished by dissolution of the photoresist in a 5 percent solution of potassium hydroxide.

The firing of the thick-film paste was carried out in two stages. The burnout of the binder was carried out in air at 450°C for 1 h using a box muffle furnace. Previous tests had shown that the oxide-protected NbN did not deteriorate after this treatment.

We found that, even using extensive N_2 flushing of the furnace, N_2 firing at 850°C would destroy the superconductivity of the NbN films. Auger analysis showed that this was caused by

oxidation of the NbN by residual oxygen in the furnace. Consequently, a vacuum-firing process was implemented. For this vacuum-sintering process, the ceramic-coated wafers were placed in a quartz tube which was pumped to 10^{-7} Torr using an ion pump. The quartz tube was then placed in a furnace which was ramped up to 850°C in 3 h and was held at this temperature for 30 min. During the sintering, the outgassing of the film exceeded the pumping capacity of the ion pump and a sorption pump was used for the last part of the sintering sequence. The pressure at this stage was 10^{-3} Torr. The furnace was then allowed to cool to room temperature. A test made with this annealing procedure showed no significant suppression of T_c for the NbN films. (Typical T_c 's of 15 K were obtained on large-area samples, and a <2 -percent drop occurred upon annealing.) Finally, a thick film of NbN ($\sim 2\text{ }\mu\text{m}$) was deposited on the back of the Si wafer and on the top of the thick film. The counterelectrodes for the capacitors were patterned using RIE.

The device was packaged and contacts were made to the two lower capacitor electrodes of the resonator using ultrasonically bonded Al wires. The packaged device was tested using an impedance analyzer in a four-probe configuration. The device was mounted at the end of a probe and loaded into a liquid-He dewar. Four 1-m-long coaxial cables connected the package to the analyzer. The absolute value of the impedance and the phase angle were measured, from which the quality factor (Q) for the LC circuit was determined.

Two devices were tested. They have resonant frequencies of 6.1 and 5.6 MHz and Q s of 70 and 28, respectively. These values of Q are smaller than expected from the manufacturer data. It is not clear at this time if the higher-than-expected losses of the capacitors are due to the modified firing schedule or to undetected damage to the NbN. In new structures, measurements of the changes of the Q with temperature will help to clarify the loss mechanism.

S.C. Wong
A.C. Anderson

5.2 HIGH- T_c SUPERCONDUCTING RESONATORS

The recent discovery of the new metal-oxide high-transition-temperature superconducting materials¹ has stimulated interest in many applications, including high-quality-factor resonators which could be operated at liquid N_2 temperatures (77 K). Such resonators would be the basis for construction of low-phase-noise oscillators for application to radar and communication systems. The use of superconductors is of interest because extremely high Q s and high power levels are possible. Q s of 10^6 for thin-film stripline resonators operating at 1 GHz and 10^5 at 10 GHz are achievable with the standard materials such as Nb at liquid He temperatures. Even higher Q s have been achieved using superconducting cavities, but the stripline structure is preferred because it is compact, easy to fabricate, and can be integrated with other planar circuits.

The resonator Q is determined by the RF surface resistance of the superconducting material which, although low, is not identically zero as it is at dc. The finite RF resistance is a result of the nonzero mass of the superconducting electron pairs; an ac voltage results from this inertia which in turn drives the lossy normal electrons which are present at any nonzero temperature.

Few measurements of the RF surface resistance have been made in the new high- T_c materials, and as yet there is no reliable theoretical calculation. As discussed below, predictions of Q presently must rely upon measured data which depend strongly upon the material processing and thus should not be considered definitive.

However, if low-loss characteristics can be achieved reproducibly at gigahertz frequencies with the new materials, then devices of practical importance can be considered. Detailed calculations of oscillator phase noise will be presented, including such factors as amplifier flicker noise and power-handling capability of the superconductor. Calculations using a standard two-fluid model for the high- T_c materials based upon the measured bulk low-frequency properties show that a Q of 10^8 should be possible at 1 GHz at 50 K. However, the validity of the two-fluid model has not been confirmed, and measured values of resistance are more than an order of magnitude higher than those calculated from standard superconductivity theory.

Before calculating the phase noise of an oscillator stabilized with a superconducting resonator, we must first estimate the Q expected for the stripline structure and the maximum power that the resonator can support. In Figure 5-3 we show the cross section of the proposed stripline resonator. The two substrates are of an appropriate low-loss dielectric material, e.g., MgO, 1 mm thick. The center conductor is 2.54 mm wide. For this configuration, the conductor-limited quality factor, Q_c , obtainable with a material having a surface resistance R_s in ohms at a frequency f in hertz is

$$Q_c = 3.73 \times 10^{-9} \times f / R_s \quad , \quad (5-1)$$

and the maximum input power is

$$P = \frac{n\pi Z_o I_c^2}{8 I_L (1-I_L) Q_L} \quad (5-2)$$

where Z_o is the impedance of the stripline, I_c the maximum current for the center conductor, I_L the insertion loss, and Q_L the loaded Q . For the chosen dimensions, Z_o is 28 Ω .

We assume $R_s = 4.1 \times 10^{-4} \Omega$ at 10 GHz and 50 K, obtained by extrapolating the results from the Stanford/UCLA measurements,² done at 100 GHz, to lower frequencies assuming an f^2 dependence. For calculating I_c , we assume a critical current of 1×10^7 A/cm² at 50 K, a conservative assumption in view of the results of the Stanford group. For these values, and assuming an insertion loss of 15 dB, we obtain a Q of 150,000 at 5 GHz and a maximum input power of 32.4 W. The corresponding values for a center frequency of 10 GHz are $Q = 75,000$ and $P = 64$ W. These power levels are maximum input powers and not values of dissipated power.

In the calculation of Q and critical current, we used a stripline configuration for the transmission line. Stripline, besides eliminating radiation losses, can be dimensioned to maximize the Q and input power. Other structures, notably microstrip and coplanar lines, could also be used. Microstrip lines have the advantage that they require only a single substrate and hence are less sensitive to mechanical vibrations. The radiation losses can be minimized by careful design and

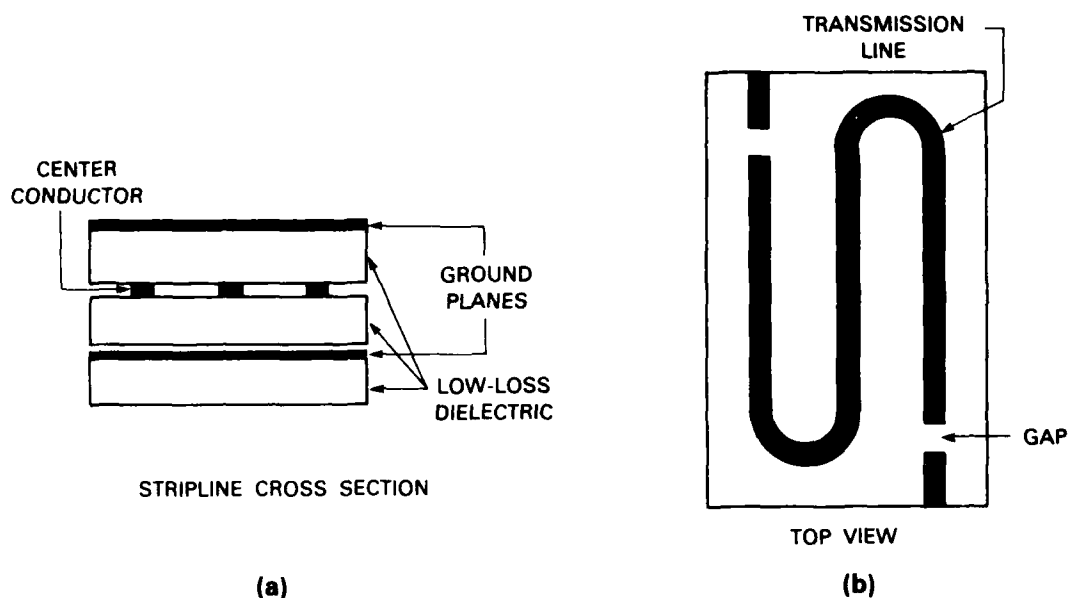


Figure 5-3. Stripline resonator structure: (a) cross section; (b) top view of center conductor.

packaging. Coplanar lines have the additional advantage that films have to be deposited on only one side of the substrate. For the same thin-film conductor properties, coplanar lines are lossier and can carry less current than a microstrip or stripline, but they may be adequate for our purposes.

Having calculated the Q and power, one can predict the values of phase noise to be expected from a feedback oscillator stabilized by a superconducting resonator, using the standard Leeson model.³ The stability of an oscillator to be used in a Doppler radar or communication system is best analyzed in the frequency domain where one considers the FM noise sidebands of the oscillator. This quantity is called the single-sideband phase noise and is given by the following expression:

$$L(\omega) = 10 \log \left[N^2 \left(1 + \frac{\omega_o^2}{4Q^2\omega^2} \right) \left(\frac{Gf k T}{P_c} + \frac{\alpha}{\omega} \right) \right] \quad (5-3)$$

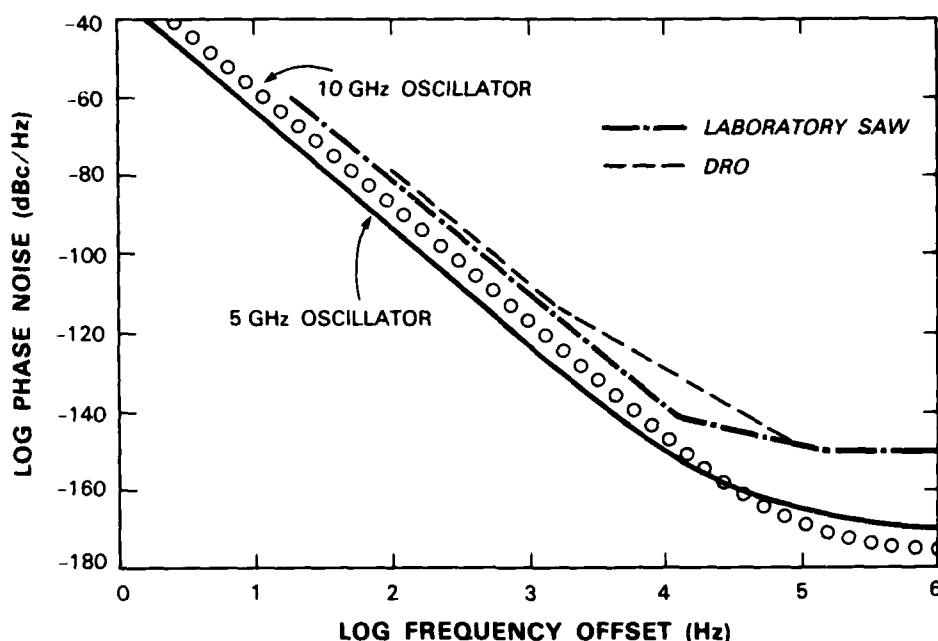
where $L(\omega)$ is the noise power relative to the carrier in a 1-Hz bandwidth (given in dBc/Hz), P_c is the power at the output of the amplifier, G is the loop gain, f is the amplifier noise figure, ω is the offset frequency in rad/s, Q is the loaded resonator quality factor, ω_o is the oscillator fundamental frequency, α is the empirically determined flicker-noise constant, k is Boltzmann's constant, T is the absolute temperature, and N is the frequency-multiplication factor. The flicker ($1/f$) noise can originate in either the amplifier, or the resonator, or both. Since the flicker noise is not well understood theoretically, it must be empirically determined. We can make reasonable estimates for the amplifier contribution, but for the resonator we must rely on experimentally determined values. This is a very important point. Our projections of phase noise that follow

assume that the contribution to the flicker noise from the resonator is small compared with the amplifier contribution, but the phase noise at offsets of less than about 5 kHz is dominated by the flicker noise. If the flicker noise contribution of the superconducting resonator is larger than that of the amplifier, then the actual phase noise will be greater than the following predictions. The importance of the resonator flicker noise has led us to undertake the measurements described below.

Figure 5-4 shows the projected phase noise at 10 GHz for a superconducting-resonator-stabilized oscillator for two different sets of parameters. One curve represents an oscillator operating at 5 GHz, frequency-doubled to obtain 10 GHz. The other parameters are $Q = 150,000$, $G = 15$ dB, $F = 6$ dB, $P = 25$ dBm (0.3 W), and $\alpha = 4 \times 10^{-12}$. This value of α is that normally assumed for a GaAs FET amplifier. The second curve represents an oscillator operating at 10 GHz with a $Q = 75,000$ and the other parameters unchanged from the first curve. The reduction in Q , when raising the frequency from 5 to 10 GHz, comes from the frequency dependence of the surface resistance of superconductors. The parameter values chosen for these curves are for illustrative purposes and should not be considered final. We have, for instance, assumed room-temperature operation for the amplifier, but when it is operated at the cryogenic temperatures, noise performance would be improved. We have also assumed an oscillator-loop power of 25 dBm because this value should be easily supported by a relatively simple and inexpensive amplifier. As discussed above, the power-handling capacity of the resonator itself is considerably higher than the 25 dBm used in the calculation. Still better phase-noise performance would be obtained with higher power levels, but this higher performance may not be necessary and may not justify the added expense of a higher-power amplifier. In addition, the insertion loss of the resonator is a design parameter which we are free to choose to optimize overall performance. For instance, it may be useful in the future to design the resonator so that a single transistor with a 10 dB gain provides the necessary loop gain for oscillation. This is entirely possible to do with a slight degradation of loaded Q . Such an option may be attractive if the unloaded Q can be made higher than our conservative projections.

Also shown in Figure 5-4 are the phase-noise curves for quartz crystal and SAW oscillators. Clearly, the superconducting oscillator provides better performance than any other technology and is able to meet the needs of real radar systems with a comfortable margin.

Because, as discussed above, the flicker noise of the superconducting resonator is unknown and because, even for the standard superconducting materials, there are no relevant experimental data, we have made preliminary measurements of the residual noise of an all-Nb superconducting resonator fabricated with the stripline structure described above. The devices have a loaded Q of $\sim 2.5 \times 10^4$, a fundamental resonant frequency of 1.15 GHz, and were operated at 4 K with the resonator in a liquid-He bath. The measurements were made by passing a constant frequency tone, generated by a synthesizer, through the resonator under test, and beating the output of the resonator against the tone. The power spectrum of this baseband output is the resonator contribution to the $1/f$ noise, the last term in parentheses of Equation (5-3).



101818-30

Figure 5-4. Calculated single-sideband phase noise.

The results are shown in Figure 5-5. The bandwidth of this resonator is 40 kHz, so one sees in the data the synthesizer phase noise for offset frequencies >40 kHz. For offset frequencies <1 kHz, the rise in the data is the result of the resonator. It is not clear how much of the noise is due to fundamental flicker noise in the resonator, how much is due to vibration in the resonator or liquid-He dewar probe, and how much is due to temperature fluctuations. The noise below 10-Hz offset no longer follows a $1/f$ frequency dependence, so that it is probably the result of either thermal or mechanical instabilities. (This resonator design, however, was made for material evaluation and not for oscillator application, so it is not surprising that performance is affected by vibration.)

Between 10 Hz and 1 kHz the curve closely follows a $1/f$ dependence. If the $1/f$ dependence between 10 Hz and 1 kHz is typical, the resonator flicker noise will be comparable to the GaAs amplifier contribution and will not severely degrade the performance predicted in Figure 5-4.

D.E. Oates
A.C. Anderson

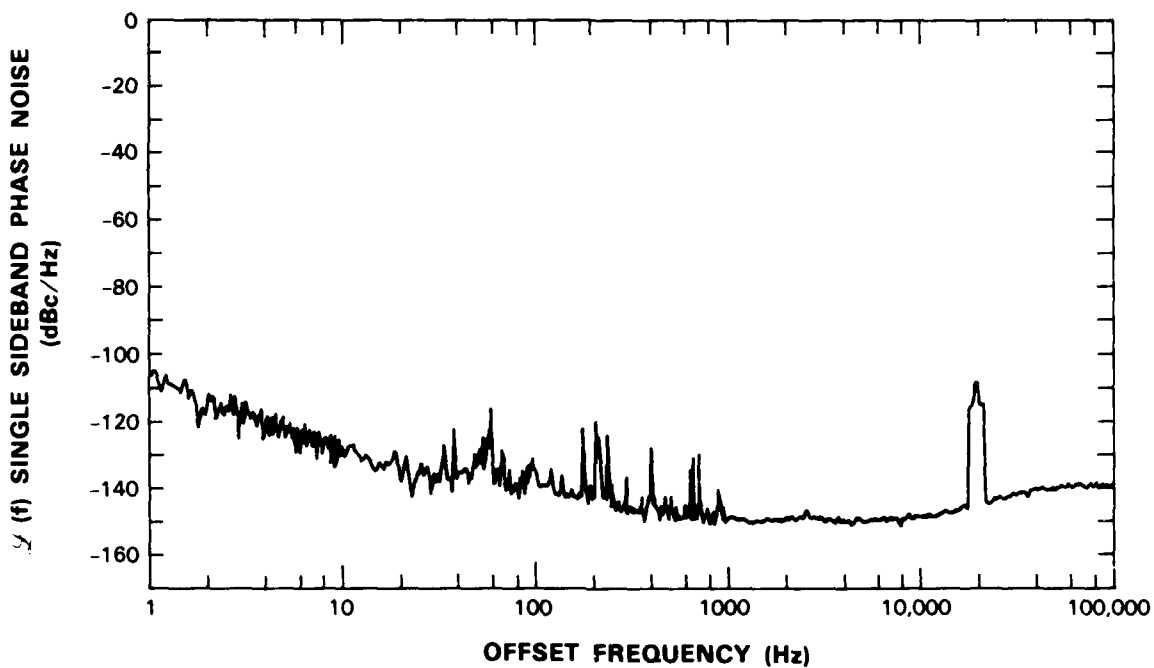


Figure 5-5. Measured residual noise for all-Nb superconducting resonator at 1.15 GHz.

REFERENCES

1. See for example, papers published in *High-Temperature Superconductors*, M.B. Brodsky, R.C. Dynes, K. Kitazawa, and H.L. Tuller, eds. (Materials Research Society, Pittsburgh, 1988).
2. M. Beasley, private communication.
3. T.E. Parker, "Precision Oscillators," in *Precision Frequency Control*, Vol 2, E.A. Gerber and A. Ballato, eds. (Academic Press, Orlando, Fla., 1985), pp. 66-79.

UNCLASSIFIED

SECURITY CLASSIFICATION OF THIS PAGE

REPORT DOCUMENTATION PAGE

1a. REPORT SECURITY CLASSIFICATION Unclassified			1b. RESTRICTIVE MARKINGS	
2a. SECURITY CLASSIFICATION AUTHORITY			3. DISTRIBUTION/AVAILABILITY OF REPORT Approved for public release; distribution unlimited.	
2b. DECLASSIFICATION/DOWNGRADING SCHEDULE				
4. PERFORMING ORGANIZATION REPORT NUMBER(S) 1988:2			5. MONITORING ORGANIZATION REPORT NUMBER(S) ESD-TR-88-162	
6a. NAME OF PERFORMING ORGANIZATION Lincoln Laboratory, MIT		6b. OFFICE SYMBOL (If applicable)		7a. NAME OF MONITORING ORGANIZATION Electronic Systems Division
6c. ADDRESS (City, State, and Zip Code) P.O. Box 73 Lexington, MA 02173-0073			7b. ADDRESS (City, State, and Zip Code) Hanscom AFB, MA 01731	
8a. NAME OF FUNDING/SPONSORING ORGANIZATION Air Force Systems Command, USAF		8b. OFFICE SYMBOL (If applicable)		9. PROCUREMENT INSTRUMENT IDENTIFICATION NUMBER F19628-85-C-0002
8c. ADDRESS (City, State, and Zip Code) Andrews AFB Washington, DC 20334			10. SOURCE OF FUNDING NUMBERS	
			PROGRAM ELEMENT NO. 63250F	TASK NO. 221
			PROJECT NO. 221	WORK UNIT ACCESSION NO.
11. TITLE (Include Security Classification) Solid State Research				
12. PERSONAL AUTHOR(S) Alan L. McWhorter				
13a. TYPE OF REPORT Quarterly Technical Report		13b. TIME COVERED FROM 2/1/88 TO 4/30/88		14. DATE OF REPORT (Year, Month, Day) 1988 May 15
15. PAGE COUNT 94				
16. SUPPLEMENTARY NOTATION None				
17. COSATI CODES			18. SUBJECT TERMS (Continue on reverse if necessary and identify by block number)	
FIELD	GROUP	SUB-GROUP	solid state devices, lasers, nonlinear optics	
			quantum electronics, laser arrays, integrated optics	
			materials research, optical modulation, microwave semiconductor devices	
			microelectronics, optical isolator, charge-coupled devices	
			analog device technology, infrared detectors, superconductors	
19. ABSTRACT (Continue on reverse if necessary and identify by block number)				
<p>This report covers in detail the research work of the Solid State Division at Lincoln Laboratory for the period 1 February through 30 April 1988. The topics covered are Solid State Device Research, Quantum Electronics, Materials Research, Microelectronics, and Analog Device Technology. Funding is provided primarily by the Air Force, with additional support provided by the Army, DARPA, Navy, SDIO, NASA, and DOE.</p>				
20. DISTRIBUTION/AVAILABILITY OF ABSTRACT <input type="checkbox"/> UNCLASSIFIED/UNLIMITED <input checked="" type="checkbox"/> SAME AS RPT. <input type="checkbox"/> DTIC USERS			21. ABSTRACT SECURITY CLASSIFICATION Unclassified	
22a. NAME OF RESPONSIBLE INDIVIDUAL Lt. Col. Hugh L. Southall, USAF			22b. TELEPHONE (Include Area Code) (617) 981-2330	22c. OFFICE SYMBOL ESD/TML